Escola de Camins
Escola Tècnica Superior d'Enginyeria de Camins, Canals i Ports
UPC BARCELONATECH

A coupled damage-elastoplasticity approach for cemented soils

MASTER FINAL THESIS

Thesis developed by:
Matias Alonso

Directed by:
Jean Vaunat

Master in:
Geotechnical Engineering

Barcelona, June 2019

Department of Civil and Environmental Engineering

Department of Civil and Environmental Engineering
Section of Geotechnical Engineering and Geosciences
Technical University of Catalonia
UPC BarcelonaTech

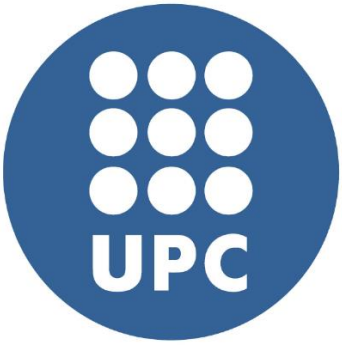

A coupled damage-elastoplasticity approach for cemented soils

Matias Alonso

Supervisor: Jean Vaunat

Barcelona, June 2019

Abstract

Structured materials, as cemented sands, have typically been treated as special cases. Due to bonded structure, their complex behaviour cannot be described by the basic concepts of soil mechanics.

Interest of cemented sands increased since the early 1970s, and many researchers have been giving important experimental contributions to the comprehension of this type of materials. An understanding of the way in which bonded structure influence the behaviour of cemented sands is required to formulate constitutive models intended to simulate their response.

In this work, the development and validation of a constitutive model intended to simulate the behaviour of cemented sands is addressed. The model is based on a composite material representing the two main elements present in this type of materials: particles of sands and cement. It includes concepts of classical elastoplasticity and damage theory. Therefore it is considered as a coupled damage-elastoplastic model.

The model is implemented in the Finite Element code Code_Bright using a Stress Point Algorithm based on an implicit integration scheme. Model performance is presented through simulated test, and a validation process through comparison with reported laboratory tests is carried out.

For isotropic compression tests, the agreement achieved is good, while for triaxial tests, the agreement achieved is poorer, particularly for the volumetric response. Finally, a relationship between the effectiveness of microstructure and the curing void ratio was found.

Resumen

Los suelos estructurados, como las arenas cementadas, se han tratado generalmente como casos especiales. Debido a su estructura adherida, su comportamiento no puede ser descrito a partir de los conceptos básicos de la mecánica de suelos.

El interés por las arenas cementadas ha venido aumentando desde principios de la década de 1970, y muchos investigadores han aportado importantes contribuciones experimentales para describir este tipo de materiales. Comprender de qué manera influye la cementación es necesario para formular modelos constitutivos destinados a simular su respuesta.

En este trabajo se aborda el desarrollo y validación de un modelo constitutivo para simular el comportamiento de arenas cementadas. El modelo se basa en un material compuesto que representa los dos elementos presentes en este tipo de materiales: partículas de arena y cemento. Incluye conceptos de elastoplasticidad clásica y teoría del daño, por lo que se considera un modelo acoplado de daño-elastoplasticidad.

El modelo se implementa en el código de elementos finitos *Code_Bright* usando un algoritmo basado en un esquema de integración implícito (*Stress Point Algorithm*). Las propiedades del modelo se muestran a través de ensayos simulados. Un proceso de validación es llevado a cabo mediante comparación con ensayos de laboratorio publicados.

La predicción del modelo en ensayos de compresión isotrópica es buena, mientras que en el caso de ensayos triaxiales, son menos acertadas. Finalmente, se ha encontrado una relación entre la efectividad de la microestructura y el índice de vacíos correspondiente al momento de curado del agente cementicio.

Contents

List of Tables

List of Figures

Chapter 1

Introduction

1.1.- Motivation, objectives and document structure

From a mechanical point of view, bonded soils and other structured materials fall in an intermediate area between rock and soil mechanics. They exhibit complex behaviour and have characteristics due to bonded structure which are similar to those observed for porous weak rocks.

The term *structure* in soils was first introduced for clays by *Mitchell (1976)*, and then described by *Burland (1990)* as being the combination of bonding and fabric. For granular soils, such sands, bonding can only be related to interparticle cementing since, unlike clays, interparticle forces are usually insignificant.

Bonding in sands can arise from many natural causes, such as precipitation of small amounts of agents, like silica, hydrous silicates, hydrous iron oxides, and carbonates deposited at particle contacts. Another source of bonding may come from improvement of soil properties by means of chemical grouting, cement grouting, and cement stabilization.

Leroueil & Vaughan (1990) concluded that the strength and stiffness which come from the cementation or bonding between particles, cannot be accounted by porosity and stress history alone, which are the basic concepts of soil mechanics. For this reason, bonded soils have typically been treated as special cases, and the understanding of their behaviour has lagged behind that developed for unstructured soils.

Recently, however, many researchers have been giving important experimental contributions to the understanding of these type of materials, highlighting the common features of their behaviour. *Leroueil & Vaughan (1990)* reported the similarities of behaviour between natural soils and weak rocks, showing in particular the effect of bonding on stiffness and strength. According to the authors, concepts related to the structure of bonded soils should be included among the general concepts of soil mechanics (i.e. initial void ratio and stress history) and they should be considered of comparable importance.

In geotechnical practical engineering, properties of cemented soils have received considerable interest in recent years, due to the fact that many natural soils are weakly cemented, and due to the increasing use of artificially cemented soil in civil engineering works. There is yet, however, still many issues about appropriate design procedures for foundations, slopes, and tunnels in sites where these materials are involved.

Conceptual and mathematical models able to describe the behaviour of soils and rocks are necessary to bring any study of this type of materials at a practical level of engineering. In the particular case of naturally or artificially bonded soils, like cemented sands, an understanding of the way in which bonded structure influence the behaviour of these materials is required to formulate constitutive models that can adequately predict their response.

This work address the development and validation of a constitutive model able to simulate the observed behaviour of bonded granular materials. The model is based on a composite material consisting of two different components that interact between each other: the sand matrix and the bonding material. With this approach, it is intended to include some microscopic aspects of the cemented soils to the framework of classical soil mechanics where macroscopic point of view is prevalent.

Each of the two component materials have their own properties and particular behaviour. Due to the typical brittle behaviour of cementitious materials, the bonding material is modeled within the framework of elastic-degrading and damage theory (*Carol et al., 1994)*. For its part, the sand matrix is modeled within the framework of classic elastoplasticity. For these reason this model is considered as a coupled damage-elastoplastic model.

The main objectives of this work can be summarized as follow:

- Review of the bibliography on the behaviour of cemented sands and modelling of these materials, summarizing the main aspects to be taken into account for the formulation of the composite model.
- Review of classical elastoplasticity and damage theory applied to soil mechanics.
- Development of a coupled damage-elastoplastic model based on a composite material, able to simulate the cemented sands behaviour.
- Numerical implementation of the model in the Finite Element code *Code_Bright* (*Olivella et al., 1994, 1996*) using a Stress Point Algorithm *(Vaunat et al., 2000*).
- Validation through comparison with reported laboratory tests, highlighting the aspects that still need to be improved.

The document consists on five chapters. This first introductory chapter follows with the review of the bibliography on the behaviour of cemented sands. In Chapter 2, the classic elastoplasticity and elastic degrading theory are presented. The formulation of the coupled model is developed in Chapter 3 and some simulated tests are shown to describe the model performance. In Chapter 4, some reported test are simulated and compared with experimental data. Finally, in Chapter 6, results are discussed and conclusions and possible futures lines of work are proposed.

1.2.- Literature review: cemented sands behaviour

The behaviour of cemented sand has been studied by many investigators since the early 1970s, most of them motivated by the use of cement in the treatment of sand (e.g.: *Chiang & Chae, 1972*; *Mitchell, 1976; Clough et al., 1981*). There are also many papers dedicated to understand the behaviour of naturally cemented sands based on laboratory testing of natural soil specimens obtained from the field (e.g.: *Airey & Fahey, 1991; Lagioia & Nova, 1995; Cuccovillo & Coop, 1997, 1999*). It was shown that this approach presents some difficulties resulting from the disturbance of the structure occurring during the sampling process. Therefore some investigators used, as alternative, artificially cemented specimens, mixing the soil with a cementitious agent (*Dupas & Pecker, 1979; Coop & Atkinson, 1993; Cuccovillo & Coop, 1993*).

After a thorough review of the available bibliography, several convergences can be identified in the observations and conclusions provided by the different researchers. The most important are:

- The behaviour and the failure mode of cemented sands is strongly influenced by the amount of cementing agent, sand density at time of bonding deposition and confining pressure. Grain size distribution and grain arrangements also plays important roles.
- The basic trends observed for the naturally cemented sands were also exhibited by the artificially cemented sands.
- There is distinct type of transition from brittle to ductile failure mode as the confining pressure increases. The reason for the transition from brittle to ductile failure mode appears to be related to the relative contributions of the cementation and frictional components to the sand response. At low confining pressures, the cementation component is far more significant than the frictional component. Because of the brittle failure of the cementation bonds, the sand itself exhibits brittle failure in this pressure range. At high confining pressures, in depends on the cement content. In the case of weakly cemented sands, the frictional component of strength becomes dominant and more ductile response results. In the case of a strongly cemented sand, the cementation is the most significant component of resistance even at these high pressures, and thus, a brittle mode is observed at low and high confining pressures.
- Cementation in sands has the basic effect of adding a cohesion and a tensile strength to the material. Cementing also gives the soil a substantial unconfined compressive strength. The friction angle can be taken as a constant for any cement content and they are close to the uncemented sand friction angle, showing that friction is mainly provided by contacts at sand grains. Peak strength increase and the strain at peak decreases with higher cement contents.

- The presence of cement in the sand results in higher shear stiffness and a larger elastic range than the uncemented soil. The shear modulus always increases with increasing cementation level, but the increase rate is not constant from low to high cementation levels. A departure from linearity was observed well before the yield point, which can be associated to the breaking of the weaker and more highly stressed bonds. After yielding, a more rapid progressive breakdown of the bonds occurs. During the process of bond degradation, the shear modulus is significantly reduced.
- The increase in the initial bulk modulus caused by an increase in cement content is much more pronounced at lower curing void ratios, and the bulk moduli tend to a unique low value as the curing void ratio increases.
- In isotropic compression tests, the cementing allows the soil to reach states outside the normal compression line of the destructured soil. The paths all follow a post-yield compression line that is unique for each degree of cementation and which converges with the intrinsic compression line of the uncemented soil as the isotropic stress increases
- For specimens cured at the same void ratio the yield stress in isotropic compression increases with increasing cement content. For specimens with the same cement content, the yield stress increases with reducing void ratio during curing. This may arise from an increase in density resulting in an increase in the number of contact points between the soil particles where the cement can form a bond.

Dupas & Pecker (1979) described the extensive laboratory testing related to the construction of a nuclear power plant at Koeberg, South Africa. Preliminary studies showed that the layer of medium-dense saturated sand over which the power plant would be situated was susceptible to liquefaction. The authors noted that by adding a small amount of cement to the sand, it was possible to obtain a material with strong enough chemical bonds between the sand grains to prevent liquefaction.

From results of several triaxial tests performed, *Dupas & Pecker (1979)* observed that the friction angle in cemented sands could be taken equal to the sand friction angle, showing that friction is mainly provided by contacts at sand grains. On the other hand, they observed that cohesion increase with dry density, time, and cement content. The values of cohesion resulting from different tests are presented in Fig. 1.1.

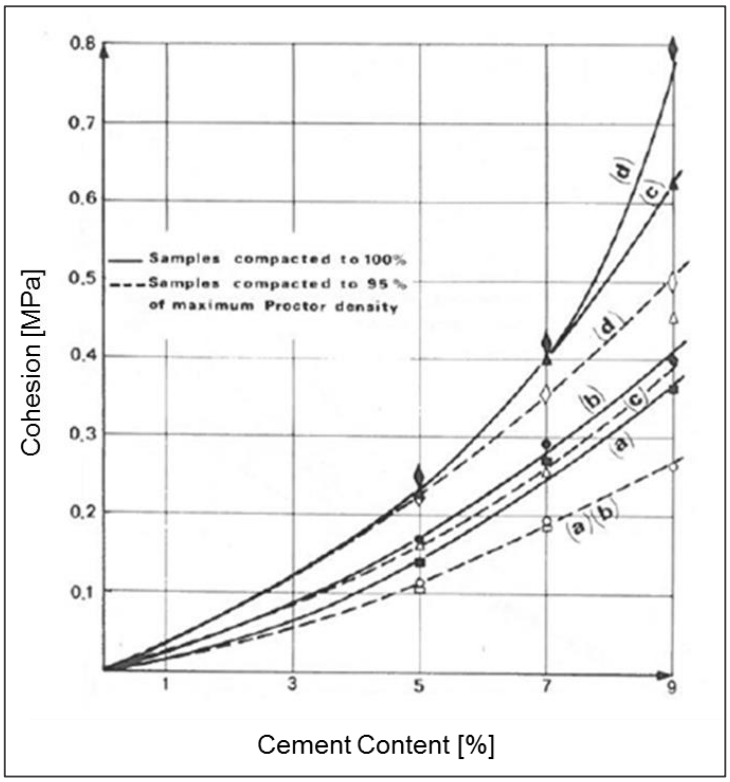

Figure 1.1: Variation of cohesion with cement content and density (after *Dupas & Pecker, 1979*)

Clough et al. (1981) present the tests performed on four naturally cemented sands found in San Francisco Bay Area, motivated by the question of stability of steep natural slopes located along the California coast. The authors also tested samples of artificially cemented sands fabricated to simulate the natural soil behaviour. The peak strength envelopes of both cemented and uncemented soils obtained by *Clough et al. (1981)* are essentially straight lines (Fig. 1.2). As the amounts of cement increases, the cohesion intercept increases, in agreement with the results obtained by *Dupas & Pecker (1979)*. They concluded that cementation in sands has the basic effect of adding a cohesion intercept and a tensile strength to the sand, increasing its stiffness, but not changing its friction angle significantly.

Typical stress-strain curves given by *Clough et al. (1981)* for two naturally cemented soils obtained in drained triaxial compression tests are presented in Fig. 1.3. These soils were considered as strongly and weakly cemented sands. The strongly cemented soil showed a brittle failure behaviour at all confining pressure levels, whereas the weakly cemented soil demonstrate a transitional response from brittle to ductile failure as confining pressure increase. For the artificially cemented sand, *Clough et al. (1981)* also observed that there is a distinct transition from brittle to ductile failure as the confining pressures increase, and that occurs earlier for the less cemented sand. The authors suggested that the reason for the transition from brittle to ductile failure modes appears to be related to the relative contributions to the sand response by the cementation and frictional components of the deformation resistance mechanism.

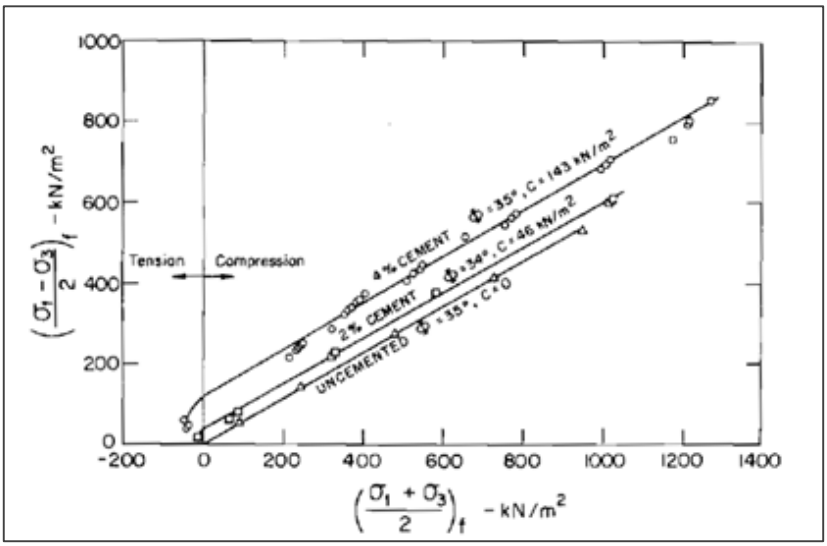

Figure 1.2: Peak strength envelopes for uncemented, 2% and 4% cement contents specimens (*Clough et al., 1981*)

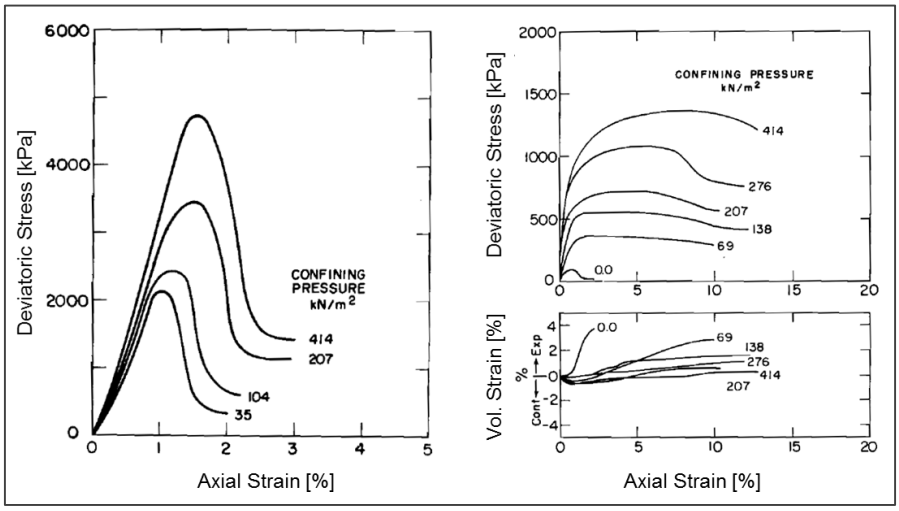

Figure 1.3: Typical stress-strain curves for strongly (left) and weakly (right) naturally cemented sands (after *Clough et al., 1981*)

Acar & El-Tahir (1986) intended to assess the development of dynamic shear modulus with artificial cementation. Fig. 1.4 shows the results obtained by the authors for the variation of maximum shear modulus with confining stress and cement content. The authors suggested that an increase in the confining stress leads to an increase in the number of particle bonds contributing to the resistance of the specimen to deformation.

Chang & Woods (1992) also tried to identify the most significant factors affecting the low-strain shear modulus of cemented sands. They suggested that, while for dry, clean, uncemented sand, void ratio and average effective confining pressure are two of the most important factors affecting low-strain shear modulus, for the cemented sand, the grain characteristics such as grain size and gradation (which control the number of contact points between soil particles at which the chemical bonds develop), the curing time and temperature (which affects the chemical reaction of cementing materials) were found also significant parameters affecting shear modulus.

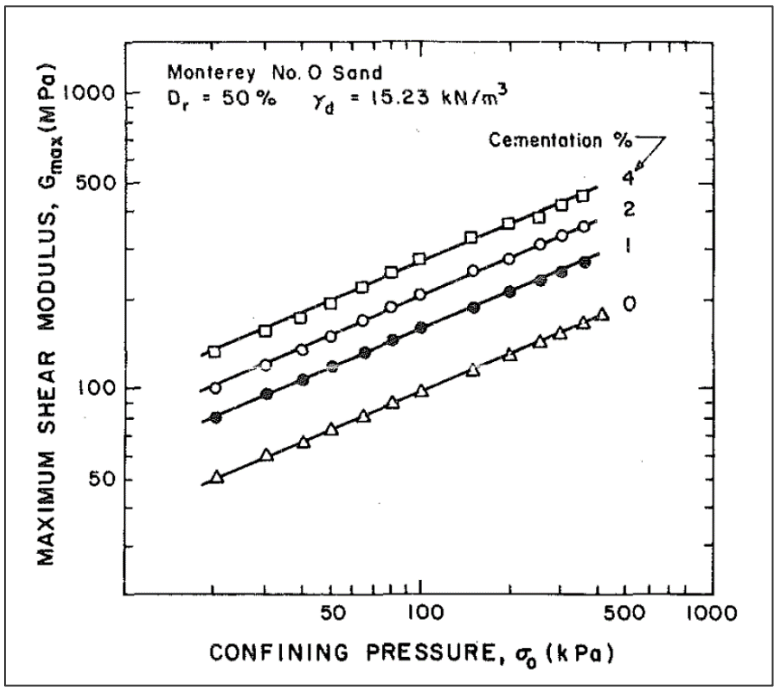

Figure 1.4: Effect of cementation on maximum dynamic shear modulus (*Acar & El-Tahir, 1986*)

Data from *Chang & Woods (1992)* are presented in Fig. 1.5. It qualitatively describe the relationship between cementation level (defined by the authors as the volume of the cementing material divided by the total volume of the initial void space) and the ratio between shear modulus of cemented and uncemented soil for various sands and cementing materials. They observed that the shear modulus of cemented sand always increases with increasing cementation level, but the increase rate is not constant from low to high cementation levels. From this observation, the authors defined three zones according to various increase rates.

Chang & Woods (1992) also study the microstructure of cemented sand by examining scanning electron micrographs. With these observations, the authors suggested that the microstructure of cemented sands could be divided into three stages related to the three zones defined from the increase rates of shear modulus mentioned before. In Zone I (cementation level under 20%-25%), cement partially covers the surface of soil particles with some initial bonding. In Zone II (cementation level between 20%-25% and 60%-80%), cementing of soil particles is very significant at the contact points between soil particles. Finally in Zone III (cementation level over 80%-90%), cement fills most of the void space between soil particles, development of chemical bonds has been completed, and the additional cement mainly plays the role of a filler. A scheme summarizing these concepts presented by the authors is shown in Fig. 1.6.

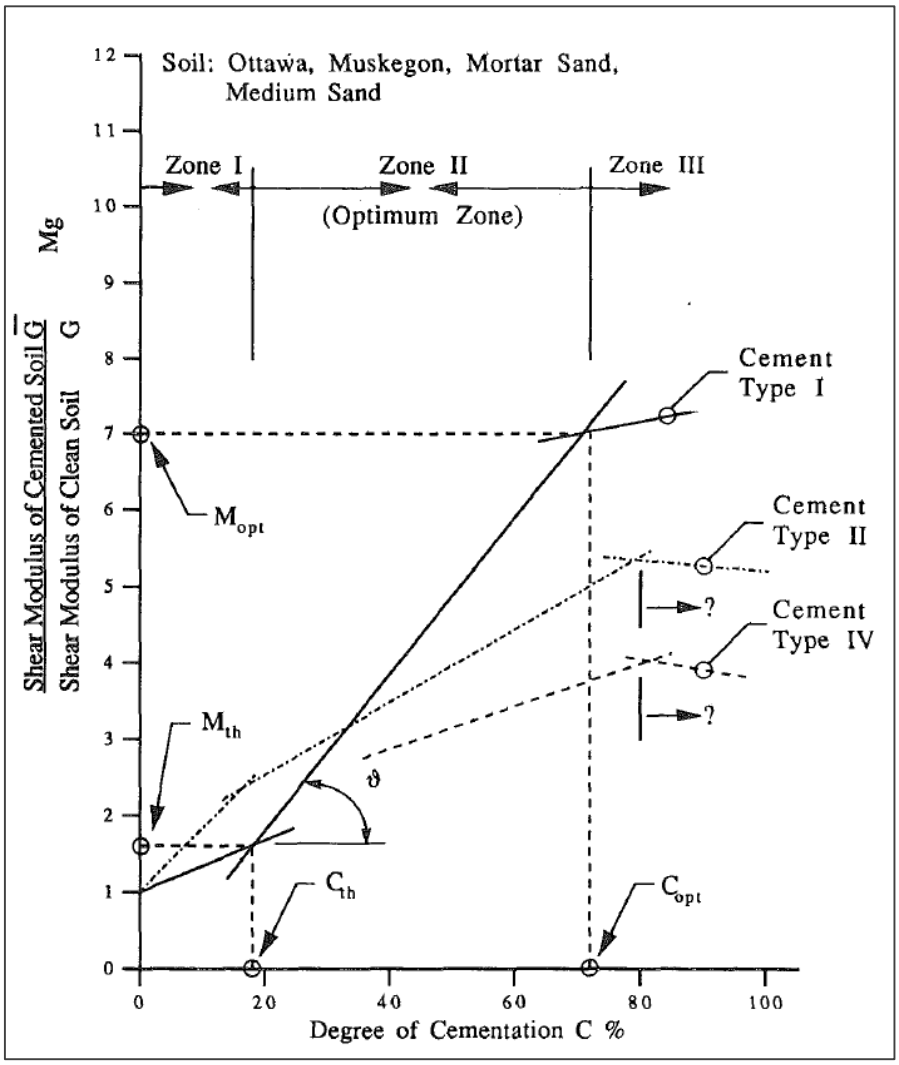

Figure 1.5: Typical evolution of the cemented to uncemented shear modulus ratio with degree of cementation (*Chang & Woods, 1992*)

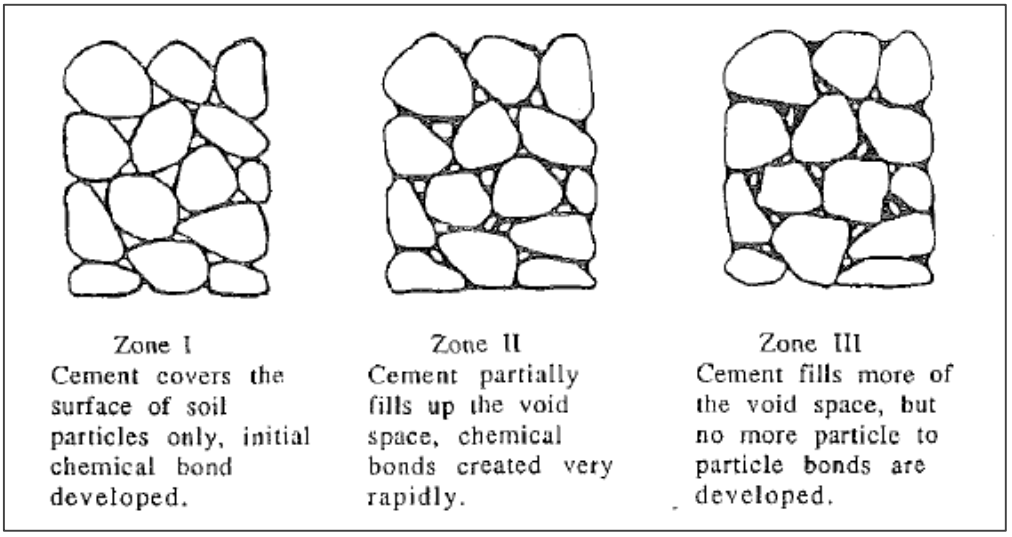

Figure 1.6: Basic cementing phenomenon (*Chang & Woods, 1992*)

Airey (1993) worked with cemented carbonate (calcarenite) soils obtained from the North West Shelf of Australia. Carbonate soils are primarily composed of the skeletal of marine organisms. They have particles of sand to silt size, and are often lightly cemented. This occurs due to carbonate precipitation and the growth of carbonate crystals on the soil grains. The behaviors of several specimens during isotropic compression reported by *Airey (1993)* are shown in Fig. 1.7. The author observed that the specimens showed a stiff response up to a fairly well defined yield point at which large volume strains start to occur. After yield, the slopes of the compression responses approach a unique value, and a normal compression line for the destructured soil can be estimated.

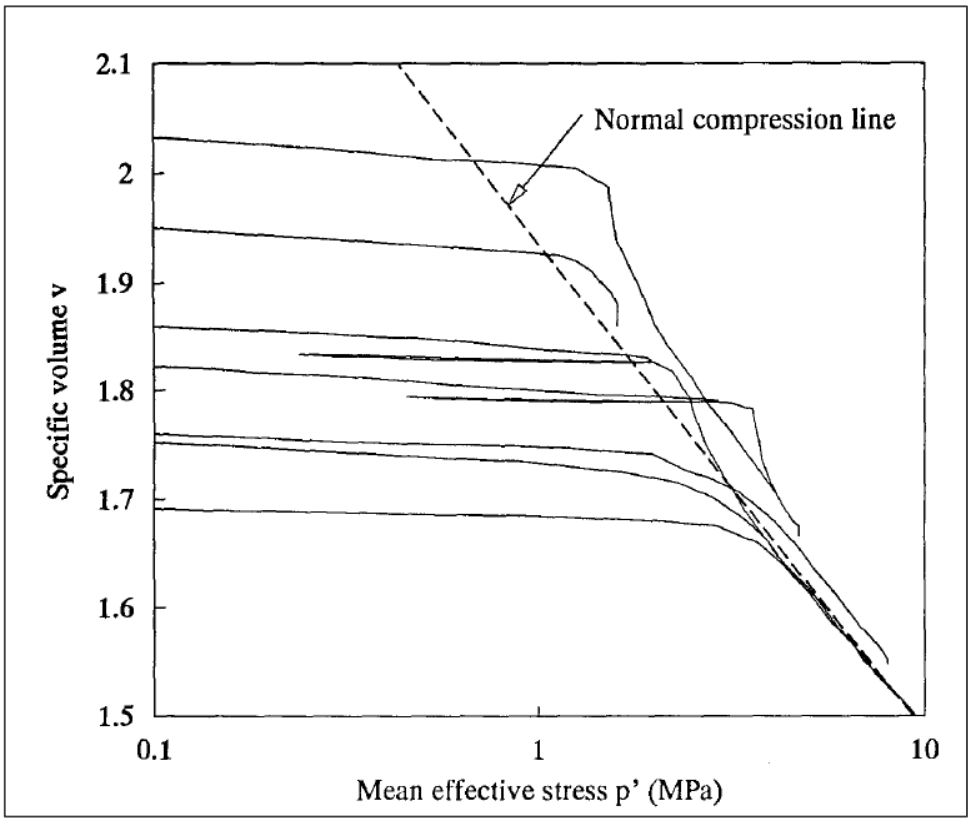

Figure 1.7: Isotropic compression responses of calcarenites (*Airey, 1993*)

Coop & Atkinson (1993) intended to examine the separate effects of cementing and grading changes by conducting tests on a carbonate sand artificially cemented using gypsum casting plaster and on uncemented mixtures of the same sand and gypsum powder. They used carbonate sand from Dog's Bay in Ireland, a biogenic carbonate poorly graded medium sand consisting predominantly of foraminifera and mollusk shells. The soil was mixed with gypsum plaster increasing the fines content from 1% to 24% and the tests were carried out on the sand-plaster mixture either uncemented or cemented.

The isotropic compression response of uncemented samples of sand-plaster mixture reported by *Coop & Atkinson (1993)* is presented in Fig. 1.8 (left). In this figure, it is also shown the compression line given by *Coop (1990)* for Dog's Bay sand without added gypsum fines. The authors observed that the addition of gypsum fines resulted in

samples of considerably smaller specific volume. On the other hand the data for isotropic compression of cemented soils reported is presented in Fig. 1.8 (right). In this case, the authors have noted more distinct yield points than those for the uncemented sand. *Coop & Atkinson (1993)* considered that the higher yield stress of the cemented soil than of the uncemented material is in agreement with the observations of *Leroueil & Vaughan (1990)* in a variety of weak rocks, where the cementing allows the soil to reach states outside the normal compression line of the destructured soil.

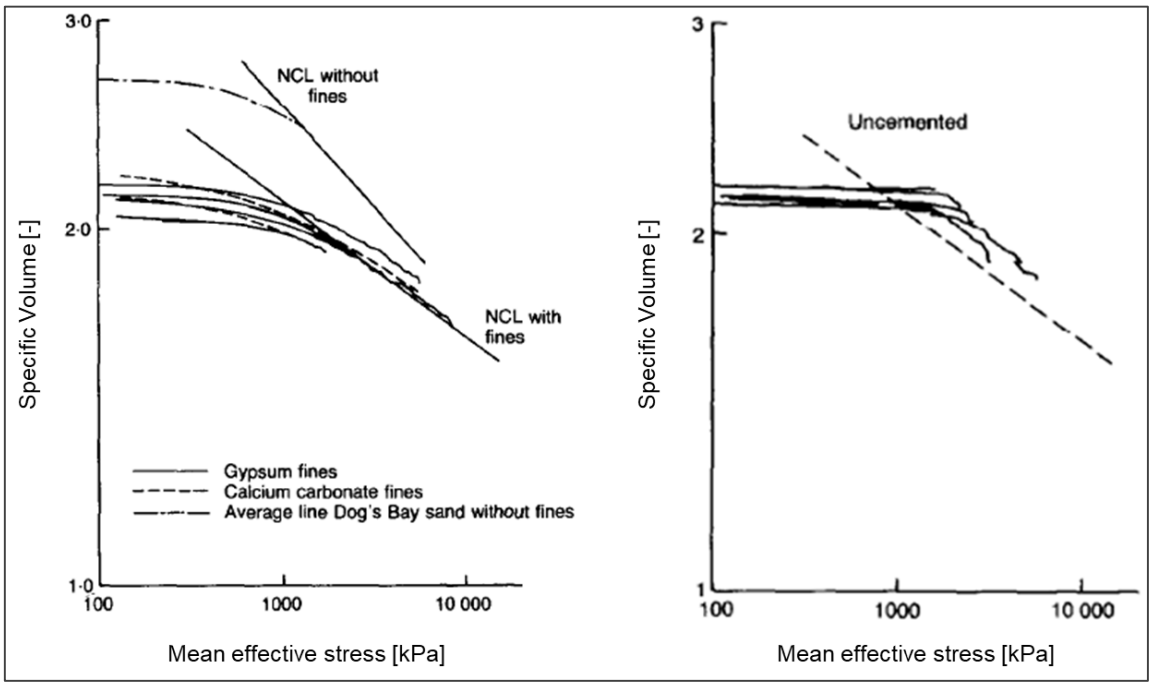

Figure 1.8: Isotropic compression response of uncemented samples with and without fines (left) and cemented samples (right) (after *Coop & Atkinson, 1993*)

From high pressure drained shear tests, *Coop & Atkinson (1993)* found that the stress-strain curves do not have discernible peaks, as the cemented bonds yielded during the initial compression stage of the test and appeared to have little further influence during shearing. At lower stresses, uncemented carbonate soils reach peak states above the critical state line because of dilation, as shown by *Coop (1990)*, but the authors found that cementing results in even higher peak shear stresses. *Coop & Atkinson (1993)* suggested that, at low confining stresses, most of the peak strength results from the cohesive cementing component and that, at higher stresses, the soil becomes purely frictional. They also suggested that this change in shearing behaviour is illustrated by the fact that at the lowest pressure triaxial tests, the peak state is reached at very low strains, followed by rapid strain softening as shear planes formed. As the confining stress increases, the ratio of the peak strength to the critical state strength decreases, and the axial strain at the peak increases substantially, corresponding to a transition from shear plane failure to a barrelling mode.

For the case of intermediate confining pressure levels, *Coop & Atkinson (1993)* concluded that peak occurs at high strains that clearly could not be sustained by an intact cemented fabric. For these tests, the cementing may continue to have some influence on the stress-strain behaviour even after initial yield of the bonds, and the transition from cemented to uncemented modes of failure is not so well defined.

For weak rocks, *Leroueil & Vaughan (1990)* have shown that the stress-strain behaviour of cemented specimens will depend on the position of the initial state of the soil relative to the yield locus of the bonding. Following the same concept, *Coop and Atkinson (1993)* described the idealized behavior of cemented soils, which is divided into three different classes, as illustrated in Fig. 1.9. The first class occurs when the soil reaches its yield stress during isotropic compression, and subsequent shearing should produce behaviour similar to that of an initially uncemented soil, with no yield point. The second class occurs for intermediate stress states, in which the bonds will be intact at the start of the test and they will be broken during shear. The strength is controlled by the frictional component of the equivalent non-structured soil and the stress-strain curve shows a well-defined yield point after an apparent linear behavior. In the third class, the soil is sheared at low confining stresses relative to the strength of the cementing. A peak in the stress-strain curve occurs at low strains and for stresses outside the limit state surface of the equivalent uncemented soil.

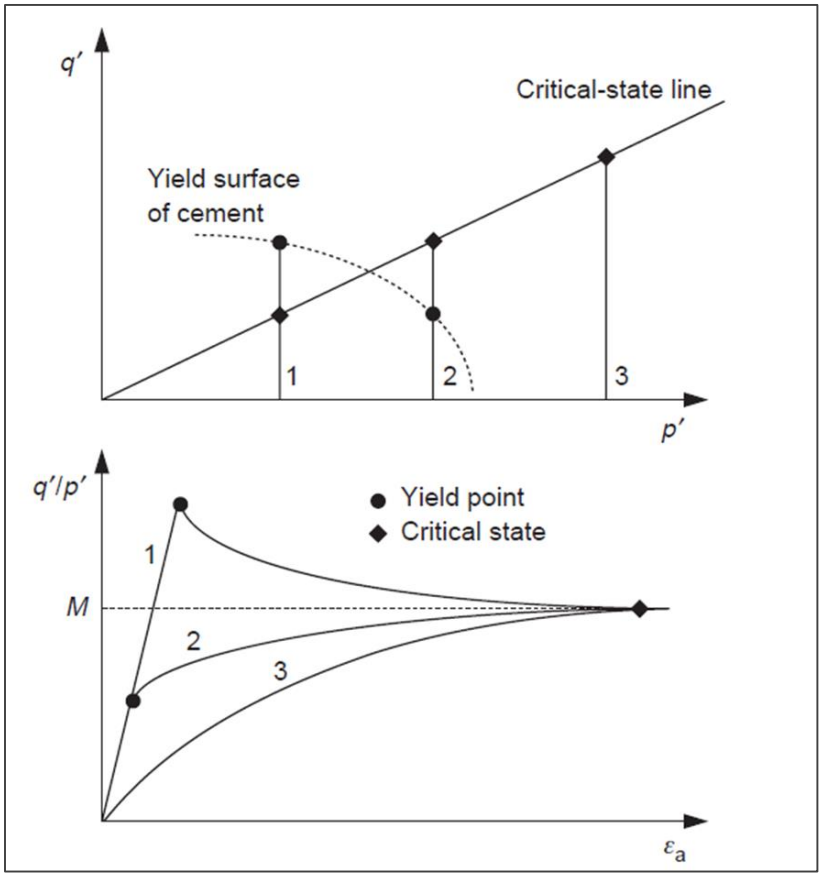

Figure 1.9: Idealized behaviour of cemented soils: (a) stress paths; (b) stress-strain behaviour (after *Coop & Atkinson, 1993*)

Lagioia & Nova (1995) also chose for their research a calcarenite. Results reported by the authors for isotropic compression test are presented in Fig. 1.10. After a linear elastic response, large volumetric strains occurring at an apparent threshold point at roughly constant isotropic pressure were observed. According to the authors, this was the first time that such behaviour has been reported, since previous studies on cemented soils showed a sudden decrease of volumetric stiffness under isotropic pressure but no softening. They suggested that at that threshold point, a collapse of the granular structure of the skeleton takes place with destruction of the intergranular bonds.

The results of drained triaxial tests at high constant cell pressures reported by *Lagioia & Nova (1995)* showed a contracting behaviour which is not affected by the occurrence of destructuration. According to the authors, since the volume is always decreasing even at very large strains, a critical state in the usual soil mechanics sense is not reached. The authors suggested that this is possibly due to the continuous crushing of the calcareous particles, which are weak and brittle. For lower confining pressures (lower than 400 kPa), *Lagioia & Nova (1995)* noted that the destructuration threshold is associated with a peak, and that the lower the confining pressure, the more marked is the peak and more dilatant is the behaviour after peak (Fig 1.11). The authors considered that the test at 400 kPa is close to the transition point between the two types of behaviour observed at low and high confining pressures. They suggested that this could simplistically be considered to give the transition between brittle and ductile behaviour.

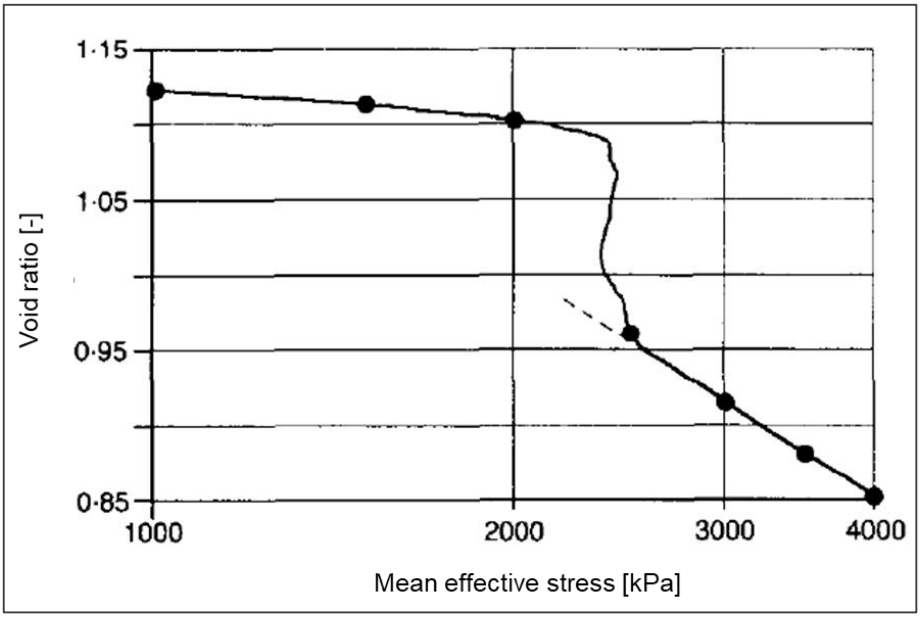

Figure 1.10: Isotropic compression test (after *Lagioia & Nova, 1995*)

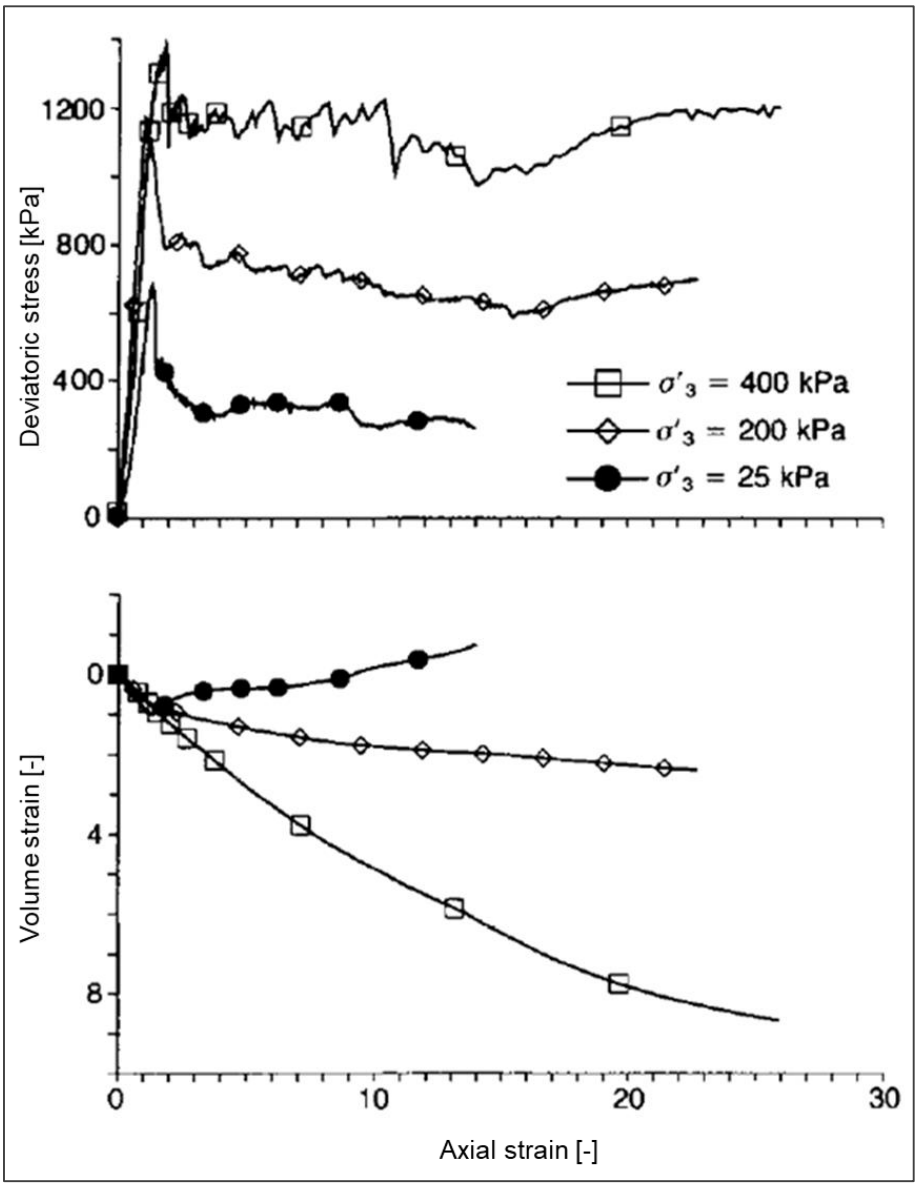

Figure 1.11: Drained constant cell pressure tests (after *Lagioia & Nova, 1995*)

Cuccovillo & Coop (1997 and 1999) compared the behaviour of the calcarenite obtained from the North West Shelf of Australia with a silica sandstone from the Lower Greensand series of Kent in England. The calcarenite consisted of a medium carbonate sand of biogenic origin bonded by calcium carbonate representing a material with weak grains bonded by a comparatively strong cement. In contrast, the silica sandstone was a medium quartz sand bonded by iron oxide representing a material with strong grains bonded by a relatively weak cement.

Thin section of a calcarenite sample under cross-polarized light reported by *Cuccovillo & Coop (1997)* is presented in Fig. 1.12 (left). The authors emphasized the open fabric of the material and suggested that cement precipitation during soil deposition prevented large strains in the material under the increasing overburden stress and leaded to low densities and an open fabric. On its part, the scanning electron micrographs of a thin section of a silica sample reported by *Cuccovillo & Coop (1997)* is presented in Fig. 1.13

(right). In this case, the authors suggested that the cement was formed in the later stages of the diagenesis after high overburden pressures had caused a substantial increase in density leading to the development of a well-defined fabric, characterized by the large area of the intergranular contacts.

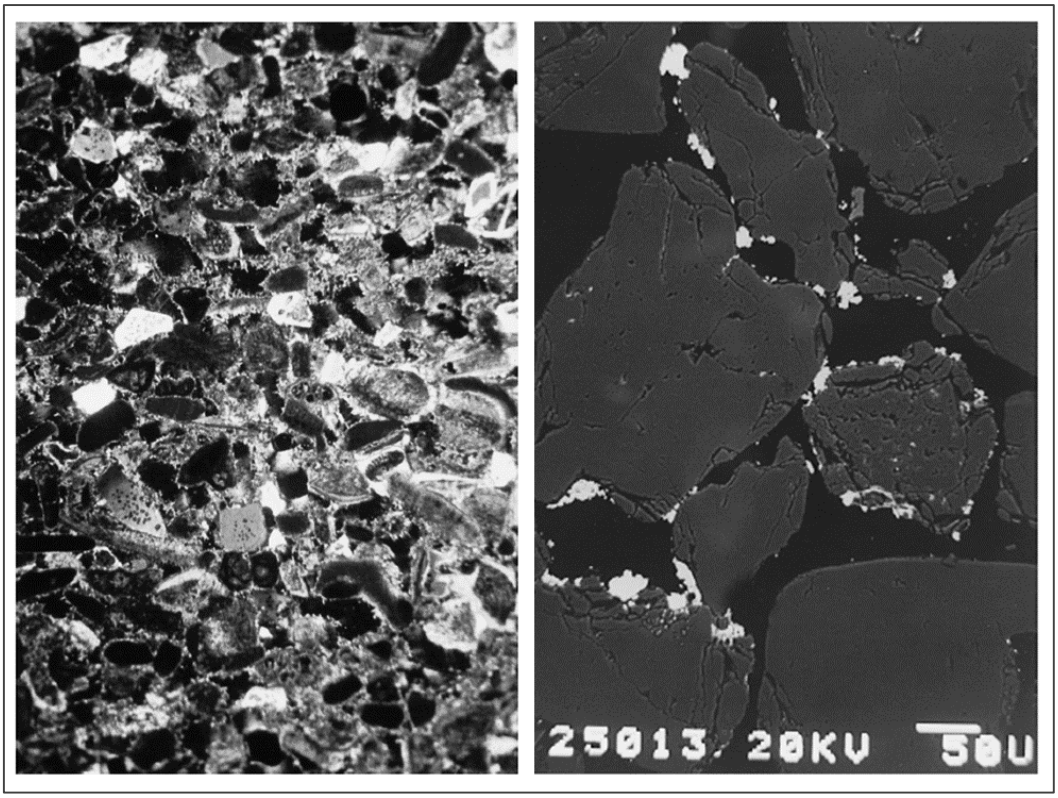

Figure 1.12: Thin section of a calcarenite sample under cross-polarized light (left) - Scanning electron micrograph of the silica sandstone (right) (*Cuccovillo & Coop, 1997*)

Cuccovillo & Coop (1997) dedicated their work to examine the pre-failure behaviour of these materials. They compared the behaviour of intact and reconstituted soils to investigate the influence of structure on the shear stiffness. In Fig. 1.13 (left) is shown the typical variation of shear modulus obtained *Cuccovillo & Coop (1997)* in drained tests for the intact silica samples. A plateau followed by a very rapid decrease of stiffness as failure is approached can be observed. In the case of the undrained shearing cycles tests, different observation were made depending of the maximum deviatoric stress reached in the probes. For the set of probes performed up to a deviator stress of 6000 kPa, a continued decrease in the deviator stress at yield was observed in each cycle (Fig. 1.13 right). The last reloading of this last series of probes caused a reduction of the shear modulus of almost 30%, which, according to the authors, reflect the extent of bond degradation in the material.

Comparisons made by *Cuccovillo & Coop (1997)* between the intact and reconstituted soils response, leaded them to conclude that the presence of bonding in the intact material resulted in higher shear stiffness and a larger elastic range than the reconstituted soil. In the silica sandstone, the cement was likely to be disrupted after isotropic load before shearing, but despite this, large difference of stiffness between

intact and reconstituted soil were observed. The authors suggested that the influence of fabric appears to be the main factor explaining this difference. For the case of calcarenite, they concluded that since the soil had not developed a pronounced fabric, any difference in response between the intact and reconstituted soils can therefore be attributed to the bonding alone.

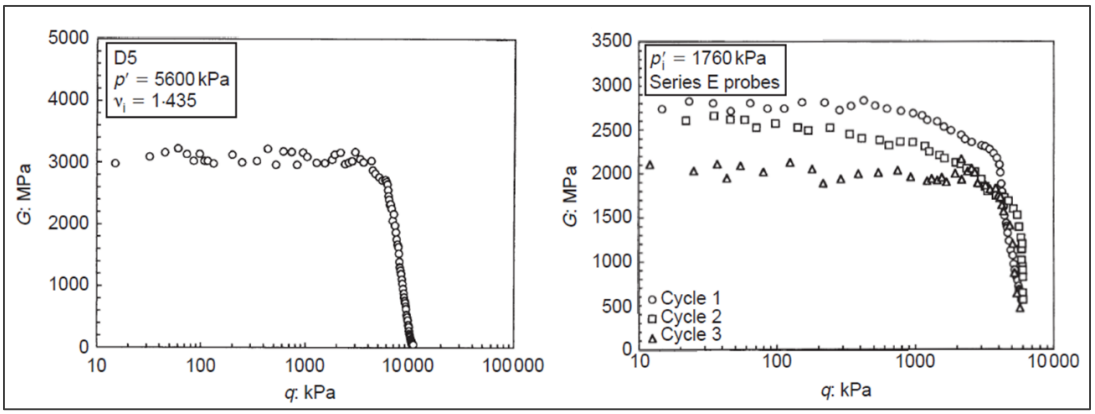

Figure 1.13: Evolution of shear modulus “G” with deviatoric stress “q” for the intact silica in drained triaxial test (left) and undrained triaxial cycles test (right) (*Cuccovillo & Coop, 1997*)

Isotropic compression tests on the intact and reconstituted soils were reported also by *Cuccovillo & Coop (1997)*. The results for the calcarenite are shown in Fig. 1.14. They found that the isotropic boundary of the intact soil (Intact IB) lay to the right of the normal compression line (NCL), reaching states which were impossible for the reconstituted soil. They also noted that the offset between the isotropic boundaries of the intact and reconstituted soils reduced as the specific volume decreased, until the two boundaries became coincident.

In *Cuccovillo & Coop (1999),* the authors presented a schematic representation of the isotropic compression behaviour observed (Fig. 1.15). The authors suggested that the difference in the behaviour of the strongly and weakly cemented soils was that the strongly bonded soil can reach states outside the NCL defined by the uncemented soil, while the weakly bonded soil yielded before reaching the NCL.

Cuccovillo & Coop (1999) extends the work made previously to examine the behaviour at larger strains performing different triaxial tests. The effect observed when the confining pressure is increased for both structured sands, was a transformation of the shear behaviour from strain-softening to strain-hardening. For the calcarenite, the authors observed that the peak states were practically coincident with yielding and were followed by a rapid loss of strength and volumetric compression. They suggested that this is a clear indication of the cohesive nature of the peak strength of this structured sand. Conversely, for the silica sandstone, they observed that the peak responses were accompanied by dilation and plastic strains that developed after the soil had yielded and the bonds had started to degrade. They suggested that in these cases, the peak strengths are frictional.

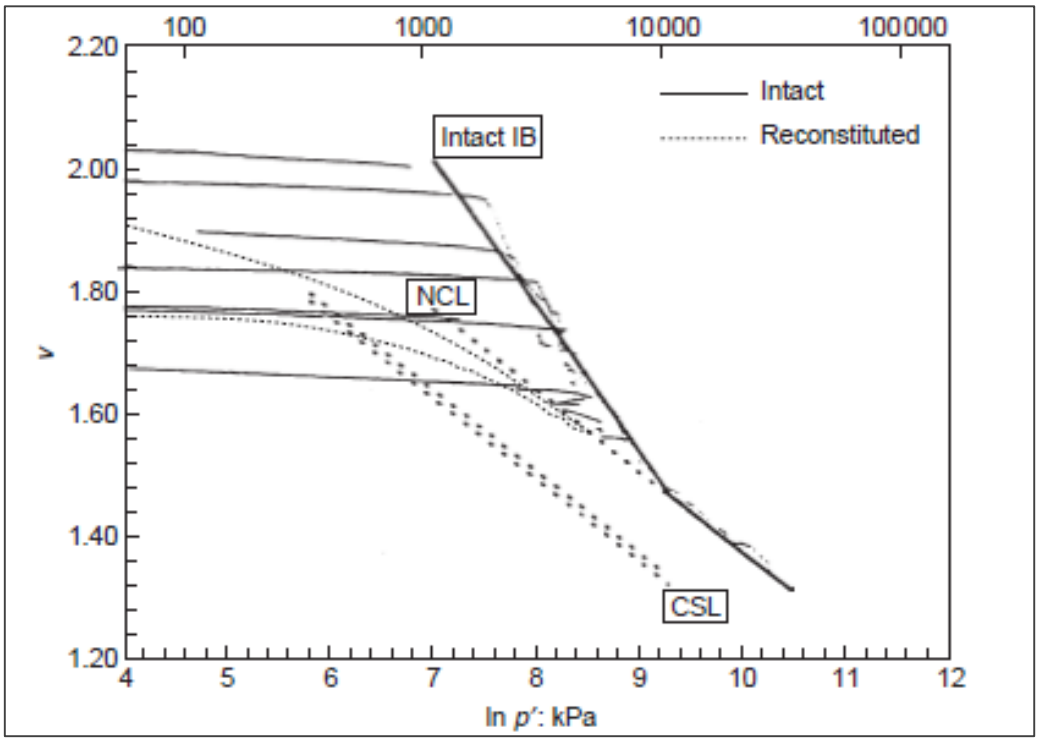

Figure 1.14: Isotropic compression data and state boundaries for intact and reconstituted calcarenite (*Cuccovillo & Coop, 1997*)

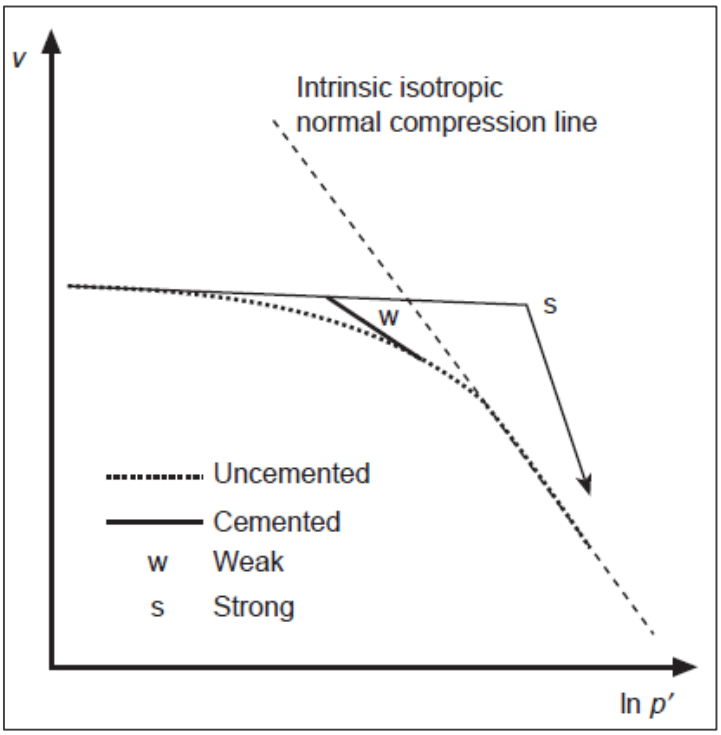

Figure 1.15: Schematic of isotropic compression response of weakly and strongly cemented sands (*Cuccovillo & Coop, 1997*)

In the early 2000s, *Consoli et al. (2000)* suggested that differences between measured results in the laboratory and those deduced from field behaviour, that were frequently explained by sample disturbance in previous studies, may also be due to the testing techniques employed. The authors considered that, although the cemented structure found in many in situ soil deposits was formed under stress, in the usual testing techniques, cementing under stress has not been considered until that moment. The authors devoted their work to prove the importance of acting stresses during the formation of cemented bonds to the behaviour of natural and artificially cemented soils.

In the same context, *Rotta et al. (2003)* simulate the formation of a cemented sedimentary deposit in which cement bonding occurs after burial and under geostatic stresses. The soil samples used come from weathered sandstone obtained from the region of Porto Alegre, in southern Brazil, and specimen were prepared with different cement contents. The curing confining stresses ranged from 50 to 2000 kPa, and were intended to represent soil elements at different depths in the fictitious sedimentary deposit when the cementing occurred.

In Fig. 1.16 isotropic compression tests results reported by *Rotta et al. (2003)* are shown for the specimens with 1% and 3% of cement content considering curing stresses at 100, 250, 500, and 1000 kPa. The authors observed that, for the specimens prepared with the same cement content, the stress increment necessary to cause a given reduction in void ratio increases as the curing stress increases. This was corroborated by the authors by plotting the initial bulk moduli against curing void ratio (void ratio at the moment of formation of the cement bonds) as shown in Fig. 1.17. This plot also allows the authors to distinguish an interactive effect of the curing void ratio and the cement content on the pre-yield volumetric stiffness. It was observed that the increase in the initial bulk modulus caused by an increase in cement content is much more pronounced at lower void ratios, and that the bulk moduli tend to a unique low value as the curing void ratio increases.

Rotta et al. (2003) also noted that after primary yield, the paths all follow a post-yield compression line that is unique for each degree of cementation and which converges to the intrinsic compression line of the uncemented soil as the isotropic stress increases. This was in agreement with previous works like *Cuccovillo & Coop (1999)* for natural calcarenites, but it can be seen in this case that convergence would occur eventually, but not before an isotropic stress as high as 30 MPa had been reached, regardless of the cement content.

With respect to the apparent yield stress, *Rotta et al. (2003)* made three basic conclusions: (1) for specimens cured at the same void ratio the primary yield stress in isotropic compression increases with increasing cement content; (2) for specimens with the same cement content, the primary yield stress increases with reducing void ratio during curing (this may arise from an increase in density resulting in an increase in the number of contact points between the soil particles where the cement can form a bond); and (3) the relative contribution of cementation to the primary yield stress in isotropic compression decreases with void ratio during curing.

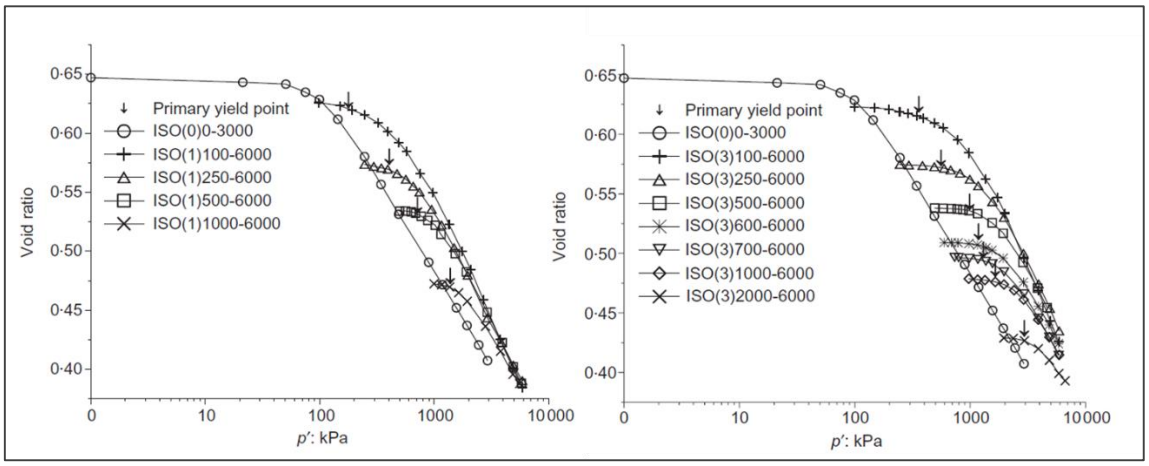

Figure 1.16: Isotropic compression test for specimens with 1% (left) and 3% (right) cement content (*Rotta et al., 2003*)

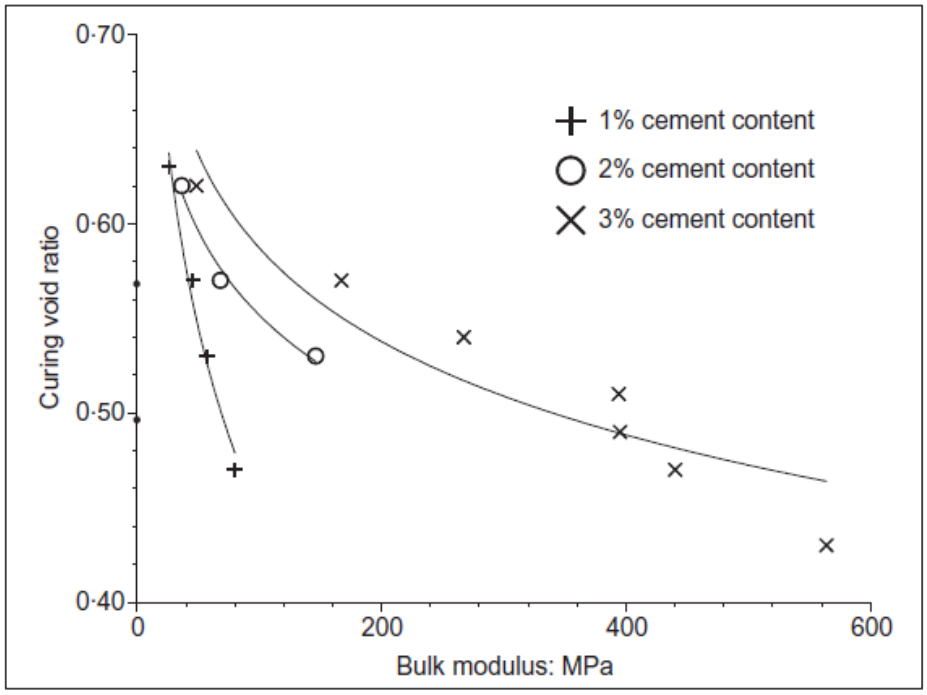

Figure 1.17: Variation of initial bulk modulus with curing void ratio (*Rotta et al., 2003*)

Consoli et al. (2006) complement the work made by *Rotta et al. (2003)* by unconfined compression tests carried out on the same artificially cemented soil. Similar patterns to that described in the previous work by *Rotta et al. (2003)* were observed. There is a roughly linear increase in the unconfined compressive strength caused by cement addition, which is much more pronounced at lower curing void ratios. They also observed that the unconfined compressive strength tends to a narrow range as the curing void ratio increases, clearly evidencing the expected coupled effect of density and cementation on the strength of bonded soils.

Dalla *Rosa et al. (2008)* extend the work made by *Consoli et al. (2000, 2006)* and *Rotta et al. (2003)* to triaxial conditions. The curing was performed under three different confining pressures, 50, 250 and 500 kPa, which presents the advantage (apart from the samples cured at 50 kPa) to be cured from points on the isotropic normal compression line for the uncemented soil. Standard drained tests were carried out, at confining pressures either equal to or different from the curing stress.

The stress–strain response reported by *Dalla Rosa et al. (2008)* for the specimens with 2% cement content are shown in Fig. 1.18. They observed that as the confining stress increased the volumetric response of the soil became increasingly contractive, and the increase in peak strength reduced. According to the authors, the cement seems to have more effect at low shearing confining pressures, independently of the curing stress.

Dalla Rosa et al. (2008) noted that, for samples cured at higher stresses, the peak strength is consistently higher than that of samples cured at lower stresses, but they suggested that this effect could be a result of the lower void ratio at the start of shearing. On the other hand, they observed that the samples cured at lower stresses and sheared at 500 kPa must have suffered damage in the cemented bonds. In these samples, a less pronounced strain-softening behaviour and lower stiffness were observed and attributed by the authors to damage of bond during isotropic loading.

Finally *Dalla Rosa et al. (2008)* suggested that the state boundary surface is independent of curing stress when the curing stress is on the isotropic compression line of the uncemented soil. This is consistent with the results presented by *Rotta et al. (2003)* where the isotropic compression curves of the uncemented and cemented material are almost parallel and slightly convergent. These observations are also in agreement with suggested frameworks for structured soils, where the state boundary surfaces of structured soils and their reconstituted counterparts are similar in shape but different in size, by a factor equal in magnitude to the degree of structure of the soil.

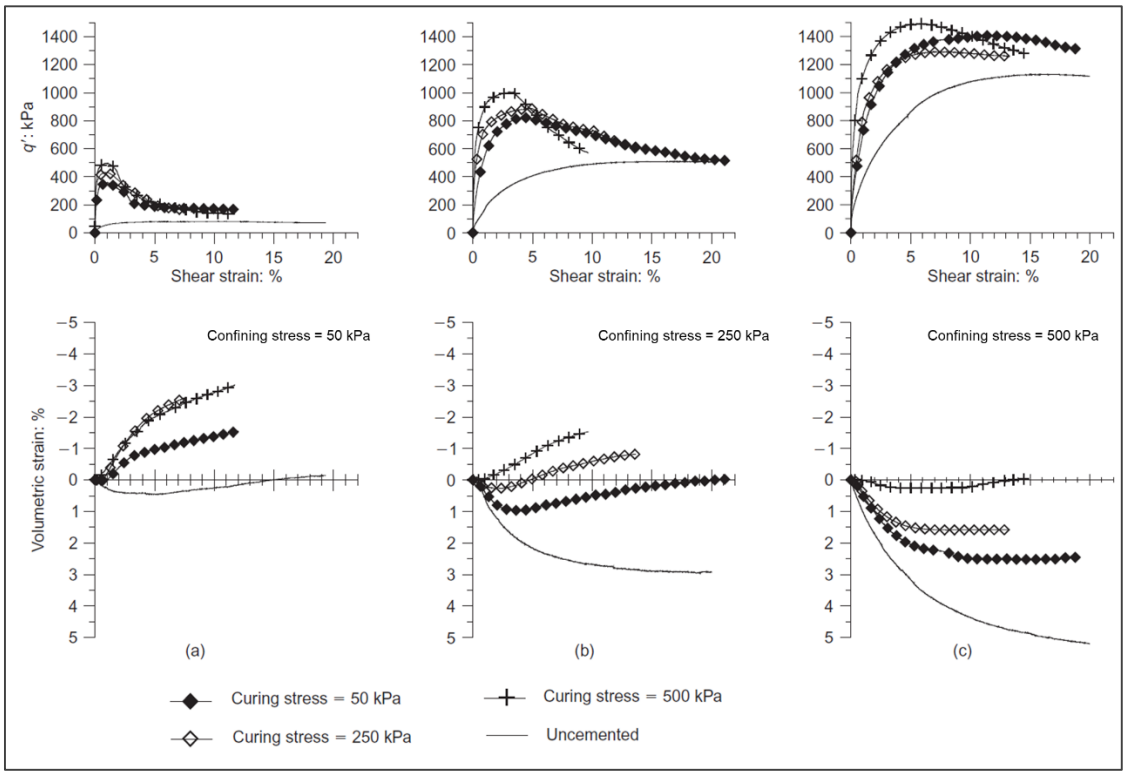

Figure 1.18: Drained triaxial tests for different curing and confinement stress for specimens with 2% cement content (Dalla Rosa *et al., 2008*)

1.3.- Literature review: modelling cemented sands

Gens & Nova (1993) presented the basic conceptual requirements for the development of a constitutive model for bonded soils. The model developed use as starting point a constitutive law for the unbonded material that is modified according to the magnitude of bonding. The degradation process is simulated then by the reduction of degree of bonding that, according the authors, depends on the increase of a damage measure.

The approach described by *Gens & Nova (1993)* consists in simulating the observed behaviour of the bonded material in relation with the behaviour of the equivalent unstructured one. In order to take into account these observations, the authors proposed a way to modified, according the amount of bonding, the yield surface valid for the behaviour of the soil in an unbonded state. The experimental observation showed that higher stresses could be applied to a bonded material without causing it to yield and that bonding also provides the soil with real cohesion and tensile strength. For these reason, in the formulation of *Gens & Nova (1993)*, as bonding increase, the yield surface grows towards the right and enlarges also to the left on a p-q- space.

In the model described by *Gens & Nova (1993),* the new structured yield surface (Fig. 1.19 top) is defined by two variables, p_{co}, that controls the yielding of the bonded soil in isotropic compression, and p_t, representing the tensile strength of the material. According the authors, both parameters increase with the magnitude of bonding, represented by the parameter b, and they proposed the corresponding dependency's $p_{co}(b)$ and $p_t(b)$.

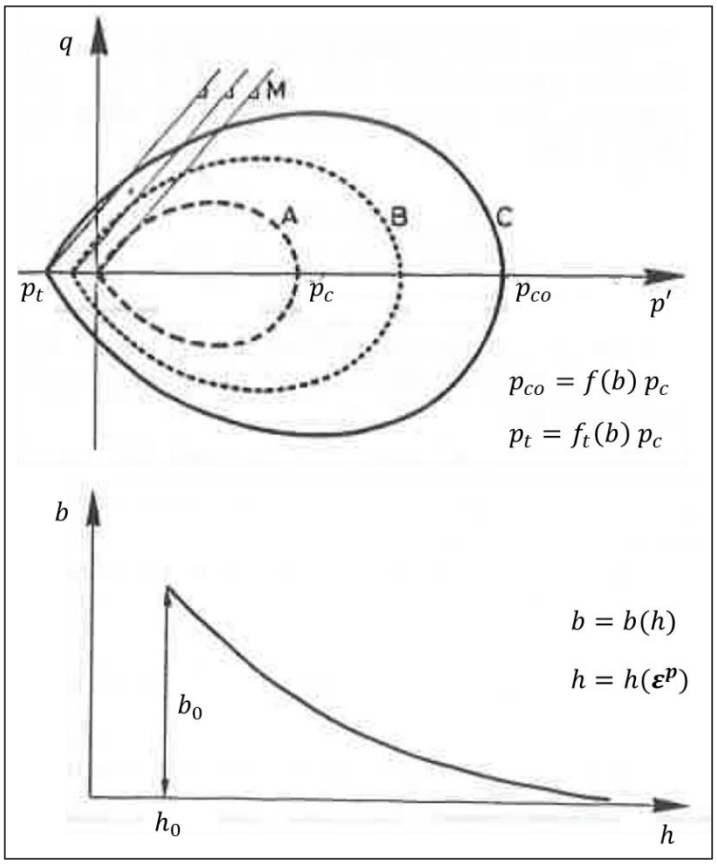

Figure 1.19: Yield surfaces for different degrees of bonding (top); and reduction of bonding with damage (bottom) (after Gens & Nova*, 1993*)

According to *Gens & Nova (1993)*, the evolution of the yield surface when bonding is destroyed is not an easy definition, since debonding may occur in different ways in different specimens. They assume that the yield loci changes due to a combined effect of conventional unbonded plastic hardening (or softening) and bond degradation. The term related to bond degradation was assumed to depends on a kind of damage measure k. In Fig. 1.19 (bottom), the reduction of bonding with increasing damage proposed by the authors is plotted. In addition, the authors propose that the damage parameter must be monotonically increasing with plastic strains.

Several examples of application were presented by *Gens & Nova (1993)*. In Fig. 1.20 (top), the computed isotropic compression curves for different amounts of initial bonding reported by the authors are shown. It can be observed that the authors could represent with their model important aspects of bonding material. A higher magnitude of bonding allows the soil to reach higher value of mean stress before yielding and with stress increase, eventually the compression curve converge towards that corresponding to the unbonded soil. The authors also observed that examining in detail the compression curve, three contributions to the magnitude of the strain can be distinguished as shown in Fig. 1.20 (bottom).

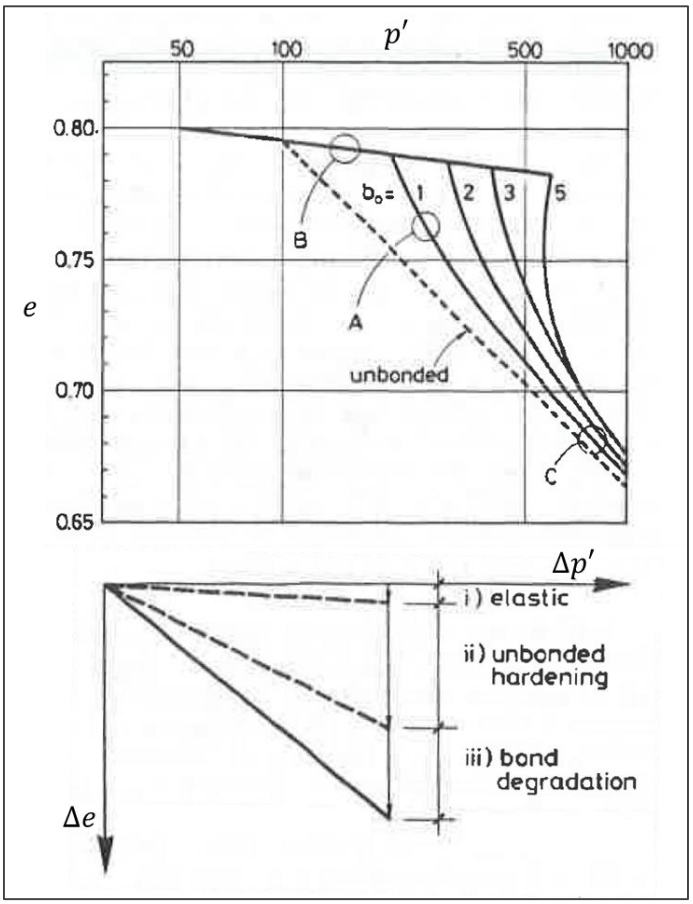

Figure 1.20: Isotropic simulated test for different amounts of bonding (top); and components of volumetric strains (bottom) (after Gens & Nova, *1993*)

Chapter 2

Elastoplastic and elastic-degrading models

The classical formulation of elastoplastic models has been done years ago, and a well-established and unified theoretical description can be found in the classical literature of soil mechanics. The stress-based formulation of elastoplasticity is briefly summarized in this section, with the particular objective of establishing a reference framework for better understanding the developments of the elastic-degrading models.

A unified theory of elastic degradation and damage was presented by *Carol et al. (1994).* This was done considering a "plasticity format" of elastic degradation, taking advantage of the concept of loading function and others concepts related to the well-known elastoplasticity formulation.

The elastic-degrading models, less frequently implemented in geomechanics, are an important component of the coupled model described in this work. Therefore, a detailed summary is presented in this section based on the paper of *Carol et al. (1994)* and *Carol et al. (2001)*, and then, useful definitions like the damage evolution law and the damage evolution rate are proposed.

2.1.- Stress-based formulation of elastoplastic models

The formulation is built around the assumption of a *loading function* F^p (also known as *loading surface*) that can be expressed as Eq. 2.1. The arguments of the function are the stress tensor $\boldsymbol{\sigma}$ and the vector $\boldsymbol{\chi^p}$ containing the variables determining the current configuration of the loading surface (commonly known as *history variables*). Inside the loading surface (i.e. for $F^p < 0$), the response is assumed elastic. On reaching the surface (i.e. $F^p = 0$), plastic deformations develop $\boldsymbol{\varepsilon^p}$.

The rate equations for the stress-based elastoplastic formulation can be derived from Fig. 2.1 and can be expressed as Eq. 2.2 and Eq. 2.3. D_{ijkl} are the components of the elastic stiffness tensor $\boldsymbol{D}$. m_{kl}^p is the *flow rule* that specifies the direction of the *plastic strain rate* $d\varepsilon_{kl}^p$, and $d\lambda^p$ is the *plastic multiplier* that defines its magnitude.

$$F^p = f(\boldsymbol{\sigma}, \boldsymbol{\chi^p}) \qquad (Eq.\,2.1)$$

$$d\sigma_{ij} = D_{ijkl}\left(d\varepsilon_{kl} - d\varepsilon_{kl}^p\right) \qquad (Eq.\,2.2)$$

$$d\varepsilon_{kl}^p = m_{kl}^p\, d\lambda^p \qquad (Eq.\,2.3)$$

Differentiation of Eq. 2.1 leads to the linearized form of the well-known consistency condition presented in Eq. 2.4a, meaning that during plastic loading (i.e. for $F^p = 0$), the current stress state always remains on the current loading surface. n_{ij}^p, defined in Eq. 2.4b, involves derivatives of the loading function for constant values of the plastic multiplier and history variables, with the geometric meaning of the direction normal to the current loading surface in the stress space.

$$dF^p = n_{ij}^p \, d\sigma_{ij} + \frac{\partial F^p}{\partial \chi_k^p} \, d\chi_k^p = 0 \qquad and \qquad n_{ij}^p = \frac{\partial F^p}{\partial \sigma_{ij}} \qquad (Eq.\,2.4\ a,b)$$

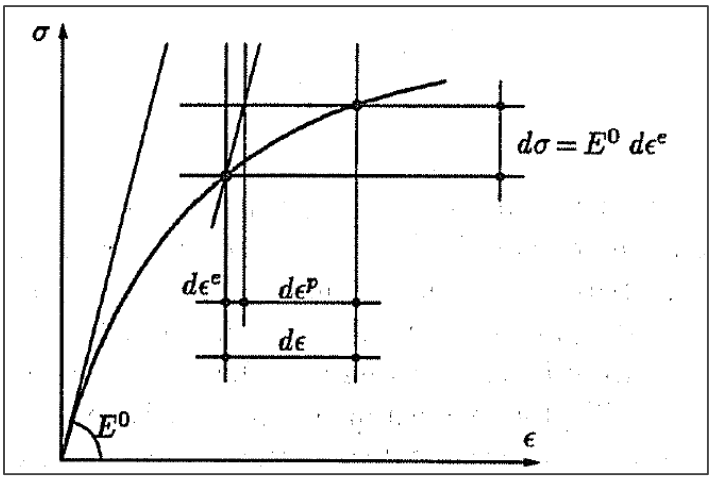

Figure 2.1: Definition of the plastic strain rate *(Carol et al., 1994)*

In the most frequently implemented elastoplastic models, flow rule is expressed in terms of a *plastic potential* Q^p as described in Eq. 2.5. The formulation is called associated in the particular case where m_{ij}^p and n_{ij}^p are collinear. The most common assumption is made when $Q^p = F^p$.

$$m_{kl}^p = \frac{\partial Q^p}{\partial \sigma_{kl}} \qquad (Eq.\,2.5)$$

Assuming that all the parameters contained in the vector of history variables $\boldsymbol{\chi^p}$ are functions of the plastic multiplier, one can define the *history variable rate* $d\chi_k^p$ as expressed in Eq. 2.6a and rewrite the consistency condition as Eq. 2.7. h_k^p in Eq. 2.6b is the *hardening/softening law* and defines the way in which the history variables change when a plastic loading occurs.

$$d\chi_k^p = h_k^p \, d\lambda^p \qquad and \qquad h_k^p = \frac{\partial \chi_k^p}{\partial \lambda^p} \qquad (Eq.\,2.6\ a,b)$$

$$dF^p = n_{ij}^p \, d\sigma_{ij} - H^p \, d\lambda^p = 0 \qquad (Eq.\,2.7)$$

$$H^p = -\frac{\partial F^p}{\partial \lambda^p} = -\frac{\partial F^p}{\partial \chi_k^p} \frac{\partial \chi_k^p}{\partial \lambda^p} = -\frac{\partial F^p}{\partial \chi_k^p} \, h_k^p \qquad (Eq.\,2.8)$$

H^p in Eq. 2.8 is the *hardening/softening modulus*. Note that this parameter is the product of the value of the hardening/softening law at current state (i.e. the way the history variables change when a plastic loading occurs) by the gradient of the current loading function respect of the history variables (i.e. the way the loading function change when a history variables variation occurs). It is a positive value when a hardening regime takes place – corresponding to an expanding loading surface –, and negative if a softening regime occurs – contracting surface. When this value is equal to zero, perfect plastic regime develops, characterized by a loading function that remains unchanged.

The loading-unloading criterion can be written as restrictions in terms of loading function and plastic multiplier as indicated by the three conditions of Eq. 2.9. These conditions lead to two possible situations indicated in Eq. 2.10. The loading criterion takes place when the plastic multiplier increases ($d\lambda^p > 0$) and therefore the loading function would expand, contract or remain unchanged depending on the regime, but always F^p would be equal to 0. On the other hand, the unloading criterion takes place when the loading function is negative, and therefore the plastic multiplier must be null.

$$\begin{cases} F^p d\lambda^p = 0 \\ F^p \leq 0 \\ d\lambda^p \geq 0 \end{cases} \qquad (Eq.\,2.9)$$

$$\begin{cases} loading \quad \rightarrow F^p = 0 \quad if \quad d\lambda^p \geq 0 \\ unloading \quad \rightarrow d\lambda^p = 0 \quad if \quad F^p < 0 \end{cases} \qquad (Eq.\,2.10)$$

The combination of Eq. 2.2, Eq. 2.3, and Eq. 2.7 leads to the classical expression of the plastic multiplier presented in Eq. 2.11. In the numerator of this expression, one can identify the scalar product of the named *trial stress increment* (i.e. the stress increment computed assuming that no increment of plastic strain occurs) with the normal of the loading surface. This product gives a positive quantity when a plastic loading occurs and negative when an elastic unloading takes place. So, for consistency with the sign of the plastic multiplier (positive in loading case) the denominator of Eq. 2.11 must remain always positive. This means that H_{cr}^p defined in Eq. 2.12 is a critical value limiting the softening (negative) modulus. The expression in Eq. 2.11 and the followings are valid if $H^p \geq H_{cr}^p$. By introducing Eq. 2.11 into Eq. 2.3 and Eq. 2.2 one obtains Eq. 2.13 where the elastoplastic tangential stiffness tensor for plastic loading can be identified (Eq. 2.14).

$$d\lambda^p = \frac{n_{ij}^p \; D_{ijkl} \; d\varepsilon_{kl}}{H^p - H_{cr}^p} \qquad (Eq.\,2.11)$$

$$H_{cr}^p = -n_{ij}^p \; D_{ijkl} \, m_{kl}^p \qquad (Eq.\,2.12)$$

$$d\sigma_{ij} = \left[D_{ijkl} \; - \frac{D_{ijmn} \, m_{mn}^p \;\; n_{pq}^p \, D_{pqkl}}{H^p - H_{cr}^p} \right] d\varepsilon_{kl} \qquad (Eq.\,2.13)$$

$$D_{ijkl}{}^{tan} = D_{ijkl} \; - \frac{D_{ijmn} \, m_{mn}^p \;\; n_{pq}^p \, D_{pqkl}}{H^p - H_{cr}^p} \qquad (Eq.\,2.14)$$

2.2.- Plastic format of elastic-degrading models formulation

The characteristic feature of an elastic-degrading material is the existence of a total stress-strain relationship as described in Eq. 2.14a and Eq. 2.14b. D_{ijkl} and C_{ijkl} are in this case the components of the elastic fourth-order secant stiffness and compliance tensor $\boldsymbol{D}$ and $\boldsymbol{C}$.

$$\sigma_{ij} = D_{ijkl}\,\varepsilon_{kl} \qquad or \qquad \varepsilon_{ij} = C_{ijkl}\,\sigma_{kl} \qquad (Eq.\,2.14\,a,b)$$

During unloading-reloading, the material stiffness (or compliance) is assumed to remain constant and equal to its current secant value, regardless of the values of strains and stresses. According to *Carol et al. (1994)*, this fact implies that no micro-crack closure-reopening effects are considered. The secant stiffness and compliance tensor must remain always symmetric to avoid spurious energy dissipation or generation under closed stress or strain paths (*Carol et al., 2001*).

By definition $\boldsymbol{D}$ and $\boldsymbol{C}$ are inverse to each other, leading to Eq. 2.15, where ${I_{ijkl}}^{sym}$ are the components of the symmetric fourth-order identity tensor. Differentiation of Eq. 2.15 leads to the useful relations between the rate of change of stiffness and compliance established in Eq. 2.16 and Eq. 2.17.

$$D_{ijpq}\,C_{pqkl} = C_{ijpq}\,D_{pqkl} = {I_{ijkl}}^{sym} \qquad (Eq.\,2.15)$$

$$dD_{ijkl} = -D_{ijpq}\,dC_{pqrs}\,D_{rskl} \qquad (Eq.\,2.16)$$

$$dC_{ijkl} = -C_{ijpq}\,dD_{pqrs}\,C_{rskl} \qquad (Eq.\,2.17)$$

Analogous to the concept of a plastic loading function, a damage loading function F^d is introduced in Eq. 2.18. As for the elastoplastic formulation, the arguments are the stress tensor $\boldsymbol{\sigma}$ and a vector $\boldsymbol{\chi^d}$ containing the history variables. Inside the loading surface (i.e. elastic domain), the response is assumed elastic and the stiffness (compliance) remains constant. On reaching the loading surface, further degradation may take place and the stiffness (compliance) varies accompanied by increments of degrading strain $\boldsymbol{\varepsilon^d}$.

$$F^d = f\left(\boldsymbol{\sigma}, \boldsymbol{\chi^d}\right) \qquad (Eq.\,2.18)$$

$$d\sigma_{ij} = D_{ijkl}\left(d\varepsilon_{kl} - d\varepsilon_{kl}^d\right) \qquad (Eq.\,2.19)$$

$$d\varepsilon_{kl}^d = m_{kl}^d\,d\lambda^d \qquad (Eq.\,2.20)$$

Equivalent to the plastic strains, the degrading strain rate is defined as the excess strain rate beyond the value that corresponds to the increment of stress according to the current secant stiffness. From Fig. 2.2 one can obtain the equivalent rate equations for the elastic-degrading formulation presented in Eq. 2.19 and Eq. 2.20. Note that, unlike the elastoplasticity formulation, D_{ijkl} denotes the components of the elastic secant

stiffness tensor $\boldsymbol{D}$. Analogous to plasticity m_{kl}^{d} is the *flow rule* and specifies the direction of the *degrading strain rate* $d\varepsilon_{kl}^{d}$ and $d\lambda^{d}$ is the *degrading multiplier* that defines its magnitude.

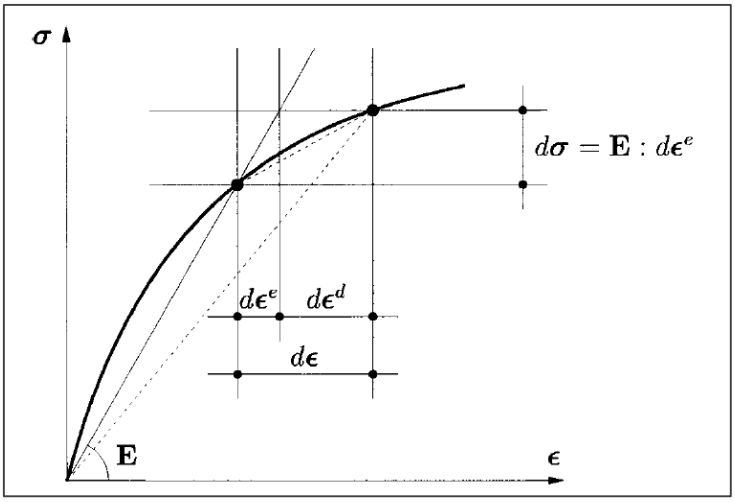

Figure 2.2: Definition of the elastic-degrading strain rate
(Carol et al., 2001)

Differentiation of Eq. 2.18 leads to the consistency condition for the elastic-degrading model presented in Eq. 2.21a, with a similar meaning of that of elastoplasticity. n_{ij}^{d} defined in Eq. 2.21b represents the derivatives of the loading function for constant values of the plastic multiplier and history variables, with the geometric meaning of the direction normal to the current loading surface in the stress space. As for the elastoplastic formulation, associativity could be imposed to the elastic-degrading formulation by considering that m_{ij}^{p} and n_{ij}^{p} are collinear.

$$dF^{d} = n_{ij}^{d}\, d\sigma_{ij} + \frac{\partial F^{d}}{\partial \chi_{k}^{d}}\, d\chi_{k}^{d} = 0 \qquad and \qquad n_{ij}^{d} = \frac{\partial F^{d}}{\partial \sigma_{ij}} \qquad (Eq.\,2.21\ a,b)$$

The history variables $\boldsymbol{\chi^{d}}$ could be expressed similarly to its counterpart in the elastoplasticity formulation as functions of the degrading multiplier. Regarding this assumption, equivalent definition of the *history variable rate* $d\chi_{k}^{d}$ and the *hardening/softening law* h_{k}^{d} can be written as expressed in Eq. 2.22a and Eq. 2.22b. h_{k}^{d} define again the way the history variables change when a degrading loading occurs.

$$d\chi_{k}^{d} = h_{k}^{d}\, d\lambda^{d} \qquad and \qquad h_{k}^{d} = \frac{\partial \chi_{k}^{d}}{\partial \lambda^{d}} \qquad (Eq.\,2.22\ a,b)$$

Rewriting Eq. 2.21a we obtain Eq. 2.23. H^{d} in Eq. 2.24 is the *hardening/softening modulus* in the elastic-degrading formulation and has similar meaning to its counterpart in the elastoplasticity formulation (i.e. the way the loading function change when a degrading loading occurs).

$$dF^d = n_{ij}^d \, d\sigma_{ij} - H^d \, d\lambda^d = 0 \qquad (Eq.\,2.23)$$

$$H^d = -\frac{\partial F^d}{\partial \lambda^d} = -\frac{\partial F^d}{\partial \chi_k^d}\frac{\partial \chi_k^d}{\partial \lambda^d} = -\frac{\partial F^d}{\partial \chi_k^d}\, h_k^d \qquad (Eq.\,2.24)$$

The loading-unloading criterion can be given as restrictions in the same manner that for elastoplasticity. These restrictions are indicated in the three conditions of Eq. 2.25 and lead to two possible situations indicated in Eq. 2.26. Like in elastoplasticity, the loading criterion takes place when the degrading multiplier increases ($d\lambda^d > 0$) and therefore the loading function must be $F^d = 0$. On the other hand, the unloading criterion takes place when the loading function is negative (i.e. elastic domain) and therefore the degrading multiplier must be null.

$$\begin{cases} F^d d\lambda^d = 0 \\ F^d \leq 0 \\ d\lambda^d \geq 0 \end{cases} \qquad (Eq.\,2.25)$$

$$\begin{cases} loading \quad \rightarrow F^d = 0 \quad if \quad d\lambda^d \geq 0 \\ unloading \quad \rightarrow d\lambda^d = 0 \quad if \quad F^d \leq 0 \end{cases} \qquad (Eq.\,2.26)$$

All these equations looks practically identical to its counterpart in classical plasticity, except that the secant stiffness is used instead of the initial stiffness. These equations can be thus combined in the same way as the ones in elastoplasticity to obtain the expression of the degrading multiplier (Eq. 2.27). Similarly to plasticity, these expressions and the followings are subjected to the constraint $H^d \geq H_{cr}^d$, where H_{cr}^d is defined in Eq. 2.28.

$$d\lambda^d = \frac{n_{ij}^d \; D_{ijkl} \; d\varepsilon_{kl}}{H^d - H_{cr}^d} \qquad (Eq.\,2.27)$$

$$H_{cr}^d = -n_{ij}^d \; D_{ijkl} \, m_{kl}^d \qquad (Eq.\,2.28)$$

By introducing Eq. 2.27 into Eq. 2.20 and Eq. 2.19 one obtains the Eq. 2.29 where the elastoplastic tangential stiffness tensor for degrading loading can be identified and written as Eq. 2.30.

$$d\sigma_{ij} = \left[D_{ijkl} - \frac{D_{ijmn} \, m_{mn}^d \;\; n_{pq}^d \, D_{pqkl}}{H^d - H_{cr}^d} \right] d\varepsilon_{kl} \qquad (Eq.\,2.29)$$

$$D_{ijkl}{}^{tan} = D_{ijkl} - \frac{D_{ijmn} \, m_{mn}^d \;\; n_{pq}^d \, D_{pqkl}}{H^d - H_{cr}^d} \qquad (Eq.\,2.30)$$

2.3.- Degradation rule and introduction of damage variables

As was noted by *Carol et al. (1994)*, in spite of the similarity with the elastoplasticity formulation, the expressions presented before show an important qualitative difference with their plastic counterparts. The fact that the secant stiffness is involved means that the functions and parameters usually defined for plasticity are not sufficient to define the evolution of the degrading models, because no evolution law for the secant stiffness (or compliance) itself has been specified yet.

In order to do that, Eq. 2.14a is differentiated and compared to Eq. 2.19. This leads to the relationship between the degrading strain rate and the rate of change of stiffness denoted in Eq. 2.31. Using the property obtained in Eq. 2.16 one obtains a more convenient expression in Eq. 2.32. This expression indicates a relationship between the increment of secant compliance and the increment of the degrading strain. When the first is known, the second follows.

$$D_{ijkl}\, d\varepsilon_{kl}^{d} = -\, dD_{ijkl}\, \varepsilon_{kl} \qquad (Eq.\,2.31)$$

$$d\varepsilon_{kl}^{d} = dC_{ijkl}\, \sigma_{ij} \qquad (Eq.\,2.32)$$

The corresponding evolution law of the secant compliance must involve the same independent components of the compliance (or stiffness) tensor itself. (i.e. 21). As suggested by *Carol et al. (1994)* and *Carol et al. (2001)*, is reasonable to suppose that there exists a reduced set of variables which characterize the state of degradation achieved in the material at any state of the loading process. These are the *damage variables* represented by $\mathfrak{D}_*$. The nature of $\mathfrak{D}_*$ (scalar, vectorial or tensorial) does not need to be specified for a general theory development (the subscript * represents the desired number of indices).

In stress-based formulations of elastic-degrading material reported by the authors cited in *Carol et al. (1994)*, the degradation process is modeled by means of some rules which describe the progressive "increase" of the secant compliance tensor $\boldsymbol{C}$ (i.e. decrease of the secant stiffness tensor $\boldsymbol{D}$). According to this, one may write Eq. 2.33 and Eq. 2.34.

$$C_{ijkl} = f\left(C_{ijkl}^{\,0}, \mathfrak{D}_*\right) \qquad (Eq.\,2.33)$$

$$dC_{ijkl} = \frac{\partial C_{ijkl}}{\partial \mathfrak{D}_*}\, d\mathfrak{D}_* \qquad (Eq.\,2.34)$$

$C_{ijkl}^{\,0}$ are the known components of the initial compliance tensor. The repetition of subscript * implies summation over all indices represented by this symbol. A general *damage rule* for $\mathfrak{D}_*$ can now be written as proposed by *Carol et al. (1994)* in Eq. 2.35a where similar to the flow rule for degrading strains, $d\lambda^d$ is the *damage multiplier* defining the magnitude and $\mathcal{M}_*$ defines the direction of the change of the damage variables in the damage space.

$$d\mathfrak{D}_* = \mathcal{M}_* \, d\lambda^d \qquad with \qquad \mathcal{M}_* = \frac{\partial \mathfrak{D}_*}{\partial \lambda^d} \qquad (Eq.\,2.35\ a,b)$$

By substitution of Eq. 2.35 in Eq. 2.34 one obtains Eq. 2.36. Then by substitution of the latter in Eq. 2.32, one obtains Eq. 2.37 that allows setting the relationship between the flow rule of degrading strain m_{kl}^d and the damage rule $\mathcal{M}_*$, (Eq. 2.38). Note that, according these expressions, the flow rule for the degrading strains is fully defined when the law for the evolution of the secant compliance with the damage variables (i.e. $\partial C_{ijkl}/\partial \mathfrak{D}_*$) and the damage rule $\mathcal{M}_*$ are established.

$$dC_{ijkl} = \frac{\partial C_{ijkl}}{\partial \mathfrak{D}_*} \, \mathcal{M}_* \, d\lambda^d \qquad (Eq.\,2.36)$$

$$d\varepsilon_{kl}^d = \frac{\partial C_{ijkl}}{\partial \mathfrak{D}_*} \, \mathcal{M}_* \ \ \sigma_{ij} \, d\lambda^d \qquad (Eq.\,2.37)$$

$$m_{kl}^d = \frac{\partial C_{ijkl}}{\partial \mathfrak{D}_*} \, \mathcal{M}_* \, \sigma_{ij} \qquad (Eq.\,2.38)$$

2.4.- Thermodynamic considerations

As was exposed in *Carol et al. 1994*, further insight into the formulation of elastic-degrading material requires the introduction of some thermodynamic concepts. For the elastic-degrading material, the mechanical free energy of the system is given by the elastic energy corresponding to the current secant stiffness (or compliance) and can be expressed as Eq. 2.39a or Eq. 2.39b.

$$u = \frac{1}{2}\varepsilon_{ij} D_{ijkl} \varepsilon_{kl} \quad or \quad u = \frac{1}{2}\sigma_{ij} C_{ijkl} \sigma_{kl} \qquad (Eq.\,2.39\ a,b)$$

Differentiation of Eq. 2.39a leads to Eq. 2.40 and Eq. 2.41. The first term on the right-hand side of Eq. 2.41 has the meaning of the external work supplied to the system (with constant stiffness), while the second correspond to the dissipation energy due to the stiffness degradation (i.e. with no external work supply). The second term is called *rate of degrading dissipation* $d\mathcal{d}$ defined in Eq. 2.42.

$$du = \frac{\partial u}{\partial \varepsilon_{kl}} d\varepsilon_{kl} + \frac{\partial u}{\partial D_{ijkl}} dD_{ijkl} \qquad (Eq.\,2.40)$$

$$du = \sigma_{kl} \, d\varepsilon_{kl} + \frac{1}{2} \ \varepsilon_{ij} dD_{ijkl} \varepsilon_{kl} \qquad (Eq.\,2.41)$$

$$d\mathcal{d} = -\frac{1}{2} \ \varepsilon_{ij} dD_{ijkl} \varepsilon_{kl} \quad or \quad d\mathcal{d} = \frac{1}{2}\sigma_{ij} dC_{ijkl} \sigma_{kl} \qquad (Eq.\,2.42\ a,b)$$

The *thermodynamic or conjugated force* $-\mathcal{Y}_*$, which is conjugated to the damage variable $\mathfrak{D}_*$, is defined as the quantity that yields the rate of degrading dissipation when multiplied by the rate $d\mathfrak{D}_*$ (Eq. 2.43). This force must have the same character and dimensions than $\mathfrak{D}_*$. By substitution of Eq. 2.34 in Eq. 2.42b one obtains Eq. 2.44 that allows one to define the conjugated force as Eq. 2.45. Note that the previous definition is equivalent to define the gradient of the mechanical free energy, as in Eq. 2.46.

$$dd = (-\mathcal{Y}_*)\, d\mathfrak{D}_* \qquad (Eq.\,2.43)$$

$$dd = \frac{1}{2}\sigma_{ij}\sigma_{kl}\ \frac{\partial C_{ijkl}}{\partial \mathfrak{D}_*}\ d\mathfrak{D}_* \qquad (Eq.\,2.44)$$

$$(-\mathcal{Y}_*) = \frac{1}{2}\sigma_{ij}\sigma_{kl}\frac{\partial C_{ijkl}}{\partial \mathfrak{D}_*} \qquad (Eq.\,2.45)$$

$$(-\mathcal{Y}_*) = \frac{\partial u}{\partial \mathfrak{D}_*} \qquad (Eq.\,2.46)$$

With the definition of $-\mathcal{Y}_*$ it is posible to define the gradient of the loading function in the damage space $\mathcal{N}_*$ and relate it to the gradient in the stress space as indicated in Eq. 2.47 and Eq. 2.48. Note that $\mathcal{N}_*$ is only defined when F^d is expressed as a function of the thermodynamic force $-\mathcal{Y}_*$. Associativity in the damage space occurs when $\mathcal{M}_*$ is porportional to $\mathcal{N}_*$ and it also implies associativity at stress level (*Carol et al., 1994 and Carol et al., 2001*).

$$\mathcal{N}_* = \frac{\partial F^d}{\partial(-\mathcal{Y}_*)} \qquad (Eq.\,2.47)$$

$$n_{ij}^d = \frac{\partial F^d}{\partial \sigma_{ij}}\ = \frac{\partial F^d}{\partial(-\mathcal{Y}_*)}\frac{\partial(-\mathcal{Y}_*)}{\partial \sigma_{ij}} = \mathcal{N}_*\ \frac{\partial C_{ijkl}}{\partial \mathfrak{D}_*}\ \sigma_{kl} \qquad (Eq.\,2.48)$$

2.5.- Isotropic scalar damage models

With the theoretical framework described previously, and taking into account the thermodynamic considerations presented before, it is possible to formulate a variety of elastic-degrading or damage models. The simplest ones are those in which the initial stiffness is isotropic, and its degraded counterpart also maintains isotropy. The traditional *"(1-D)" scalar damage model*, is one of these, in which all the components of the stiffness tensor are reduced with the same coefficient $(1-\mathfrak{D})$. $\mathfrak{D}$ is the damage variable varying from 0 to 1 and is related to the ratio of micro-cracks area over the whole area. In *Carol et al. (1994)*, a strain-based formulation of this type was derived.

In the *"(1-D)"* scalar damage models type, the well-known expressions in Eq. 2.49 are assumed for the secant stiffness and compliance. Note that the damage variables are reduced to one scalar variable. In Eq. 2.50 the differentiation of Eq. 2.49b is presented. With these definitions, it is possible to use $d\mathfrak{D}$ itself as inelastic multiplier, as indicated

in Eq. 2.51. In addition, the definition of the damage rule is derived in Eq. 2.52. According to Eq. 2.38 and 2.45, one can define the flow rule of degrading strain and the conjugated force as indicated in Eq. 2.53 and Eq. 2.54.

$$D_{ijkl} = (1 - \mathfrak{D})\, D^{0}_{ijkl} \quad and \quad C_{ijkl} = \frac{1}{1-\mathfrak{D}}\, C^{0}_{ijkl} \qquad (Eq.\,2.49\ a,b)$$

$$\frac{\partial C_{ijkl}}{\partial \mathfrak{D}_*} = \frac{1}{(1-\mathfrak{D})^2}\, C^{0}_{ijkl} = \frac{1}{1-\mathfrak{D}}\, C_{ijkl} \qquad (Eq.\,2.50)$$

$$d\mathfrak{D} = d\lambda^{d} \qquad (Eq.\,2.51)$$

$$\mathfrak{D}_* = scalar = \mathfrak{D} \quad and \quad \mathcal{M}_* = scalar = \mathcal{M} = \frac{\partial \mathfrak{D}}{\partial \lambda^{d}} = 1 \qquad (Eq.\,2.52)$$

$$m^{d}_{kl} = \frac{1}{1-\mathfrak{D}}\, \varepsilon_{kl} \qquad (Eq.\,2.53)$$

$$(-\mathcal{Y}_*) = scalar = -\mathcal{Y} = \frac{u}{1-\mathfrak{D}} \qquad (Eq.\,2.54)$$

A simpler expression were presented by *Carol et al. (2001)* by introducing the concept of *logarithmic scalar damage variable*. While the conventional damage variable $\mathfrak{D}$ varies between 0 and 1, the logarithmic damage variable, L, varies between 0 and ∞. Again, it is possible to use dL itself as damage multiplier. Similar definition than Eq. 2.51 and Eq. 2.52 are made in the Eq. 2.55 and Eq. 2.56. These assumptions allows one to rewrite Eq. 2.49, Eq. 2.50, Eq. 2.53, and Eq. 2.54 as following Eq. 2.57, Eq. 2.58, Eq. 2.59 and Eq. 2.60. Note that the expression of m^{d}_{kl} and $-\mathcal{Y}$ are not directly dependent on the damage variable anymore.

$$dL = d\lambda^{d} \qquad (Eq.\,2.55)$$

$$\mathfrak{D}_* = scalar = L = \ln\left(\frac{1}{1-\mathfrak{D}}\right) \quad and \quad \mathcal{M}_* = scalar = \mathcal{M} = \frac{\partial L}{\partial \lambda^{d}} = 1 \qquad (Eq.\,2.56)$$

$$D_{ijkl} = e^{-L}\, D^{0}_{ijkl} \quad and \quad C_{ijkl} = e^{L}\, C^{0}_{ijkl} \qquad (Eq.\,2.57\ a,b)$$

$$\frac{\partial C_{ijkl}}{\partial \mathfrak{D}_*} = e^{L}\, C^{0}_{ijkl} = C_{ijkl} \qquad (Eq.\,2.58)$$

$$m^{d}_{kl} = \varepsilon_{kl} \qquad (Eq.\,2.59)$$

$$-\mathcal{Y} = u \qquad (Eq.\,2.60)$$

As was done by *Carol et al. (2001),* in order to achieve an associated formulation in the damage space (and therefore in the stress space) the loading function is written in terms of the conjugate force $-\mathcal{Y}$ and the damage state L (equivalent to λ^{d}). The format considered is detailed in the Eq. 2.61. r is the unique history variable (scalar) determining

the current configuration of the loading surface and its evolution with damage. Its meaning is discussed later. According to Eq. 2.47 and Eq. 2.48 one can obtain Eq. 2.62 and Eq. 2.63. Note that the gradients $\mathcal{N}$ and n_{ij}^{d} are equal to the corresponding rules $\mathcal{M}$ and m_{kl}^{d}, which means associativity at stress and damage levels.

$$F^{d} = u - r \qquad (Eq.\,2.61)$$

$$\mathcal{N}_{*} = \mathcal{N} = \frac{\partial F^{d}}{\partial(-\mathcal{Y})} = \frac{\partial F^{d}}{\partial u} = 1 \qquad (Eq.\,2.62)$$

$$n_{ij}^{d} = \frac{\partial F^{d}}{\partial \sigma_{ij}} = \frac{\partial F^{d}}{\partial(-\mathcal{Y})}\frac{\partial(-\mathcal{Y})}{\partial \sigma_{ij}} = \varepsilon_{ij} \qquad (Eq.\,2.63)$$

The equivalent hardening/softening modulus of the elastoplastic formulation is named now *damage evolution modulus* H^{d}. It can be obtained from the definition of F^{d} and written as Eq. 2.64 (the derivative developed in Eq. 2.66 was useful). Also the equivalent hardening/softening law h^{d} is presented in Eq. 2.65. Its definition is subjected to the definition of r.

$$H^{d} = -\frac{\partial F^{d}}{\partial \lambda^{d}} = -\left(\frac{\partial u}{\partial \lambda^{d}} - \frac{\partial r}{\partial \lambda^{d}}\right) = h^{d} - u \qquad (Eq.\,2.64)$$

$$h^{d} = \frac{\partial \chi_{k}^{d}}{\partial \lambda^{d}} = \frac{\partial r}{\partial \lambda^{d}} \qquad (Eq.\,2.65)$$

$$\frac{\partial u}{\partial \lambda^{d}} = \frac{\partial\left(\frac{1}{2}\varepsilon_{ij}D_{ijkl}\varepsilon_{kl}\right)}{\partial \lambda^{d}} = \frac{1}{2}\varepsilon_{ij}\varepsilon_{kl}D_{ijkl}^{0}\frac{\partial\left(e^{-\lambda^{d}}\right)}{\partial \lambda^{d}} = -\frac{1}{2}\varepsilon_{ij}D_{ijkl}\varepsilon_{kl} = -u \qquad (Eq.\,2.66)$$

Finally, the expression for the degrading (or damage) multiplier λ^{d} and the tangent stiffness for this particular damage model is obtained as indicated in Eq. 2.67 to Eq. 2.69. Eq. 2.69 can be written also as Eq. 2.70 and considering that, when degrading process is activated and $F^{d} = 0$, we have $u = r$, we can also write Eq. 2.71.

$$d\lambda^{d} = \frac{\varepsilon_{ij}\ D_{ijkl}\ d\varepsilon_{kl}}{H^{d} - H_{cr}^{d}} = \frac{\sigma_{kl}}{h^{d} + u}d\varepsilon_{kl} \qquad (Eq.\,2.67)$$

$$H_{cr}^{d} = -\varepsilon_{ij}\ D_{ijkl}\,\varepsilon_{kl} = -2u \qquad (Eq.\,2.68)$$

$$D_{ijkl}{}^{tan} = D_{ijkl} - \frac{\sigma_{ij}\ \sigma_{kl}}{h^{d} + u} = e^{-\lambda^{d}}\,D_{ijkl}^{0} - \frac{\sigma_{ij}\ \sigma_{kl}}{h^{d} + u} \qquad (Eq.\,2.69)$$

$$D_{ijkl}{}^{tan} = D_{ijkl} - \frac{D_{ijkl}\,\varepsilon_{kl}\ \sigma_{kl}}{h^{d} + u} = D_{ijkl}\left(1 - \frac{2u}{h^{d} + u}\right) \qquad (Eq.\,2.70)$$

$$D_{ijkl}{}^{tan} = D_{ijkl}\left(1 - \frac{2r}{h^{d} + r}\right) \qquad (Eq.\,2.71)$$

2.6.- Damage evolution law and damage evolution rate

The model requires defining only one history variable (r). This variable indicates the current configuration of the loading surface and defines its evolution when a degrading (or damaging) state is in process. According to the definition of F^d (Eq. 2.61), r must be defined with the same units as the mechanical free energy u and must be related with the damage multiplier λ^d.

The physical meaning could be understood as the value of mechanical free energy from which the damaging process is activated. If the mechanical energy accumulated in the material is lower than the current value of r, no degrading occurs, λ^d does not increase, and elastic behaviour will be observed. When the mechanical energy accumulated reaches the current value of r, λ^d increases, degrading strain occurs and non-elastic behaviour will be observed. In other words, r is in some way the loading surface expressed in terms of the mechanical free energy u. For these reason r is usually named *damage locus*.

The evolution of r with damage (i.e. with λ^d) defines how the loading surface (or damage locus) change when a degrading process takes place. If r is defined in such way that it increases with increasing λ^d, a hardening process in terms of mechanical energy will occur with an expanding loading surface. This means that a damaged material is able to receive more energy by increasing its damage. Conversely, if r is defined in such way that it decreases with increasing λ^d, a softening process in terms of mechanical energy will occur, and damaged material reduces its capacity to accumulate energy. For these reason the expression defining r as a function of λ^d is named the *damage evolution law*.

In geomaterials, hardening processes are likely to take place. For these reason, only expression that define increasing r with damage are considered. In the present work two expression are proposed and implemented as damage evolution laws. One is the exponential dependency indicated in Eq. 2.72a (introduced in previous works, e.g. Gens et al. 2007 and Pinyol et al. 2007) and the other one is the linear dependency presented in Eq. 2.73a. For both cases, the corresponding expression for h^d are derived in Eq. 2.72b and Eq. 2.73b.

$$r = r_0\, e^{r_1\, \lambda^d} \qquad h^d = \frac{\partial r}{\partial \lambda^d} = r_1\, r \qquad (Eq.\, 2.72\ a, b)$$

$$r = r_0 + r_1\, \lambda^d \qquad h^d = \frac{\partial r}{\partial \lambda^d} = r_1 \qquad (Eq.\, 2.73\ a, b)$$

r_0 is the initial value of the damage locus in the undamaged state and represent the energy threshold from which degrading process is activated. r_0 equal or close to zero means that the degrading process starts very early when the material starts to accumulate energy (note that zero is not possible for the exponential dependency). r_1 is defined as the *damage evolution rate* and it gives the rate of evolution of r with damage multiplier (note that higher values of r_1 gives lower damage rate, since the damage locus

increases faster). Since r must always increase, r_1 is restricted to zero and positive values. r_1 equal to zero means that the size of damage locus is constant and equal to the initial value r_o.

Is important to note that hardening in terms of mechanical energy cannot be directly related to a hardening behaviour in terms of stress-strain response. In other words, an expanding mechanical energy loading surface does not mean an expanding loading surface in the stress space. This can be understood rewriting the definition of the damage evolution modulus H^d as shown in Eq. 2.74 and Eq. 2.75 for exponential and linear damage evolution laws (from Eq. 2.64 substituting h^d defined in Eq. 2.72b and Eq. 2.73b and considering $u = r$).

$$H^d = h^d - u = r_1\, r - r = r(r_1 - 1) \qquad (Eq.\,2.74)$$

$$H^d = h^d - u = r_1\ - r \qquad (Eq.\,2.75)$$

For the exponential dependency, H^d is zero for $r_1 = 1$, positive for values of $r_1 > 1$ and negative for values of $r_1 < 1$. This means that for $r_1 = 1$ the behaviour of the elastic-degrading material is like perfect plasticity in elastoplastic formulation, and that for values of $r_1 > 1$ and $r_1 < 1$ a hardening or softening behaviour will be observed respectively. For the linear damage evolution law, H^d is zero for $r_1 = r$, and therefore, positive for values of $r_1 > r$ and negative for values of $r_1 < r$. Since r is not a fixed value is not possible to known beforehand the resulting stress-strain behaviour.

It is also interesting to derive a more detailed expression of tangent stiffness, substituting Eq. 2.72b or 2.73b in Eq. 2.71 obtaining Eq. 2.76 and Eq. 2.77 for exponential and linear damage evolution laws respectively. Note again that, in the case of exponential dependency, for a value of $r_1 = 1$ the tangent stiffness matrix is null (i.e. “perfect plasticity” behaviour) and for values of $r_1 > 1$ and $r_1 < 1$, it is positive and negative definite (i.e. hardening and softening behavior, respectively). Again, not conclusions can be made for the case of linear dependency.

$$D_{ijkl}{}^{tan} = D_{ijkl}\left(1 - \frac{2}{1 + r_1}\right) \qquad (Eq.\,2.76)$$

$$D_{ijkl}{}^{tan} = D_{ijkl}\left(1 - \frac{2r}{r_1 + r}\right) \qquad (Eq.\,2.77)$$

2.7.- Loading surface in the p- q space

The loading surface in the mean volumetric stress - shear stress plane (p-q space) is conveniently defined to illustrate the features of the model in a synthetic and graphic way. The definition of the free mechanical energy in terms of p and q for an elastic-degrading material is presented in Eq. 2.78, where ε_v is the volumetric strain and ε_q is the equivalent shear strain. ε_v and ε_q are related to p and q through Eq. 2.79a and 2.80a respectively. K and G are the current bulk and shear modulus that defines the current secant stiffness of the damaged material. Its relation with the undamaged parameters K_o and G_o is presented in Eq. 2.79b and 2.80b respectively.

$$u = \frac{1}{2}\left(p\ \varepsilon_v + q\ \varepsilon_q\right) \qquad (Eq.\ 2.78)$$

$$\varepsilon_v = \frac{p}{K} \qquad with \qquad K = K_o\ e^{-\lambda^d} \qquad (Eq.\ 2.79\ a,b)$$

$$\varepsilon_q = \frac{q}{3G} \qquad with \qquad G = G_o\ e^{-\lambda^d} \qquad (Eq.\ 2.80\ a,b)$$

Substituting Eq. 2.79a and 2.80a into Eq. 2.78 leads to Eq. 2.81 ($u = r$ was considered). The expression is an ellipse that represents the loading surface in the p-q space for the case of an isotropic damage model. The radius are equal to $\sqrt{2Kr}$ and $\sqrt{6Gr}$ for the p-axis direction and q-axis direction respectively as showed in Fig. 2.3. The expansion or contraction of the loading surface depends on the variation of K, G, and r. Since the elastic parameters K and G degrade with the same rate as indicated in Eq. 2.79b and Eq. 2.80b, it is possible to conclude that the loading surface expands or contracts without changing its shape (i.e. the relation between horizontal and vertical radius is always the same).

$$\frac{p^2}{2Kr} + \frac{q^2}{6Gr} = 1 \qquad (Eq.\ 2.81)$$

$$\frac{p^2}{2K_o r_0\ e^{\lambda^d\,(r_1-1)}} + \frac{q^2}{6G_o r_0\ e^{\lambda^d\,(r_1-1)}} = 1 \qquad (Eq.\ 2.82)$$

Taking into account the exponential damage evolution law (Eq. 2.72a) and the definitions presented in Eq. 2.79b and 2.80b, one can write Eq. 2.82. In agreement with what was explained previously, an expansive loading surface would result for $r_1 > 1$, a contractive loading surface for $r_1 < 1$ and an unchangeable loading surface with $r_1 = 1$, related to a hardening, softening and “neutral” behaviour in the stress-strain response.

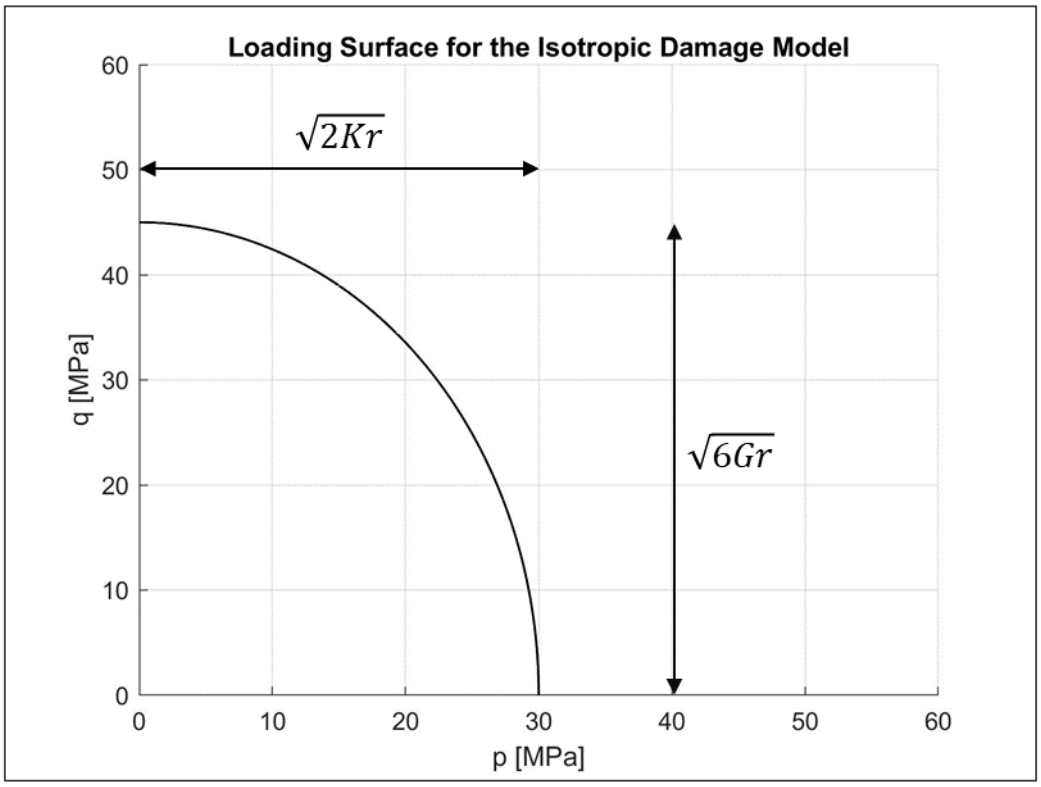

Figure 2.3: Loading surface for the isotropic damage model in the p-q plane

2.8.- Model features through simulated tests

At this point is convenient to summarize the parameters that must be defined to fully describe this isotropic damage model:

- D_{ijkl}^{0}: the components of the initial (undamaged) secant stiffness tensor. For isotropic elasticity it is fully defined with the initial modulus of elasticity E^0 and the Poisson's ratio ν (considered constant) as indicated in Eq. 2.83.
- r_0: the initial damage locus that represents the energy threshold to exceed to start the degrading process. The units are the same as for energy.
- r_1: the damage evolution rate that gives the rate of evolution of the loading surface with damage multiplier. It is dimensionless for exponential damage evolution law and has the same unit as for energy in the case of linear damage evolution law.
- In addition, it is necessary to define which of the damage evolution laws is considered: for this work, exponential or linear dependency.

$$\boldsymbol{D^0} = \frac{E^0}{(1+\nu)(1-2\nu)} \begin{bmatrix} 1-\nu & \nu & \nu & & & \\ \nu & 1-\nu & \nu & & & \\ \nu & \nu & 1-\nu & & & \\ & & & \frac{1-2\nu}{2} & & \\ & & & & \frac{1-2\nu}{2} & \\ & & & & & \frac{1-2\nu}{2} \end{bmatrix} \quad (Eq.\,2.83)$$

In order to illustrate the damage model capabilities in a parametric study, a few unconfined compression tests have been simulated. The parameters of the materials chosen are presented in Tab. 2.1. In the tests grouped under the title "*Group 1 Tests"*, r_0 is variable while r_1 is fixed. On the other hand, in tests grouped under the title "*Group 2 Tests"*, r_0 is fixed while r_1 is variable. The elastic behaviour determined by E^0 and ν are the same for all tests. Both linear and exponential damage evolution laws were implemented.

Parameter	Group 1 Tests	Group 2 Tests
$E^0\ [MPa]$	4000	4000
$\nu\ [-]$	0.20	0.20
$r_0\ [MPa]$	Analyzed	0.2
$r_1\ [-\ or\ MPa]$	0.2	Analyzed

Table 2.1: Parameters for the triaxial tests simulated

The results for the case of exponential damage evolution law, are plotted in Fig. 2.4 and Fig 2.5 for Group 1 tests, and Group 2 tests respectively. In the same way, the results for the case of linear damage evolution law are plotted in Fig. 2.6 and Fig 2.7 for Group 1 Tests, and Group 2 Tests respectively.

It can be observed that the slope of the first part of the stress-strain curve is the same for all the simulated tests since it is defined by the initial elastic behaviour (i.e. E^0 and ν). In Fig. 2.4 and Fig. 2.6, one can see how the initiation of damage (or degrading) is controlled by the initial size of the damage locus r_0. In Fig. 2.5 and Fig. 2.7, it is clearly observed the influence of the damage evolution rate on the stress-strain response once reached the maximum deviatoric stress. In general, in both exponential and linear dependencies, the lower r_1 is, the more brittle is the behaviour after peak. Linear damage evolution law results in softer responses after peak, while the exponential gives more sharply behaviour. Finally, from Fig. 2.5, one can see also how r_1 define the behaviour for the exponential dependency as discussed before ("neutral" for $r_1 = 1$, and hardening or softening behaviour for values of $r_1 > 1$ and $r_1 < 1$ respectively).

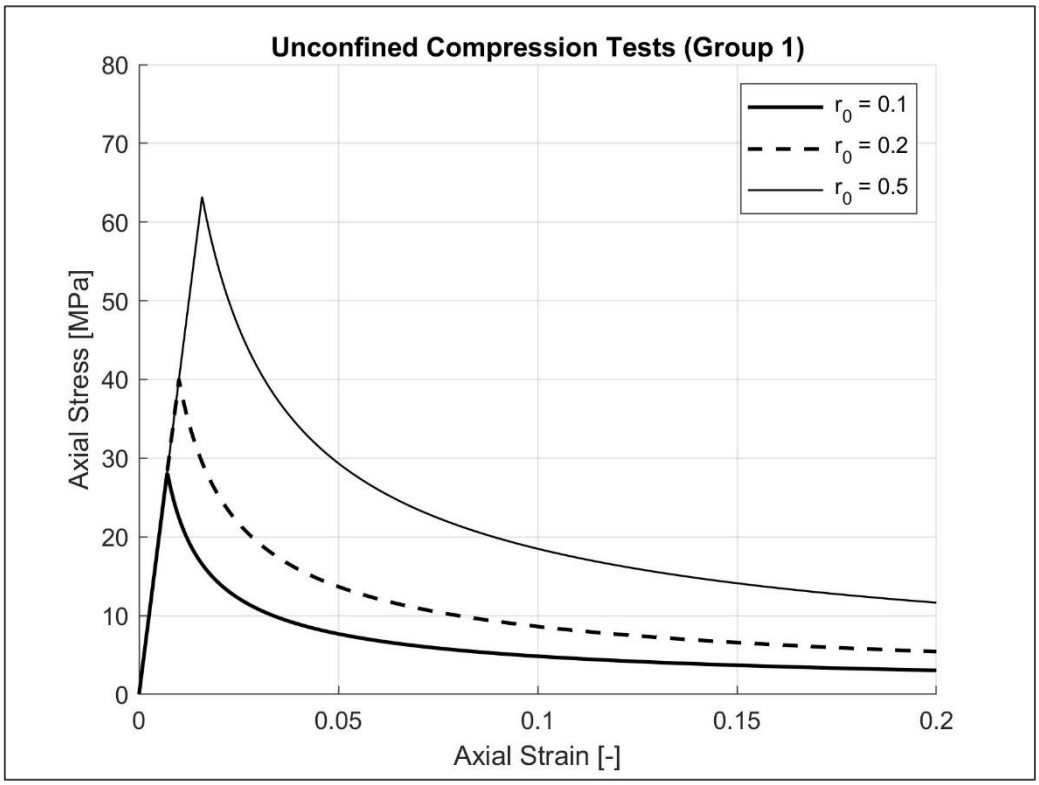

Figure 2.4: Unconfined compression tests of Group 1 - Exponential damage evolution law

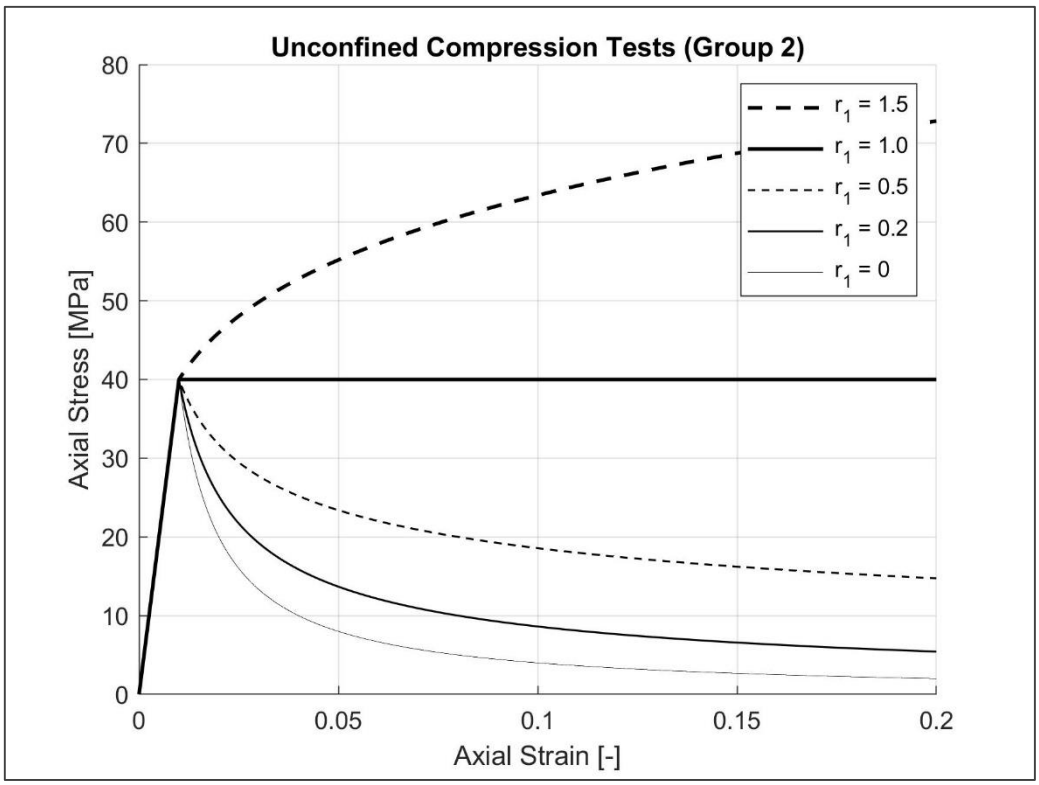

Figure 2.5: Unconfined compression of tests Group 2 - Exponential damage evolution law

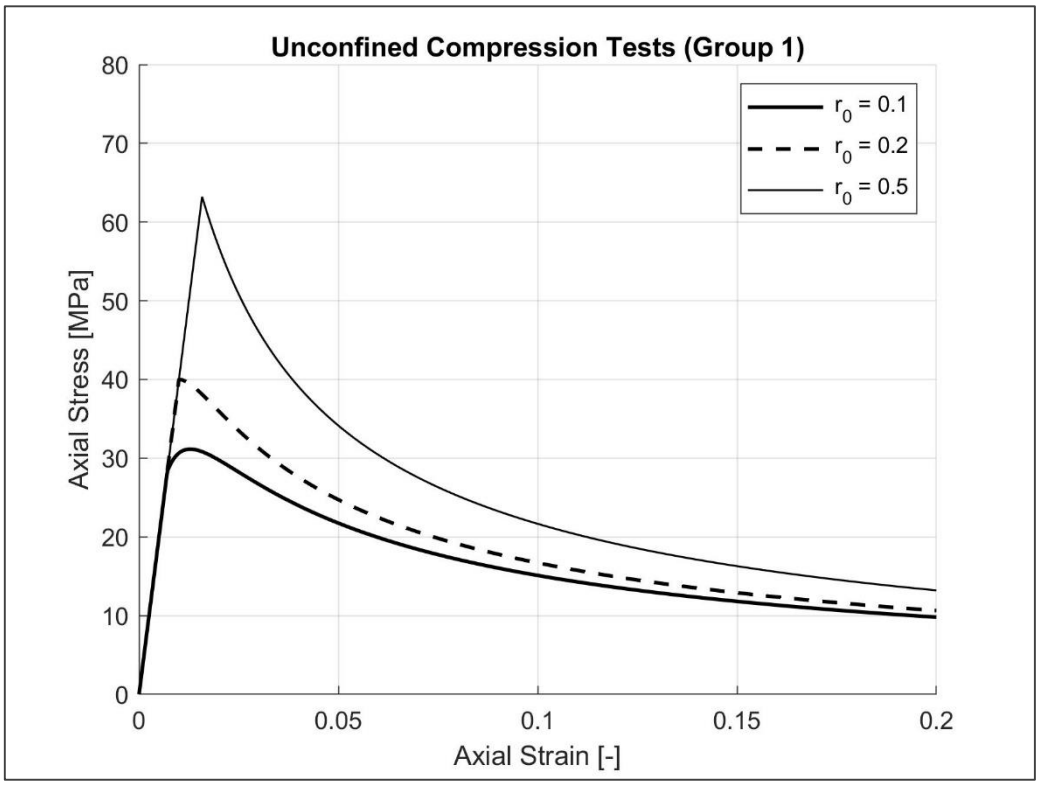

Figure 2.6: Unconfined compression tests of Group 1 - Linear damage evolution law

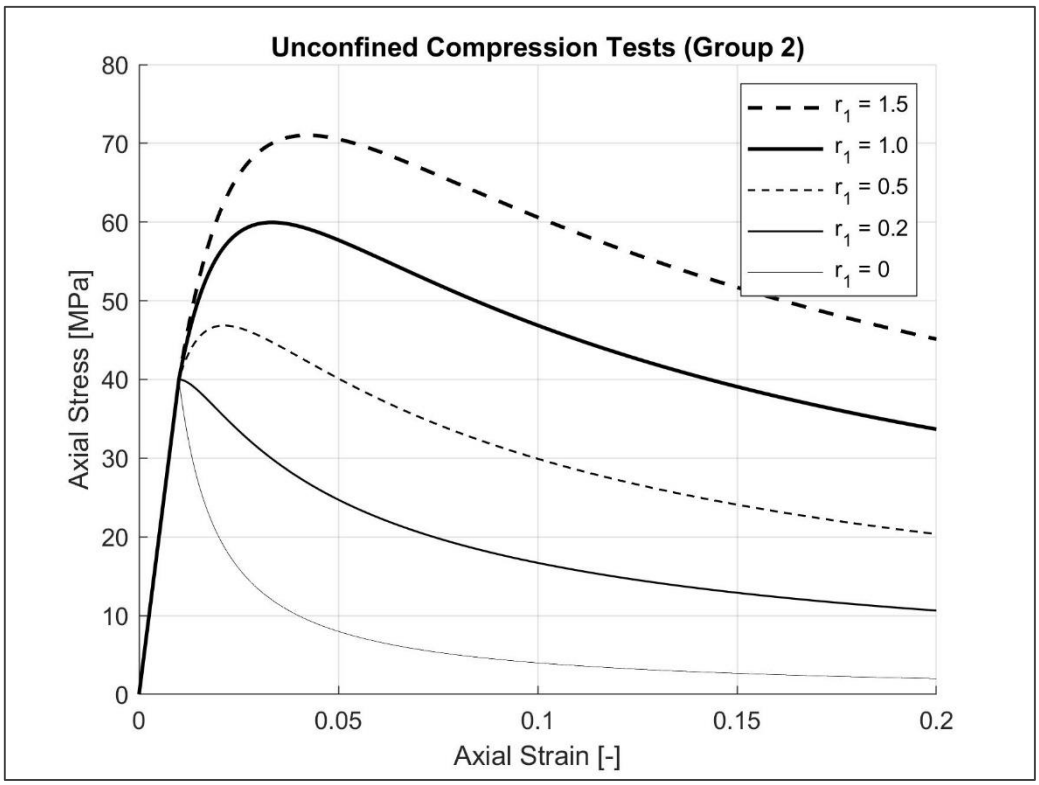

Figure 2.7: Unconfined compression tests of Group 2 - Linear damage evolution law

In the case of unconfined compression tests, the expression to determine the mechanical free energy u can be simplified as indicated in Eq. 2.84, where σ_a and ε_a are the axial components of the stress and strain tensor. With this simplification, and remembering that $u = r$ when the degrading process is activated, one can derive the expression of Eq. 2.85a.

$$u = \frac{1}{2}\sigma_{ij}\varepsilon_{ij} = \frac{1}{2}\sigma_a\varepsilon_a \qquad (Eq.\,2.84)$$

$$\sigma_a = \frac{2u}{\varepsilon_a} = \frac{2r}{\varepsilon_a} \qquad and \qquad \sigma_a = \frac{2r_0}{\varepsilon_a} \;\; (for\; r_1 = 0) \qquad (Eq.\,2.85\;a, b)$$

Expression of Eq. 2.85a represents a hyperbola easy to plot in the axial stress-axial strain plane. Actually, the hyperbola can be idealized as the loading surface in terms of energy itself, which "change" position (rather it increases) when r increases. If we assume $r_1 = 0$ (i.e. r constant and equal to the initial value r_0) the loading function (expressed in terms of energy) does not increase, and can be plotted directly in the axial stress-axial strain plane. This hyperbola demarcates the boundaries of the "*possible states area*" in terms of amount of energy accumulated.

This is shown in Fig. 2.8 where, on the right hand side, the hyperbola considering $r_0 = 0.2\;MPa$ is plotted beside the simulated triaxial test with $r_0 = 0.2\;MPa$ and $r_1 = 0$ (note that the damage evolution law has no influence: if r_1 is equal to zero, the response obtained will be the same). Evolution of the damage multiplier λ^d is plotted in the same figure to follow the evolution of damage.

On the left hand side of the Fig. 2.8 are plotted the stress path in the p-q plane, and the initial configuration of the loading surface (i.e. in terms of initial undamaged values of elastic parameters). When the surface is reached, the elastic parameters start to degrade, and the loading surface starts to contract (indicated by the blue arrows in Fig. 2.8). The stress path after peak is the same as elastic loading but in the opposite direction (indicated by the two red arrows in Fig. 2.8).

Finally, to illustrate the material behaviour under unloading-reloading cycles, the response of simulated unloading-reloading cycles compression test is plotted in Fig. 2.9 for $r_0 = 0.5\;MPa$, $r_1 = 0.2$, and considering exponential damage evolution law. It can be observed that, in an unloading-reloading cycle, the behaviour is elastic and the elastic parameter (i.e. modulus of elasticity E) corresponds to the current secant stiffness at the current damaged state. Evolution of the damage multiplier λ^d is also plotted. It remains constant during the unloading-reloading cycles.

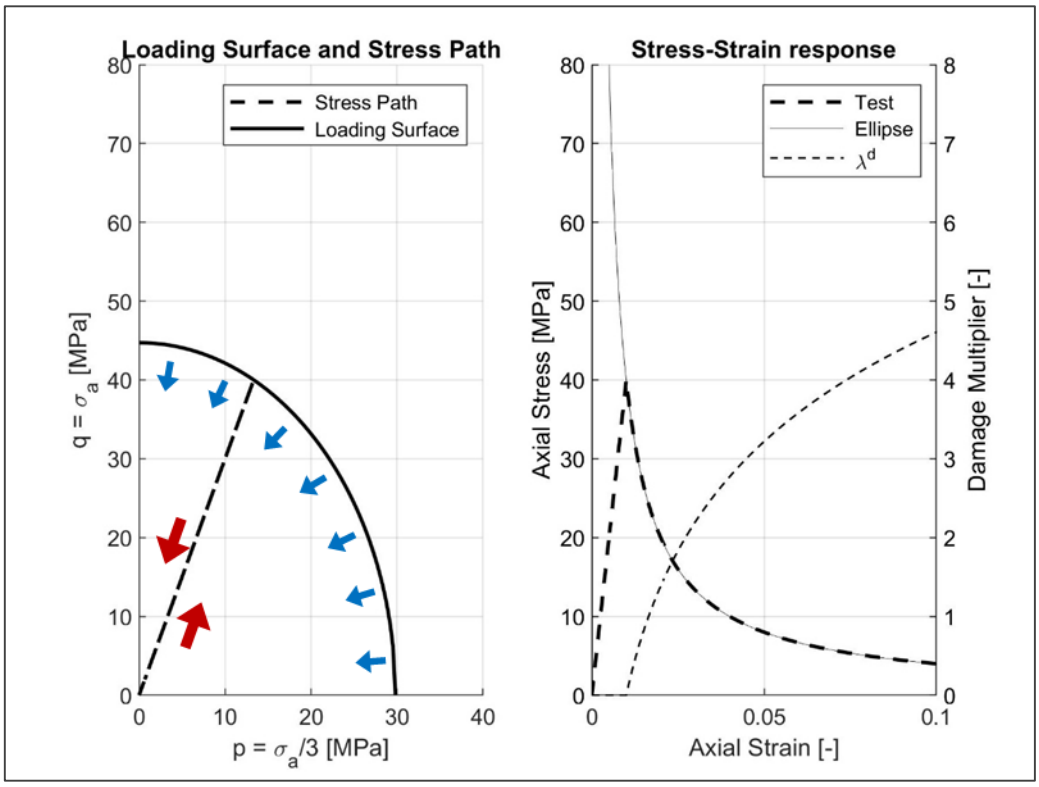

Figure 2.8: Hyperbola idealizing the damage locus and evolution of damage multiplier

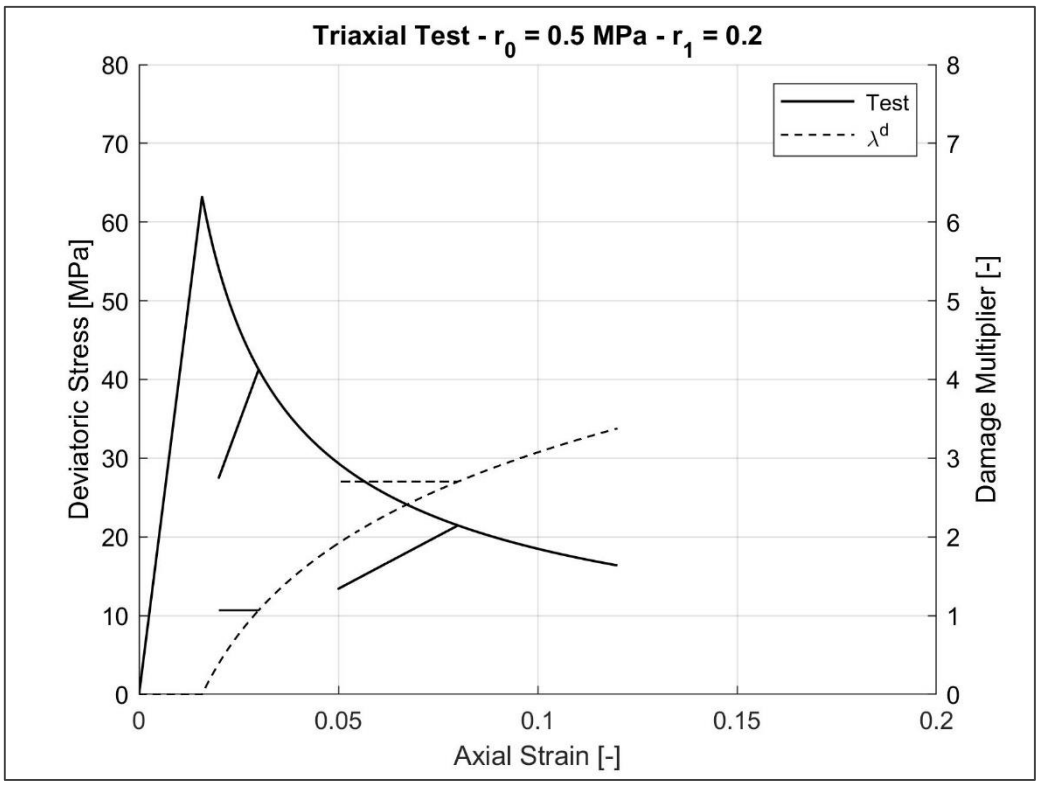

Figure 2.9: Unloading - reloading cycles

Chapter 3

Coupled damage-elastoplastic model formulation

The basis of this type of composite model was developed for argillaceous rocks by *Vaunat and Gens (2003)* and then implemented by other authors (e.g. Gens et al., 2007; Pinyol et al., 2007). As described by *Vaunat and Gens (2003)*, the model combines the approaches proposed for structured materials into a single comprehensive framework able to reproduce the cohesive-frictional transition of material as bonding level decreases. This framework extends the concepts of limit and critical states initially developed for soils to structured materials by introducing a dependency of the yield surface on a structuration parameter.

In this section the model is first described taking as a reference the developed by *Vaunat and Gens (2003)*. Different definition for the structuration parameter is proposed and a new parameter controlling the rate of de-structuring is introduced.

3.1.- Basics assumptions for the formulation

As described in *Vaunat and Gens (2003)*, the basis of the model consists in considering a composite material made by two different materials: the *matrix* and the *bonds*, which partially occupy the pores of the medium. The schematic arrangement of the composite material follow that one showed in Fig. 3.1. In the case of cemented sands, the matrix are the sand particles and the bonds are the cementitious agent deposited at the intergranular contact.

When an external load is applied to the medium, part of the stresses will be carried by the sand particles (i.e. the matrix) and part by the bonding material and, therefore, both materials will experience different local values of stresses and strains determined by the stress-strain relationship resulting of the behaviour of each material. These values of stress and strains are constrained by two conditions. One is that the local strains must be compatible with externally applied deformations, and the other is that local stresses must be in equilibrium with the external load.

In order to consider the compatibility of strains condition, volumetric strain relationship will be first written and then the results will be generalized to triaxial conditions. To do that, different volumetric strain rate can be defined from Fig. 3.1. The volumetric strain rate associated with the rate of pore size change $d\varepsilon_v^v$, is defined in Eq. 3.1a, while the volumetric strain rate of the bonding material $d\varepsilon_v^b$, is defined in Eq. 3.1b. Is important to note that $d\varepsilon_v^b$ must be defined locally (i.e. in terms of the volume of bonding material V_b

and not the total volume V_T). This is because, as it will be exposed later, $d\varepsilon_v^b$ is involved in the (local) stress-strain behaviour defined by the bond material constitutive model (i.e. in this case, the damage model for the cementitious agent).

There is not considered a change in volume of sand particles. The rate of change in volume between the matrix particles is defined in Eq. 3.2a. It includes the rate of change in volume of pores and the rate of change of bond material volume. $d\varepsilon_v^M$ can be considered as a measurement of the relative motion of sand particles and will be involved in the stress-strain behaviour defined by the constitutive model related to the matrix material (i.e. in this case, the elastoplastic model considered for the sand). The externally observed volumetric strain rate $d\varepsilon_v^{EXT}$ is, in fact, equal to $d\varepsilon_v^M$ as indicated in the equality of the first part of Eq. 3.3, where the relation defined in Eq. 3.2a was generalized to triaxial conditions.

c_b is the *volume concentration of bond material* defined as the volume of cement by unit volume of total composite material (Eq. 3.2b). Usually in the literature the bond concentration is reported as weight of cement by weight of dry soil (indicated by c_b^* in this work). To obtain one when the other is given, relations presented in Eq. 3.4 would be useful, where γ_c and γ_s are the specific weight of cement and solid particles respectively, and e is the classical void ratio.

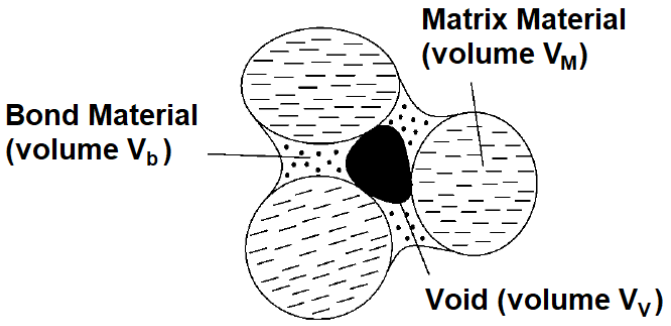

Figure 3.1: Schematic arrangement of the composite material (after *Vaunat and Gens, 2003*)

$$d\varepsilon_v^v = -\frac{\Delta V_v}{V_T} \qquad d\varepsilon_v^b = -\frac{\Delta V_b}{V_b} \qquad (Eq.\,3.1\ a,b)$$

$$d\varepsilon_v^M = -\frac{\Delta V_v + \Delta V_b}{V_T} = d\varepsilon_v^v + c_b d\varepsilon_v^b \qquad with \qquad c_b = \frac{V_b}{V_T} \qquad (Eq.\,3.2\ a,b)$$

$$d\varepsilon_{ij}^M = d\varepsilon_{ij}^{EXT} = d\varepsilon_{ij}^v + c_b d\varepsilon_{ij}^b \qquad (Eq.\,3.3)$$

$$c_b^* = c_b \frac{\gamma_c}{\gamma_s} \frac{1+e}{1-c_b} \qquad c_b = \left(1 + \frac{\gamma_c}{\gamma_s} \frac{1+e}{c_b^*}\right)^{-1} \qquad (Eq.\,3.4\ a,b)$$

3.2.- Strain rate partition

The formulation continues with the definition of the relationship between the different strain rate mentioned in the previous section (i.e. strain rate partition). The key assumption of this coupled model is that a relation between $d\varepsilon_{ij}^{v}$ and $d\varepsilon_{ij}^{b}$ exists at all times and can be written as Eq. 3.5, where χ is the structuration parameter. In *Vaunat and Gens (2003),* this parameter was defined in a restrictive way from energy equivalence principle in terms of accumulated strains ε_{ij}^{v} and ε_{ij}^{b} instead of the strain rates $d\varepsilon_{ij}^{v}$ and $d\varepsilon_{ij}^{b}$. In this work, χ parameter is defined in a more general way as the ratio between the strain rates.

The structuration parameter χ can be devised as a measurement of the distribution and effectiveness of bond material in the general structuration of the composite material (the higher χ the more structured is the composite material due to bond effectiveness). As defined, for a given c_b, χ determines how the external strain rate is distributed between rate of change in pore size and rate in change in bond volume. Also, as it will be explained immediately, χ influences the distribution of external stresses among the bond and matrix material.

$$\chi = \frac{d\varepsilon_{ij}^{b}}{d\varepsilon_{ij}^{v}} \qquad (Eq.\,3.5)$$

$$d\varepsilon_{ij}^{v} = \frac{1}{1 + c_b\chi} d\varepsilon_{ij}^{EXT} \qquad (Eq.\,3.6)$$

$$d\varepsilon_{ij}^{b} = \frac{\chi}{1 + c_b\chi} d\varepsilon_{ij}^{EXT} \qquad and \qquad c_b d\varepsilon_{ij}^{b} = \frac{c_b\chi}{1 + c_b\chi} d\varepsilon_{ij}^{EXT} \qquad (Eq.\,3.7\ a,b)$$

$$d\varepsilon_{ij}^{M} = d\varepsilon_{ij}^{EXT} = (1 + c_b\chi)\, d\varepsilon_{ij}^{v} \qquad (Eq.\,3.8)$$

From Eq. 3.3 and Eq. 3.5, some useful relationship can be derived (Eq. 3.6 to Eq. 3.8). To illustrate how χ works in the strain rate partition, evolution of $d\varepsilon_{ij}^{v}$ and $c_b d\varepsilon_{ij}^{b}$ with χ (for given c_b and normalized with $d\varepsilon_{ij}^{EXT}$) are plotted in Fig. 3.2. Note that the product $c_b d\varepsilon_{ij}^{b}$ is considered instead of just $d\varepsilon_{ij}^{b}$, because, as previously explained, $d\varepsilon_{ij}^{b}$ was defined locally and, in order to be comparable with $d\varepsilon_{ij}^{v}$, must be related to the total volume.

Note from Fig. 3.2 that, for a given c_b, the more structured is the material, the lower is the rate of change in pore size and the higher is the rate in change in bond volume. In the case of $\chi = 0$ (i.e. completely de-structured material) the external strain rate is all attributed to rate of change in pore size, and the response of the composite material would be defined by the matrix material behaviour (i.e. de-structured sand). In the case of a high value of χ (i.e. high level of structuration), the external strain rate is almost all attributed to rate of change in bond volume, and the response of the composite material

would be defined by the cement behaviour (i.e. defined by the damage model). This effect is, as expected, more pronounced for higher values of bond concentration.

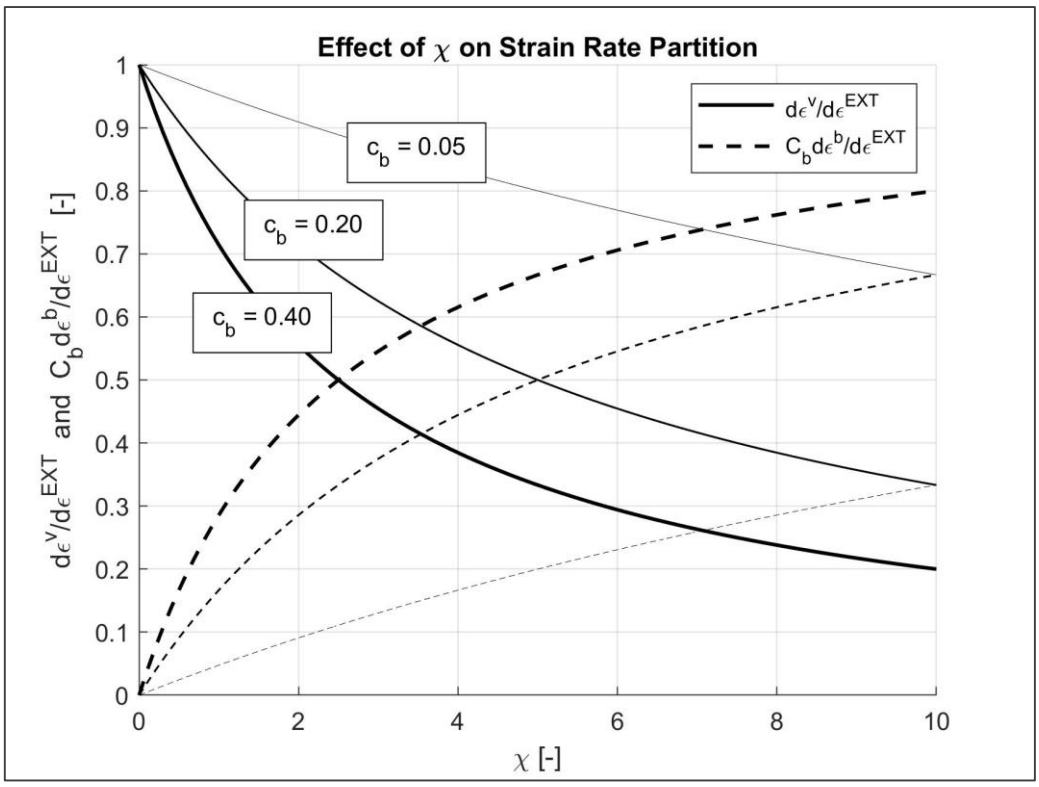

Figure 3.2: Effect of χ on strain rate partition

When the structured composite material is subjected to a loading process, the material suffers a destructuring process. It is assumed then, that the value of the structuration parameter is not constant and depends on the level of bond damage (i.e. it depends on the damage multiplier λ^d defined in the previous chapter). When the bond material is undamaged, a constant initial value χ_o is assumed. It provides the strain rate partition before bond damage process starts. The evolution of the structuration parameter with bond damage is supposed of exponential type as denoted in Eq. 3.9a. β_χ is a new parameter introduced to control the destructuring rate. In Eq. 3.9b, the differentiation of Eq. 3.9a is presented.

$$\chi = \chi_o e^{-\beta_\chi \lambda^d} \qquad and \qquad d\chi = -\beta_\chi \chi \, d\lambda^d \qquad (Eq.\,3.9\ a,b)$$

To illustrate now how the damage multiplier influences the strain rate partition, evolution of $d\varepsilon_{ij}^v$ and $c_b d\varepsilon_{ij}^b$ with λ^d (normalized with $d\varepsilon_{ij}^{EXT}$) are plotted in Fig. 3.3, Fig. 3.4, and Fig. 3.5, for given c_b, for given χ_o and for given β_χ respectively. As expected, the higher λ^d is, the lower the rate of change in bond volume is (i.e. less structured material). Also from Fig. 3.4 and Fig. 3.5 one can observe how χ_o defines the strain rate relationships at the beginning, and how β_χ controls the "speed" of the destructuring process.

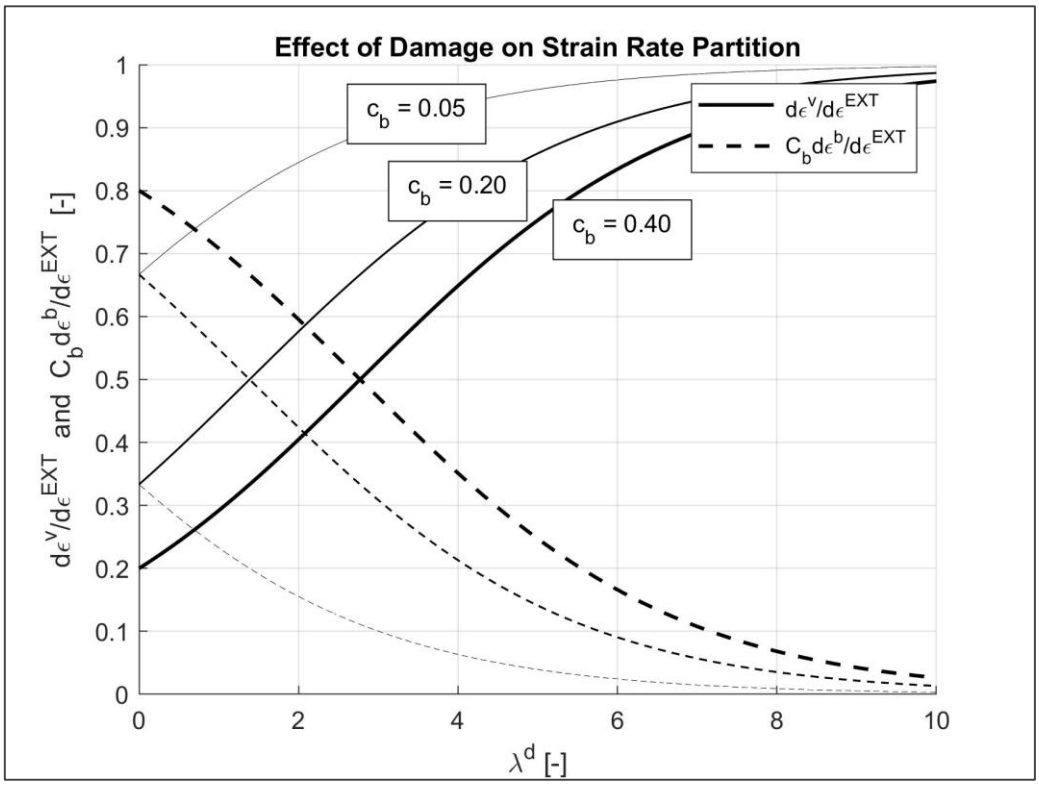

Figure 3.3: Effect of damage on strain rate partition - given C_b

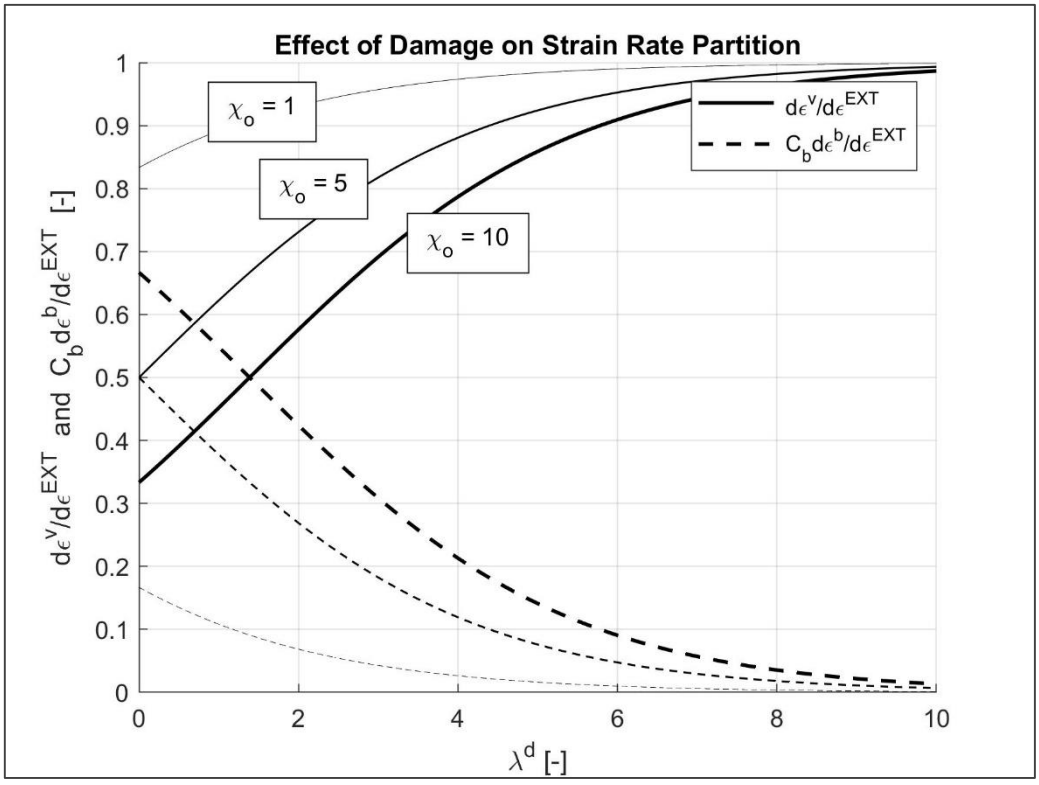

Figure 3.4: Effect of damage on strain rate partition - given χ_o

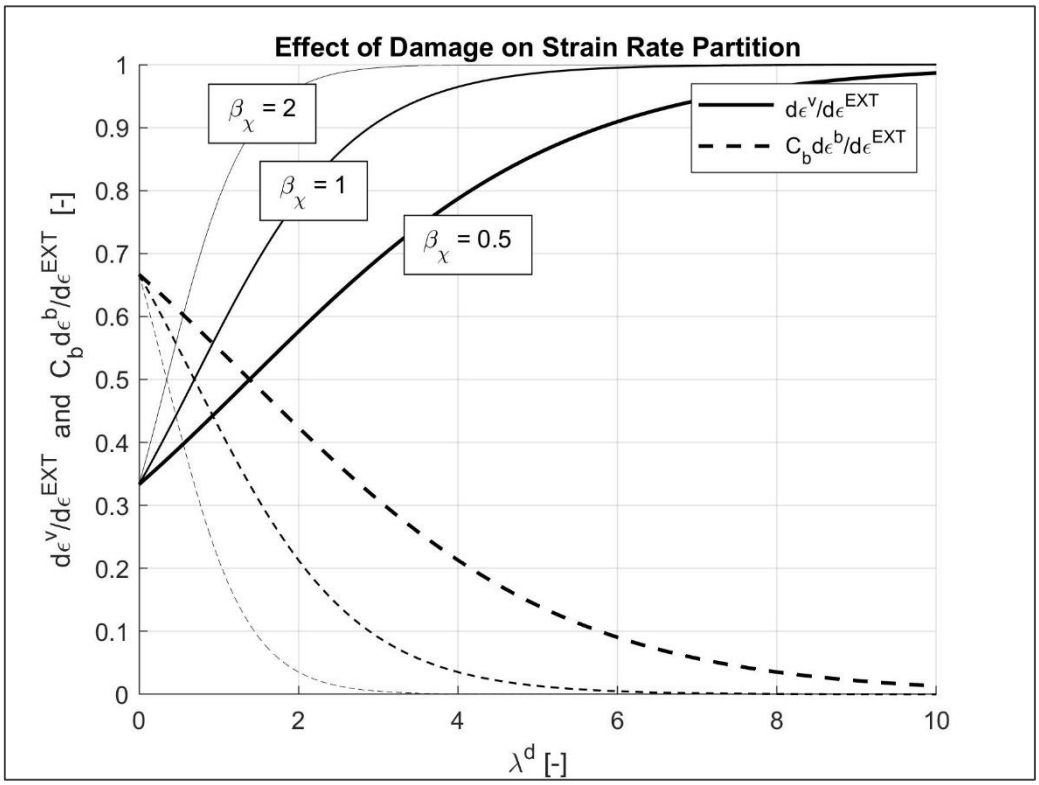

Figure 3.5: Effect of damage on strain rate partition - given β_χ

3.3.- Stress partition

In order to derive an expression for the external stresses σ_{ij}^{EXT} in terms of the local matrix and local bond stresses σ_{ij}^{M} and σ_{ij}^{b}, the principle of virtual work is applied. Local equilibrium is ensured if the work of external stresses during any increment of strain is equal to the work of stresses inside the bonds and matrix material as expressed in Eq. 3.10.

Operating with Eq. 3.7 and Eq. 3.8, Eq. 3.10 can be rewritten as Eq. 3.11. This equation is valid for any external change in strain and provides an expression to compute the external stress in terms of local bond and matrix stresses. For any increment of external strain $d\varepsilon_{ij}^{EXT}$ (i.e. $d\varepsilon_{ij}^{M}$), the incremental bond strain is determined by the current value of χ and bond concetration c_b through Eq. 3.7. Then integrating the constitutive models (damage model for the bond material and elastoplastic model for the sand) incremental stresses $d\sigma_{ij}^{M}$ and $d\sigma_{ij}^{b}$ are calculated and σ_{ij}^{M} and σ_{ij}^{b} updated. Finally, the direct use of Eq. 3.11 provides the value of the updated σ_{ij}^{EXT}.

$$\sigma_{ij}^{EXT} d\varepsilon_{ij}^{v} = \sigma_{ij}^{M} d\varepsilon_{ij}^{M} + \sigma_{ij}^{b}\, c_b d\varepsilon_{ij}^{b} \qquad (Eq.3.10)$$

$$\sigma_{ij}^{EXT} = (1 + c_b\chi)\, \sigma_{ij}^{M} + c_b\chi\, \sigma_{ij}^{b} \qquad (Eq.3.11)$$

It is interesting, and in some cases useful, to derive an expression for the "*coupled damage-elastoplastic tangent stiffness for the composite material*" $D_{ijkl}^{EDP\,tan}$ that relates the external stress increment $d\sigma_{ij}^{EXT}$ to the external strain increment $d\varepsilon_{ij}^{EXT}$. In order to do that, differentiation of Eq. 3.11 is first derived in Eq. 3.12 and then rewritten as Eq. Eq. 3.13. As can be observed in this expression, the increment of external stress is determined by the increment of matrix and bond stresses as explained before, but also by the variation of the structuration parameter $d\chi$, which is directly related to the variation of damage multiplier $d\lambda^d$ through Eq. 3.9b.

$$d\sigma_{ij}^{EXT} = (1 + c_b\chi)\, d\sigma_{ij}^{M} + c_b\chi\, d\sigma_{ij}^{b} + c_b d\chi \left(\sigma_{ij}^{M} + \sigma_{ij}^{b}\right) \qquad (Eq.3.12)$$

$$d\sigma_{ij}^{EXT} = (1 + c_b\chi)\, d\sigma_{ij}^{M} + c_b\chi\, d\sigma_{ij}^{b} - c_b\, \beta_\chi\, \chi\left(\sigma_{ij}^{M} + \sigma_{ij}^{b}\right) d\lambda^d \qquad (Eq.3.13)$$

The matrix stress increment $d\sigma_{ij}^{M}$ for an external stress increment is determined by the matrix constitutive law as indicated in Eq. 3.14, where ${D_{ijkl}^{M}}^{tan}$ is the tangent stiffness matrix for the matrix material. Taking into account that $d\varepsilon_{kl}^{EXT}$ is equal to $d\varepsilon_{kl}^{M}$ (with the physical meaning of the relative motion of sand particles), ${D_{ijkl}^{M}}^{tan}$ is defined through Eq. 2.14 from Chapter 2 where the tangent stiffness matrix for the elastoplastic formulation was obtained. The expression is rewritten in Eq. 3.15, now with D_{ijkl}^{M} as the elastic stiffness tensor of the matrix material.

$$d\sigma_{ij}^{M} = {D_{ijkl}^{M}}^{tan} d\varepsilon_{kl}^{M} = {D_{ijkl}^{M}}^{tan} d\varepsilon_{kl}^{EXT} \qquad (Eq.3.14)$$

$${D_{ijkl}^{M}}^{tan} = D_{ijkl}^{M} - \frac{D_{ijmn}^{M}\, m_{mn}^{p}\, \dfrac{\partial F^{p}}{\partial \sigma_{pq}} D_{pqkl}^{M}}{H^{p} - H_{cr}^{p}} \qquad (Eq.3.15)$$

For its part, the bond stress increment $d\sigma_{ij}^{b}$ can be determined by the bond constitutive law as indicated in Eq. 3.16, where ${D_{ijkl}^{b}}^{tan}$ is the tangent stiffness matrix for the bond material. The difference is that, in this case, $d\sigma_{ij}^{b}$ is related to the local strain increment of bond $d\varepsilon_{kl}^{b}$ instead of $d\varepsilon_{kl}^{EXT}$. With the relation established in Eq. 3.7 one can write Eq. 3.17 where $d\sigma_{ij}^{b}$ is now related to $d\varepsilon_{kl}^{EXT}$. ${D_{ijkl}^{b}}^{tan}$ is defined through Eq. 2.69 from Chapter 2 where the tangent stiffness matrix for an isotropic scalar damage model was obtained. The expression is rewritten in Eq. 3.18 and Eq. 3.19, now considering D_{ijkl}^{b} as the elastic secant stiffness tensor for the bond material and ${D_{ijkl}^{b}}^{0}$ the initial one (i.e. undamaged state). The mechanical free energy of the bond material u^b is redefined in Eq. 3.20.

$$d\sigma_{ij}^{b} = {D_{ijkl}^{b}}^{tan} d\varepsilon_{kl}^{b} \qquad (Eq.3.16)$$

$$d\sigma_{ij}^{b} = \frac{\chi}{1 + c_b \chi} D_{ijkl}^{b}{}^{tan} d\varepsilon_{ij}^{EXT} \qquad (Eq.\,3.17)$$

$$D_{ijkl}^{b}{}^{tan} = D_{ijkl}^{b} - \frac{\sigma_{ij}^{b}\ \sigma_{kl}^{b}}{h^{d} + u^{b}} \qquad (Eq.\,3.18)$$

$$D_{ijkl}^{b}{}^{tan} = e^{-\lambda^{d}}\ D_{ijkl}^{b\ 0} - \frac{\sigma_{ij}^{b}\ \sigma_{kl}^{b}}{h^{d} + u^{b}} \qquad (Eq.\,3.19)$$

$$u^{b} = \frac{1}{2}\sigma_{ij}^{b}\ \varepsilon_{ij}^{b} \qquad (Eq.\,3.20)$$

The damage multiplier is conveniently redefined in Eq. 3.21 from Eq. 2.69. Finally, Eq. 3.15, Eq. 3.18 and Eq. 3.21 are substituted in Eq. 3.13, leading to Eq. 3.22. After some operations one obtains Eq. 3.23, where $D_{ijkl}^{b\ *}{}^{tan}$ is defined in Eq. 3.24 (or Eq. 3.25) and denoted with * symbol to difference from $D_{ijkl}^{b}{}^{tan}$.

The coupled damage-elastoplastic tangent stiffness tensor for the composite material $D_{ijkl}^{EDP\,tan}$ can be identified in Eq. 3.23 and written as Eq. 3.26. Note that it is a composition of the tangent stiffness tensors $D_{ijkl}^{M}{}^{tan}$ and $D_{ijkl}^{b\ *}{}^{tan}$ defined previously.

$$d\lambda^{d} = \frac{\chi}{1 + c_b \chi}\ \frac{\sigma_{kl}^{b}}{h^{d} + u^{b}} d\varepsilon_{kl}^{EXT} \qquad (Eq.\,3.21)$$

$$d\sigma_{ij}^{EXT} = (1 + c_b \chi)\ D_{ijkl}^{M}{}^{tan} d\varepsilon_{kl}^{EXT} + \frac{c_b \chi^{2}}{1 + c_b \chi} D_{ijkl}^{b}{}^{tan} d\varepsilon_{ij}^{EXT} \quad \cdots$$
$$- \beta_{\chi}\left(\sigma_{ij}^{M} + \sigma_{ij}^{b}\right) \frac{c_b \chi^{2}}{1 + c_b \chi}\ \frac{\sigma_{kl}^{b}}{h^{d} + u^{b}} d\varepsilon_{kl}^{EXT} \qquad (Eq.\,3.22)$$

$$d\sigma_{ij}^{EXT} = \left\{(1 + c_b \chi)\ D_{ijkl}^{M}{}^{tan} + \frac{c_b \chi^{2}}{1 + c_b \chi} D_{ijkl}^{b\ *}{}^{tan}\right\} d\varepsilon_{kl}^{EXT} \qquad (Eq.\,3.23)$$

$$D_{ijkl}^{b\ *}{}^{tan} = D_{ijkl}^{b}{}^{tan} - \beta_{\chi}\ \frac{(\sigma_{ij}^{M} + \sigma_{ij}^{b})\sigma_{kl}^{b}}{h^{d} + u^{b}} \qquad (Eq.\,3.24)$$

$$D_{ijkl}^{b\ *}{}^{tan} = D_{ijkl}^{b} - \frac{\left[\beta_{\chi}\sigma_{ij}^{M} - \left(1 + \beta_{\chi}\right)\sigma_{ij}^{b}\right]\sigma_{kl}^{b}}{h^{d} + u^{b}} \qquad (Eq.\,3.25)$$

$$D_{ijkl}^{EDP\,tan} = (1 + c_b \chi)\ D_{ijkl}^{M}{}^{tan} + \frac{c_b \chi^{2}}{1 + c_b \chi} D_{ijkl}^{b\ *}{}^{tan} \qquad (Eq.\,3.26)$$

3.4.- Effect of structuration on matrix and bond loading surfaces

From Eq. 3.11, one can obtain the expressions for the external mean and deviatoric stress respectively (p^{EXT} and q^{EXT} in Eq. 3.27 and 3.28) as a composition of the mean and deviatoric stress of the matrix (p^M and q^M) and the bond material (p^b and q^b). From these expressions, useful relations between the stress components are obtained as shown in Eq. 3.29 to Eq. 3.32.

$$p^{EXT} = (1 + c_b\chi)\, p^M + c_b\chi\, p^b \qquad (Eq.3.27)$$

$$q^{EXT} = (1 + c_b\chi)\, q^M + c_b\chi\, q^b \qquad (Eq.3.28)$$

$$p^b = \frac{p^{EXT} - (1 + c_b\chi)\, p^M}{c_b\chi} \qquad (Eq.3.29)$$

$$q^b = \frac{q^{EXT} - (1 + c_b\chi)\, q^M}{c_b\chi} \qquad (Eq.3.30)$$

$$p^M = \frac{p^{EXT} - c_b\chi\, p^b}{1 + c_b\chi} \qquad (Eq.3.31)$$

$$q^M = \frac{q^{EXT} - c_b\chi\, q^b}{1 + c_b\chi} \qquad (Eq.3.32)$$

The loading surface for bond material in the p^b-q^b space was presented in Eq. 2.81 and rewritten now in Eq. 3.33 in terms of p^b and q^b. Superscript "b" in K^b and G^b indicates that it is a parameter related to the bond material. Substituting Eq. 3.29 and Eq. 3.30, one obtains Eq. 3.34. This expression corresponds to the bond loading surface but now in the p^{EXT}-q^{EXT} space.

Note that Eq. 3.34 represents again an ellipse, but now with scaled radius $c_b\chi\sqrt{2Kr}$ and $c_b\chi\sqrt{6Gr}$, and centered on the coordinates $(1 + c_b\chi)\, p^M$ and $(1 + c_b\chi)\, q^M$ as showed in Fig. 3.6. As observed, the coordinates of the center depends on the matrix stresses p^M and q^M, so the ellipse "moves" when the stress in the matrix varies. For example, at the time of bond deposition the ellipse would be centered on the coordinates related to the curing stresses. The radius now depends not only on r^b and the degraded current stiffness (K^b and G^b) but also on the structuration parameter χ. Note that all these parameters depend directly on the damage multiplier λ^d.

$$\frac{{p^b}^2}{2\, K^b\, r^b} + \frac{{q^b}^2}{6\, G^b\, r^b} = 1 \qquad (Eq.3.33)$$

$$\frac{[p^{EXT} - (1 + c_b\chi)\, p^M]^2}{2\, K^b\, r^b\, (c_b\chi)^2} + \frac{[q^{EXT} - (1 + c_b\chi)\, q^M]^2}{6\, G^b\, r^b\, (c_b\chi)^2} = 1 \qquad (Eq\ 3.34)$$

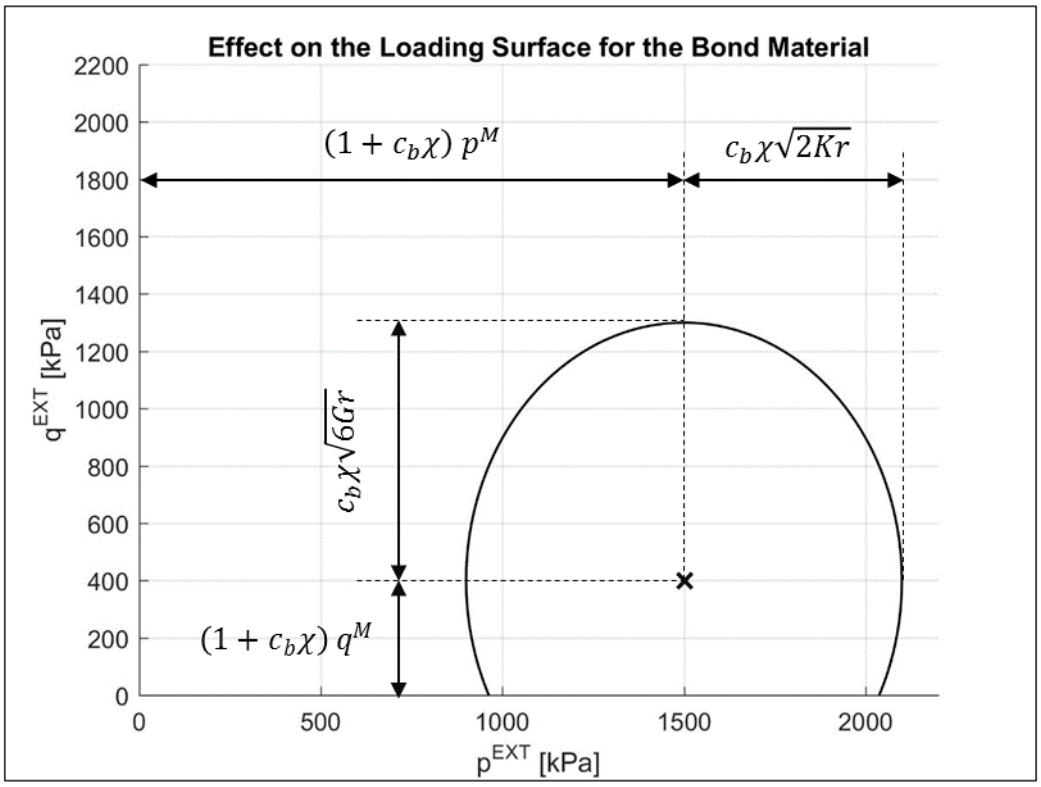

Figure 3.6: Effect of structuration on the loading surface for bond material

The same procedure can be applied to the matrix sand. Two elastoplastic criteria are considered in this case: Mohr Coulomb Model and Modified Cam Clay Model (MCCM). In Eq. 3.35 the elastoplastic loading surface for Mohr Coulomb model is presented, where A and B are defined in Eq. 3.36, and c^M and φ^M are the cohesion and frictional angle of the matrix material respectively. Substituting Eq. 3.31 and Eq. 3.32, one obtains Eq. 3.37. This expression corresponds to the matrix loading surface but now in the p^{EXT}-q^{EXT} space. q^* and p^* are defined in Eq. 3.38.

$$F^p = q^M - A\, p^M - B\, c^M = 0 \qquad (Eq.\,3.35)$$

$$A = \frac{6\sin\varphi^M}{3 - \sin\varphi^M} \qquad and \qquad B = \frac{6\cos\varphi^M}{3 - \sin\varphi^M} \qquad (Eq.\,3.36\ a, b)$$

$$F^p = q^* - A\, p^* - (1 + c_b\chi)\, B\, c^M = 0 \qquad (Eq.\,3.37)$$

$$q^* = q^{EXT} - c_b\chi\, q^b \quad and \quad p^* = p^{EXT} - c_b\chi\, p^b \qquad (Eq.\,3.38\ a, b)$$

Note that Eq. 3.36 represents the typical straight line loading surface for Mohr Coulomb Model but, for the structured material, the cohesion is scaled with $(1 + c_b\chi)$ (see Fig. 3.7). The friction angle is not affected, in agreement with the observed effect of cementation in some laboratory tests, where several authors found that the cohesion increases with cementation and the frictional angle remains almost invariable.

From Eq. 3.37 one can also note that, when the bond material is loaded (i.e. q^b and p^b are different to zero), the straight line representing the loading surface "moves" a quantity equal to $c_b\chi\, p^b$ and $c_b\chi\, q^b$ for the p-axis direction and q-axis direction respectively (see the definitions of q^* and p^* in Eq. 3.35). This kind of movement, results in an increase (or decrease) of the cohesion intercept as indicated in Fig. 3.7.

The elastoplastic loading surface considering MCCM is presented in Eq. 3.39, where M and ${p_o}^M$ are the slope of the critical state line and the preconsolidation stress respectively. Substituting Eq. 3.31 and Eq. 3.32, one obtains Eq. 3.40. This expression corresponds to the matrix loading surface but now in the p^{EXT}-q^{EXT} space.

$$F^p = {q^M}^2 + M^2\, p^M(p^M - {p_o}^M) = 0 \qquad (Eq.\,3.39)$$

$$F^p = {q^*}^2 + M^2\, p^*[p^* - (1 + c_b\chi)\, {p_o}^M] = 0 \qquad (Eq.\,3.40)$$

Note that Eq. 3.40 represents the typical ellipse for MCCM but, for the structured material, the preconsolidation stress is scaled with $(1 + c_b\chi)$, similar to what was observed for the cohesion in Mohr Coulomb Model, so the loading surface is therefore increased. When the bond material is loaded, the ellipse representing the loading surface "moves" a quantity equal to $c_b\chi\, p^b$ and $c_b\chi\, q^b$ to the p-axis direction and q-axis direction respectively. All this aspect are depicted in Fig. 3.8.

Summarizing, to represent the damage locus for bond material and the elastoplastic loading surface for matrix material in the p^{EXT}-q^{EXT} space, the effect of structuration should be considered. A scaling effect was observed for both damage locus and the elastoplastic loading surface, which depends on the structuration parameter and cement concentration. Finally, both surfaces "move" when the other material is loaded, so is not enough to know the external stresses p^{EXT}-q^{EXT}, but it is also necessary to determine the stresses acting in each material.

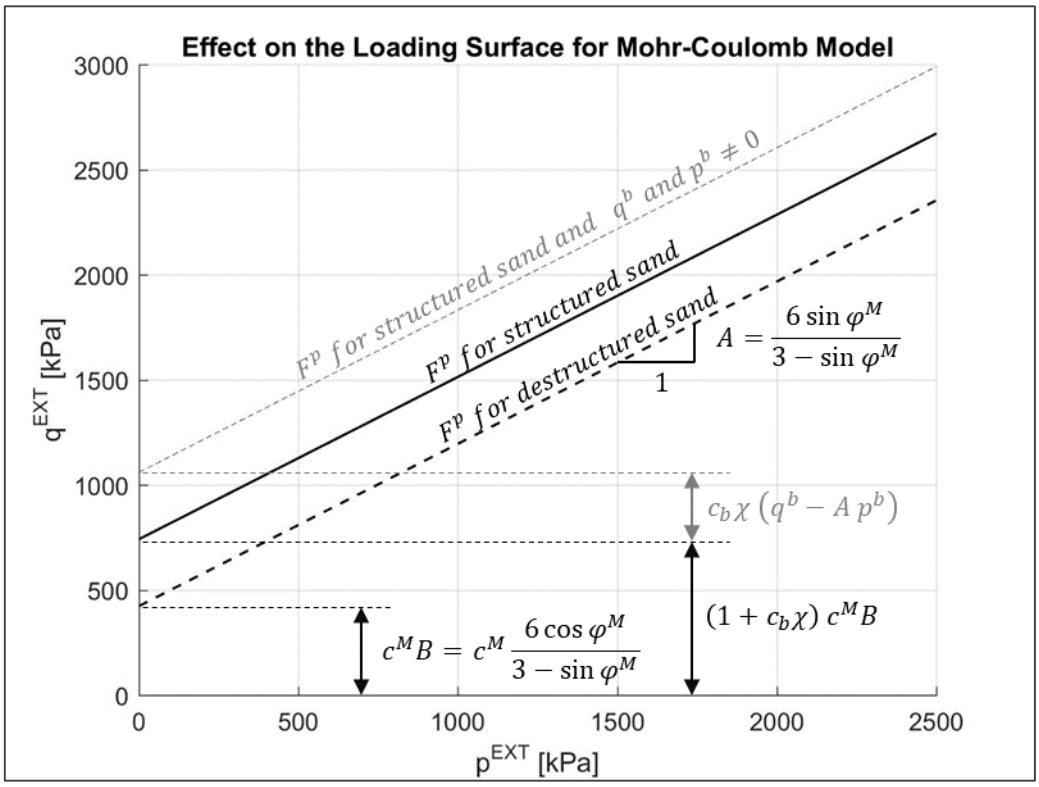

Figure 3.7: Effect of structuration on the loading surface for matrix material (Mohr Coulomb)

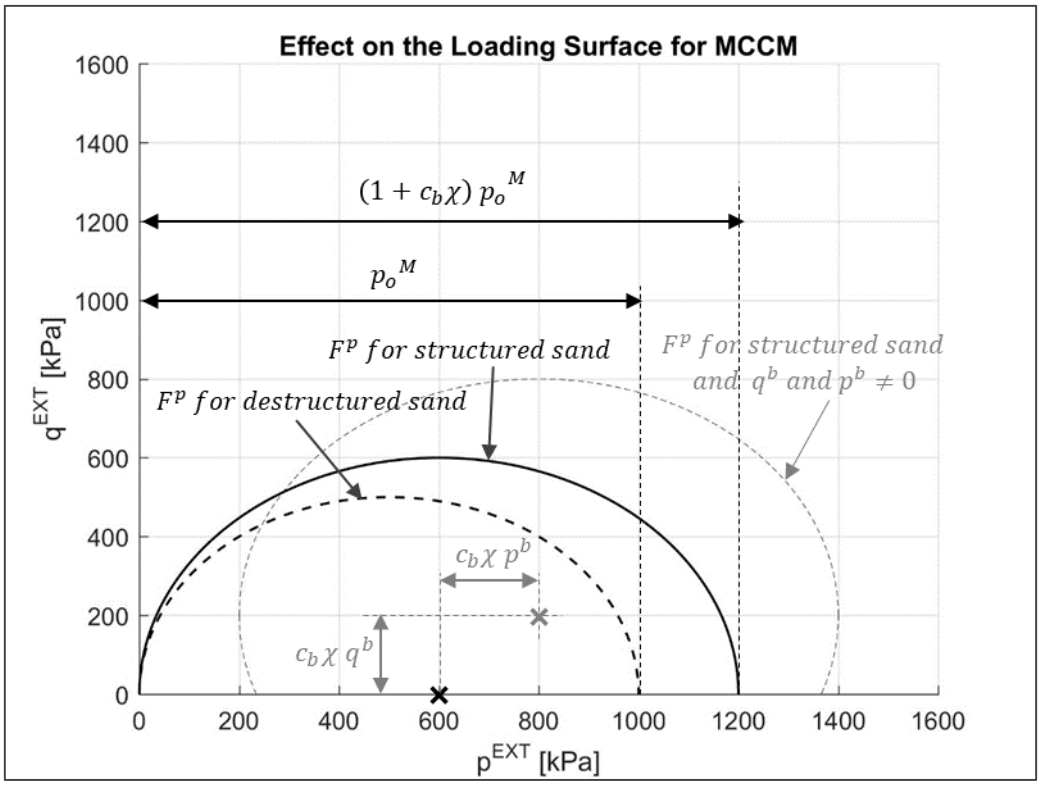

Figure 3.8: Effect of structuration on the loading surface for matrix material (MCCM)

In order to simplify and taking into account that in most reported tests in the literature the samples are cured under isotropic stress conditions, damage locus and plastic loading surfaces for two different isotropic initial states (i.e. q^b and p^b equal to zero) are presented in Fig 3.9. Normally consolidated (top) and slightly oversconsolidated (bottom) initial situations are shown.

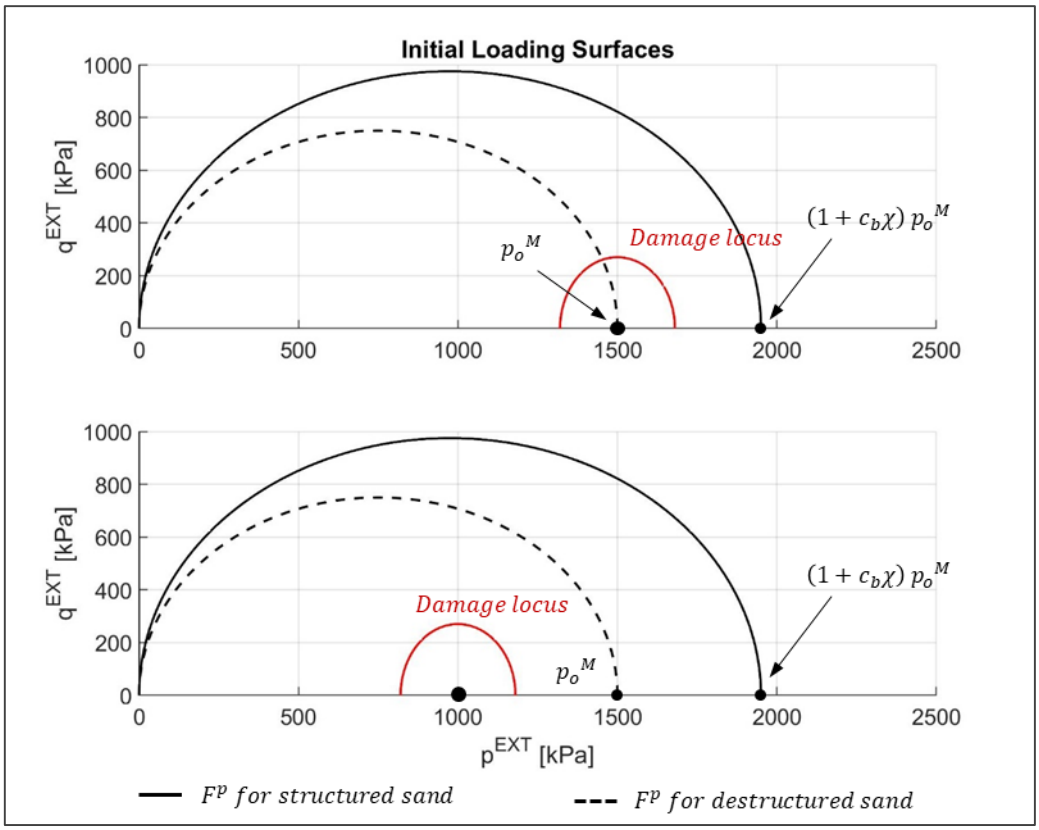

Figure 3.9: Damage locus and plastic loading surfaces

Now, to illustrate how the model works, an increment of the external mean stress p^{EXT} is considered. p^M and p^b should be determined integrating the constitutive models for each material. To simplify, values of p^M and p^b were conveniently established taking into account that the relation of Eq. 3.27 must be satisfied. When an increment of the external mean stress is applied and p^M and p^b are determined, both plastic loading surface and damage locus "move" according the analysis done previously. If the current external stress point lies inside of the surfaces, elastic behaviour would be seen for the composite material. It is also possible that the current external stress point lies outside one or even both surfaces. In these cases, the mechanism of plasticity or damage would be activated and the loading surfaces updated according plasticity or damage theory.

In Fig 3.10, examples of isotropic compression starting from the cases previously presented are shown. In the first case, after the loading surfaces are moved, it can be seen that the current p^{EXT} point lies inside both the damage locus and plastic loading surface. This means that no damage process is occurring in the bond material (i.e. no change in size of the damage locus would be seen) and that no plastic deformation are

developing (i.e. elastic behaviour of the composite material). Note that for this case, because no degrading process is activated, no destructuration occurs. In the second case it can be seen that the current p^{EXT} point lies inside the plastic loading surface but it lies outside the damage locus. This means that no plastic deformation are occurring but the process of degradation of bond is activated and, therefore, destructuration occurs. The loading surface of the structured soil (continuous line) will slowly converge to the destructured state (dashed line).

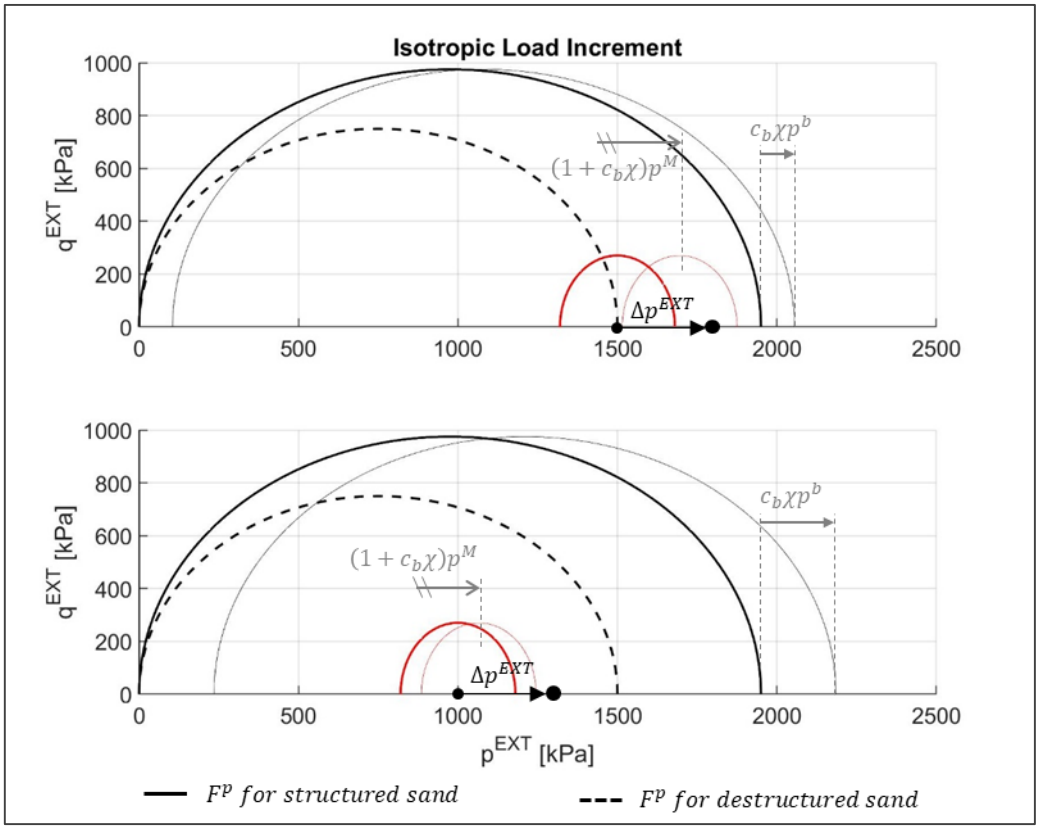

Figure 3.10: Damage locus and plastic loading surfaces

3.5.- Model features through simulated tests

As presented, in addition to the parameters related to the elastoplastic model for the matrix material (i.e. parameters for Mohr Coulomb Model or Modified Cam Clay Model) and the parameters related to the damage model for the bond material (i.e. $E^{0\,b}$, ν^b, r_0^b and r_1^b for isotropic damage model), three new parameters are needed to fully describe the behaviour of the composite material. These are listed in the following lines:

- c_b: it is the volume concentration of bond material defined as the ratio between the volume of bond (i.e. cement) and total volume of the composite material. It is dimensionless and when it is set equal to zero, only matrix material is present in the composite material, and the destructured sand behaviour is recovered. The relation between this parameter and the cement content by dry weight of material c_b^* was established in Eq. 3.4.
- χ_o: it is the value of the structuration parameter for the undamaged state (initial) of bond material. It is dimensionless and, when set equal to zero, completely destructured material is assumed.
- β_χ: it is the parameter controlling the destructuring rate with damage. It is unitless and when it is set equal to zero, no destructuring will be observed and the composite material is integrated always with the initial value χ_o.

In order to illustrate the model capabilities in a parametric study, a few conventional triaxial tests and oedometer tests, have been simulated. In the case of triaxial test, a confinement stress $\sigma_3 = 250\ kPa$ was considered and the elastoplastic behaviour of the sand material was modeled through Mohr-Coulomb model. On the other hand, in the case of odometer tests, the elastoplastic matrix behaviour was modeled through Modified Cam Clay Model (MCCM). The parameters related to the matrix material for triaxial tests and oedometer tests are specified in Table 3.1 and Table 3.2 respectively.

On the other hand, bond material was modeled through the isotropic damage model described in Chapter 2. The initial elastic parameters for bond material (i.e. $E^{0\,b}$, ν^b) were adopted equal for all simulated tests, and the values are presented in Table 3.3. Linear damage evolution law was considered in all the tests presented in this section.

The other parameters, those related to the isotropic damage model of bond material not mentioned before (r_0^b and r_1^b), and those related to the coupled model definition (c_b, χ_o, and β_χ) were analyzed in the parametric study. Tests were grouped in five groups, one for each variable studied. Values adopted for the parametric study are presented in Table 3.4 and Table 3.5 for the triaxial tests and oedometer tests respectively. Superscript “M” or “b” indicates when the parameter is related to the matrix material or to the bond material respectively.

Parameter	Value
E^M $[MPa]$	100
ν^M $[-]$	0.20
c'^M $[kPa]$	0
φ'^M $[°]$	30

Table 3.1: Parameters for matrix material in triaxial tests - Mohr-Coulomb Model[1]

Parameter	Value
$p_0'^M$ $[kPa]$	100
κ^M $[-]$	0.002
ν^M $[-]$	0.20
λ^M $[MPa]$	0.05
M^M $[°]$	0.80

Table 3.2: Parameters for matrix material in oedometer tests - MCCM

Parameter	Value
E^b $[MPa]$	8000
ν^b $[-]$	0.20

Table 3.3: Elastic parameters for bond material in both triaxial and oedometer tests

Parameter	Group TX1	Group TX2	Group TX3	Group TX4	Group TX5
r_0^b $[MPa]$	0.1	0.1	0.1	0.1	Analyzed
r_1^b $[MPa]$	0.3	0.3	0.3	Analyzed	0.3
c_b $[-]$	Analyzed	0.03	0.03	0.03	0.03
χ_o $[-]$	1.0	Analyzed	1.0	1.0	1.0
β_χ $[-]$	1.0	1.0	Analyzed	1.0	1.0

Table 3.4: Parameter for the parametric study in triaxial tests

[1] A linear isotropic hardening law was additionally considered in order to smooth the quasi-perfect elasto-plastic stress-strain curve of the matrix material.

Parameter	Group OD1	Group OD2	Group OD3	Group OD4	Group OD5
r_0^b $[MPa]$	0.01	0.01	0.01	0.01	Analyzed
r_1^b $[MPa]$	0.1	0.1	0.1	Analyzed	0.1
c_b $[-]$	Analyzed	0.01	0.01	0.01	0.01
χ_o $[-]$	1.0	Analyzed	1.0	1.0	1.0
β_χ $[-]$	2.0	2.0	Analyzed	2.0	2.0

Table 3.5: Parameter for the parametric study in triaxial tests

Similar observation can be made from the triaxial tests and oedometer tests results. The effect of bond concentration and the initial structuration parameter is shown in Fig. 3.11 and Fig. 3.12 for the triaxial tests, and in Fig. 3.16 and 3.17 for the oedometer tests. Increasing values of c_b or χ_o result in increasing values of the peak strength for the composite material. The elastic stiffness prior peak increases clearly with increasing values of χ_o, but c_b seems not to be important in this aspect. Also increasing values of χ_o results in decreasing values of the strain at peak.

The effect of the destructuring rate and the damage evolution rate is shown in Fig. 3.13 and Fig. 3.14 for the triaxial tests, and in Fig. 3.18 and 3.19 for the oedometer tests. These parameters control the after peak response: the higher β_χ is, or the lower r_1^b is, more brittle is the after peak response. It seem that they have similar effects, but it is important to remember the difference in the physical meaning. β_χ is a parameter related to the composite material, and its increase means that the material is destrucured faster and, therefore, the bonding material “loses” its effectiveness in connecting sand particles faster. On the other hand, r_1^b is an internal parameter of the constitutive law of bond material, and its decrease means that the fissures in the cement develop faster and, therefore, their elastic properties degrade faster.

The effect of the initial damage locus is shown in Fig. 3.15 and Fig. 3.20 for the triaxial and oedometer tests respectively. The elastic domain for bond material and, therefore, the elastic domain for the composite material increase for increasing values of r_0^b. This also means that the peak strength and brittleness will be higher.

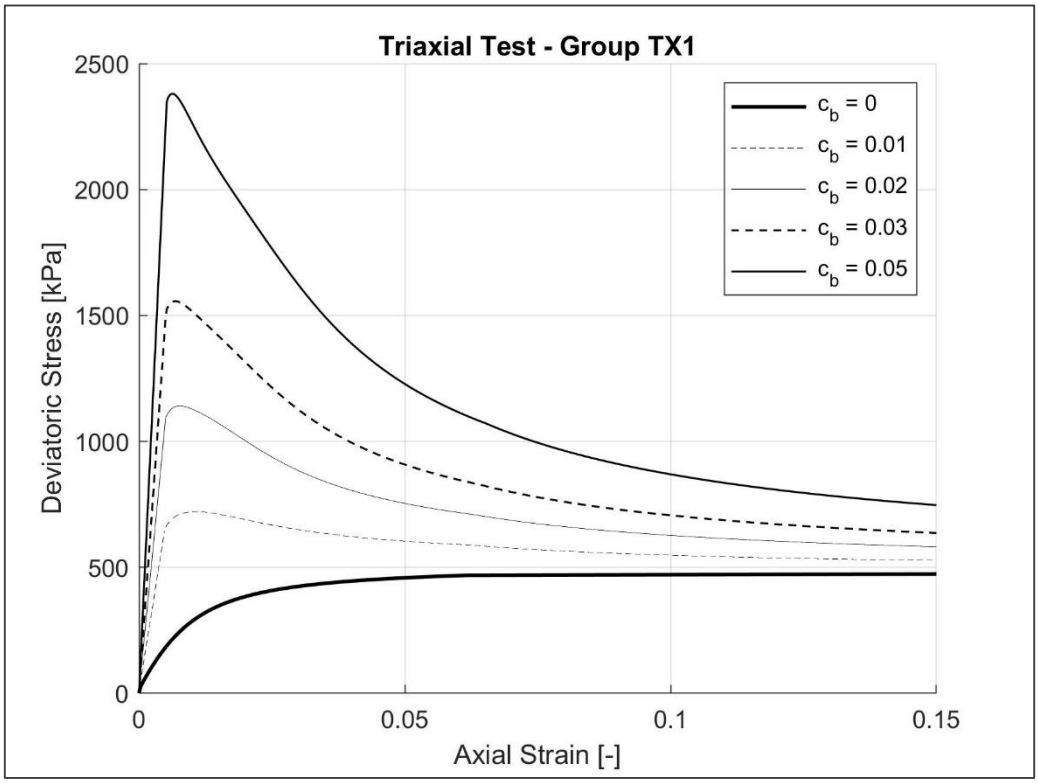

Figure 3.11: Triaxial tests of Group TX1

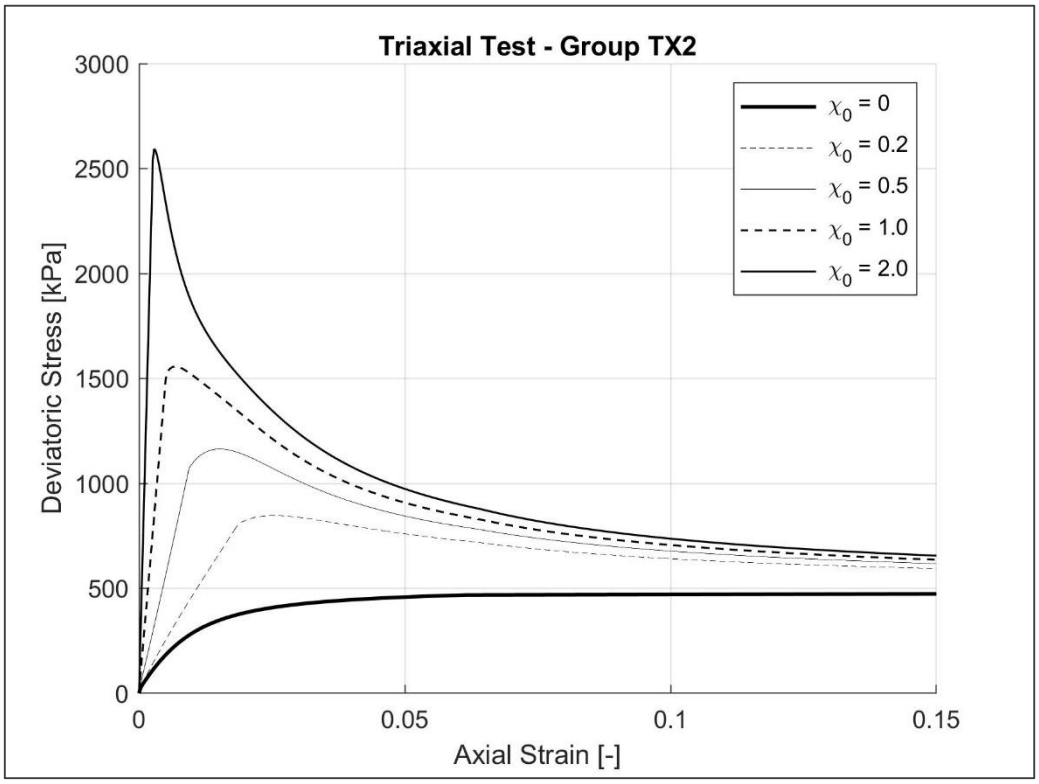

Figure 3.12: Triaxial tests of Group TX2

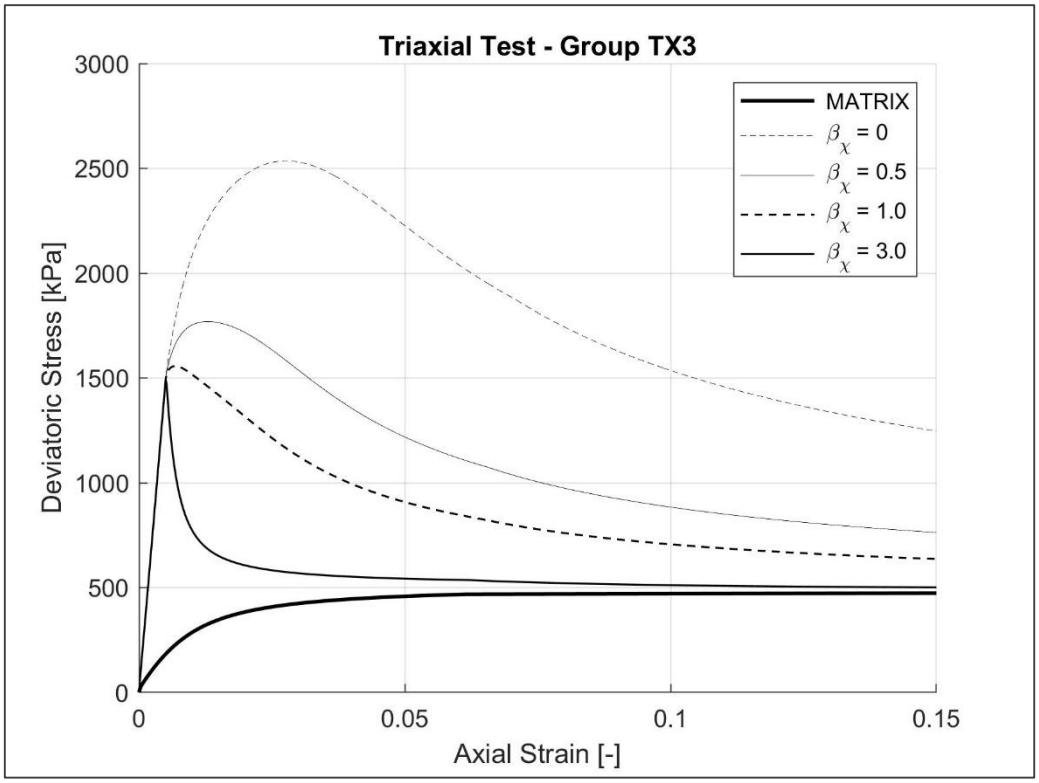

Figure 3.13: Triaxial tests of Group TX3

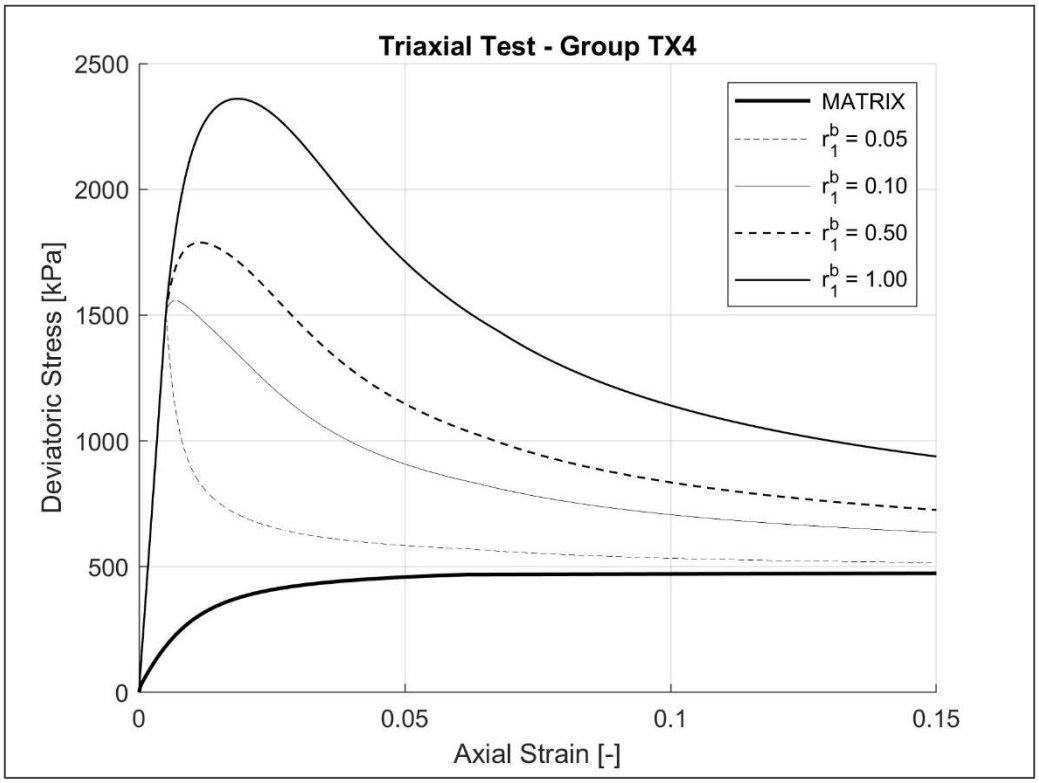

Figure 3.14: Triaxial tests of group TX4

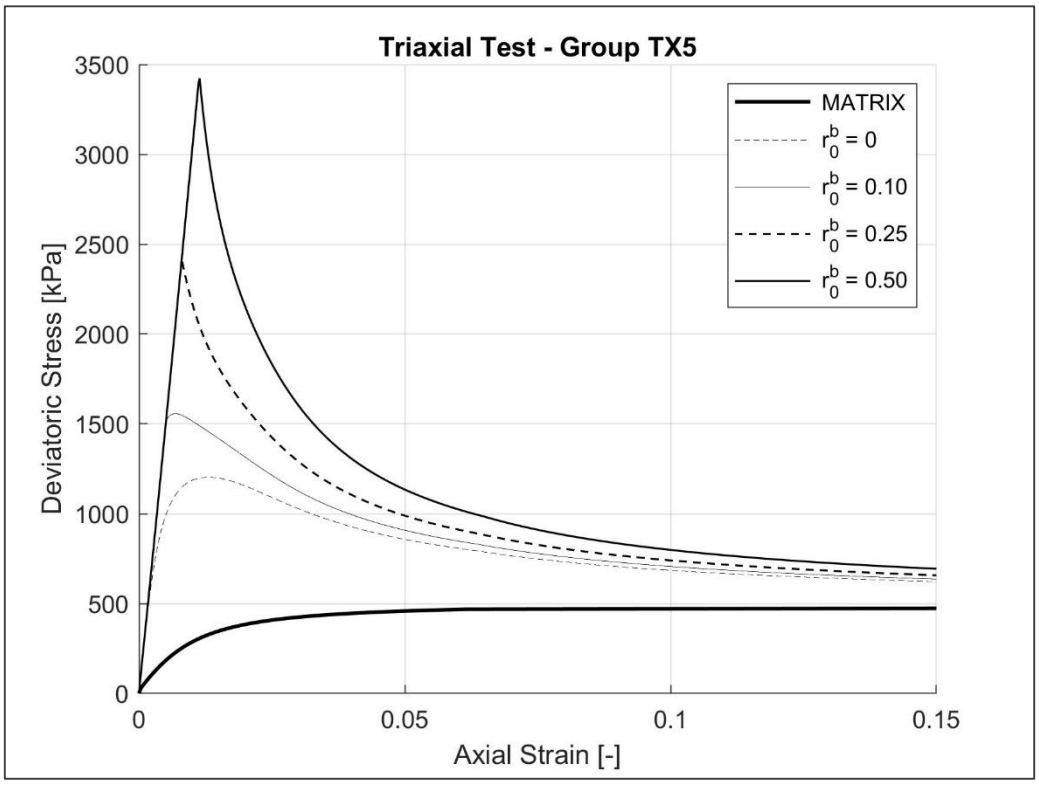

Figure 3.15: Triaxial tests of group TX5

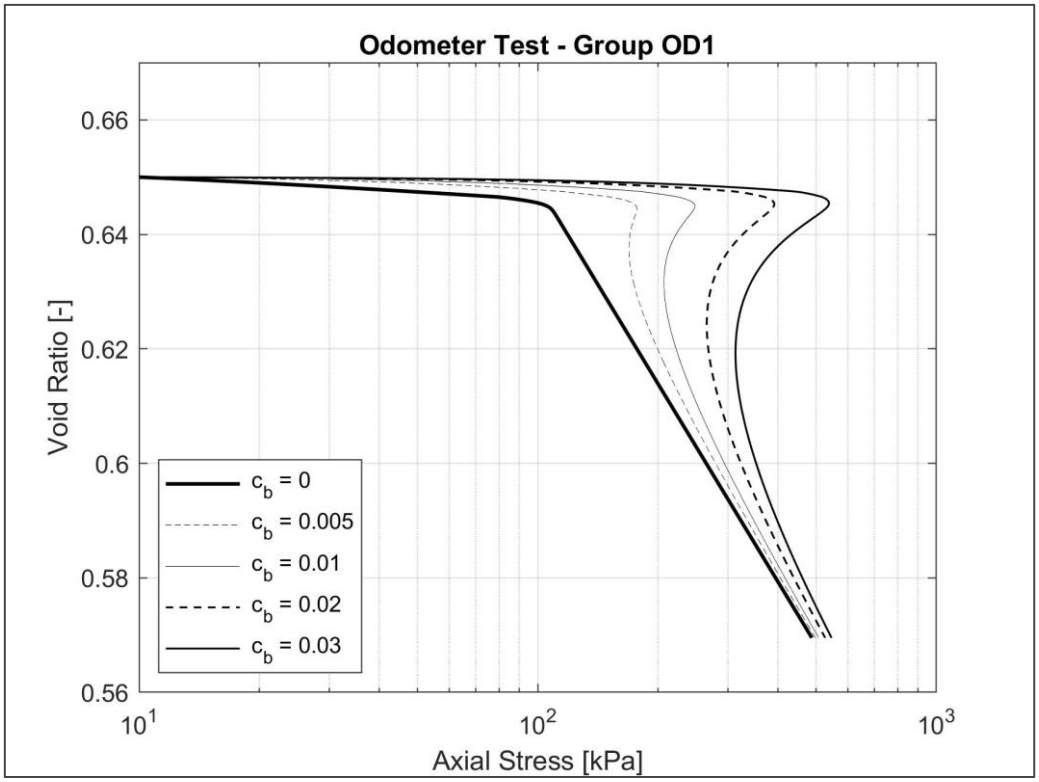

Figure 3.16: Oedometer tests of Group OD1

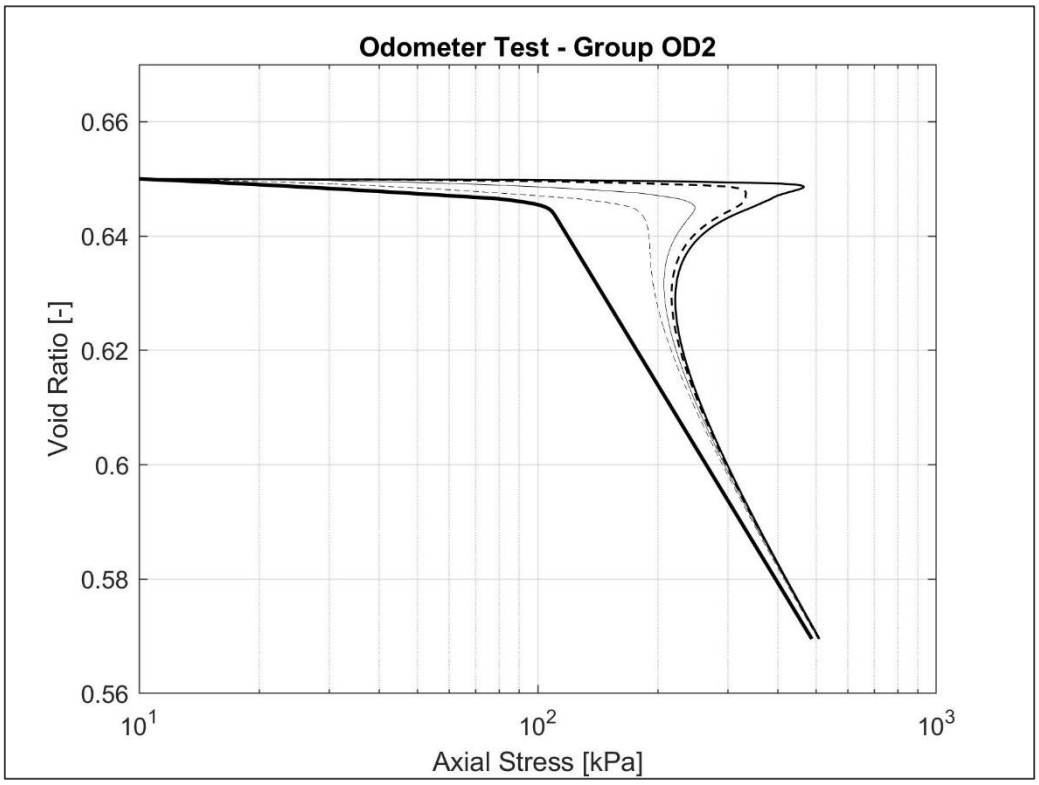

Figure 3.17: Oedometer tests of Group OD2

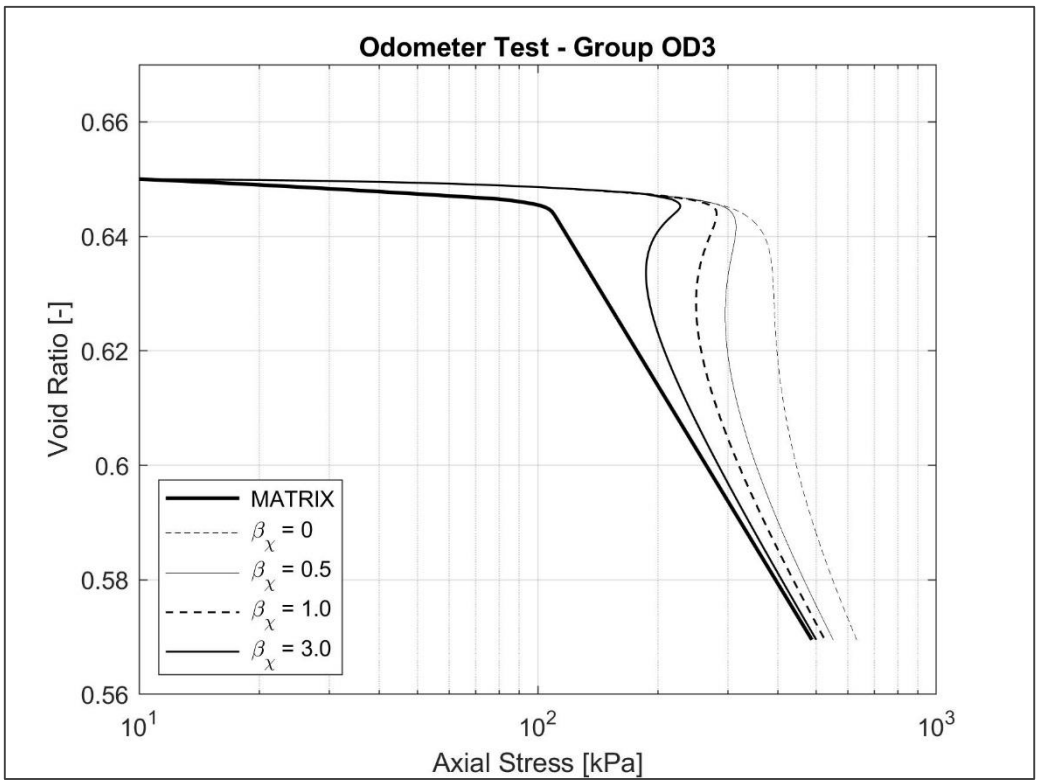

Figure 3.18: Oedometer tests of Group OD3

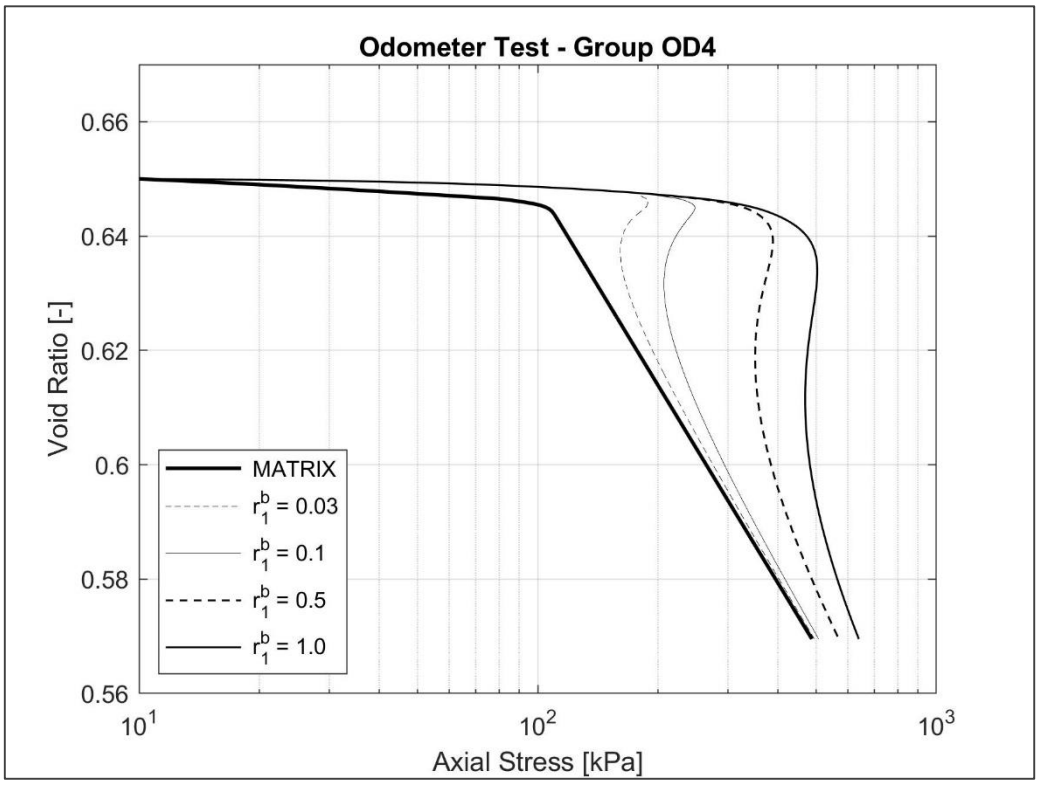

Figure 3.19: Oedometer tests of Group OD4

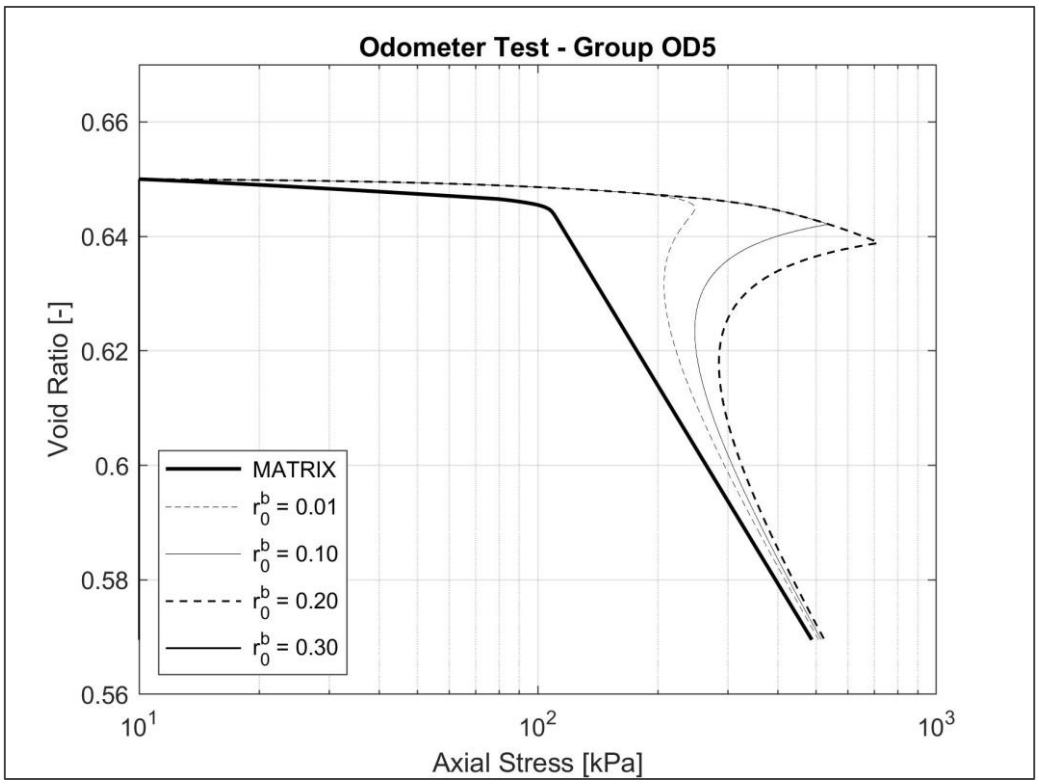

Figure 3.20: Oedometer tests of Group OD5

To illustrate the material behaviour under unloading-reloading cycles, response of simulated unloading-reloading triaxial cycles test is plotted in Fig. 3.21 for $r_0^b = 0.1\,MPa$, $r_1^b = 0.1\,MPa$, $c_b = 0.03$, $\chi_o = 1$, and $\beta_\chi = 1$. The red line indicates the initial value of the stiffness of the composite material. It can be observed that in the unloading-reloading cycle the stiffness has decreases considerably due to the degrading process of bond material and destructuring of the composite material.

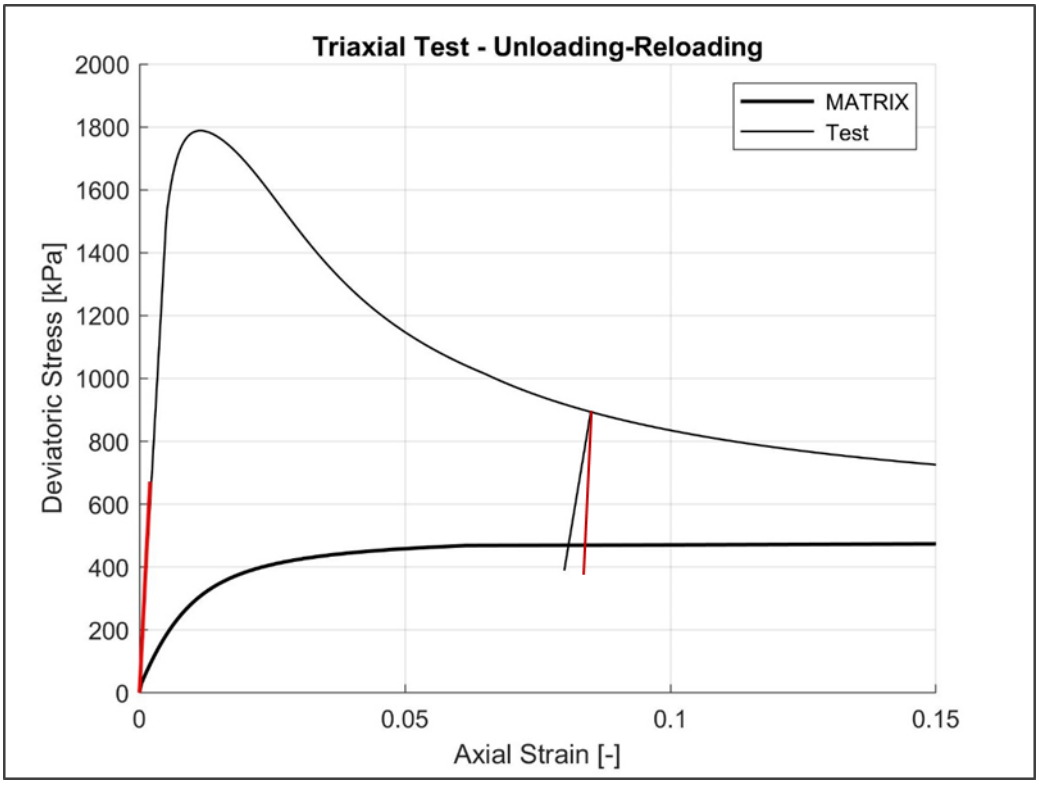

Figure 3.21: Triaxial test - Unloading-reloading cycles

Chapter 4

Modelling some reported test

Comparing experimental results with prediction carried out with numerical simulation is a fundamental procedure to validate mathematical models. It is also a technique that allows to identify the lacks of the model and the possible alternatives to improve its performance.

Two kind of tests are simulated and compared with reported results in this validation procedure: isotropic compression and conventional triaxial tests. Triaxial tests reported by *Clough et al. (1981)* for artificially cemented samples are first simulated, using Mohr Coulomb Model to reproduce the sand matrix behaviour. Then, isotropic compression tests reported by *Rotta et al. (2003)*, and triaxial tests reported by *Dalla Rosa (2008)* using the same soil, are reproduced implementing the Modified Cam Clay Model for the matrix material.

4.1.- Drained triaxial tests by Clough et al. (1981)

Clough et al. (1981) tested samples of artificially cemented sands fabricated to simulate the natural soil behaviour. The samples were intentionally manufactured so as to be relatively weak, and were tested in triaxial compression to large strain. They were prepared mixing Type II Portland cement and a uniform sand at 8% moisture content. Two percent and four percent cement by weight of sample were used. After the mixture was compacted into the mold by layers with uniform density, the samples were stored in a humid room to cure for 14 days before testing.

Results reported by Clough et al. (1981) for triaxial test carried out for specimens with 2% and 4% of cement content and at a confining pressure of 103 kPa are compared with simulations The authors suggested that, in these cases, due to the low confining pressure, cementation is far more significant than the frictional component of strength, and because of the brittle failure of the cementation bonds, the sand itself exhibits brittle failure.

For simulations, the first step was to calibrate the model in order to reproduce the uncemented sand behaviour. In this case, the matrix material was modeled through Mohr Coulomb Model and the parameters obtained after the calibration procedure are shown in Tab. 4.1. Values for the elastic parameters related to the cementitious agent are not easy to deduce, since no tests carried out using only bonding material are reported and in fact, this kind of test are practically impossible to perform. Instead, in order to proceed with the validation, typical values of a lean concrete were adopted (Tab. 4.2).

The other parameters, obtained after calibration on tested cemented sands are presented in Tab 4.3. Label “TX(a)-b” means triaxial test for the specimen with “a” percent cement content and confining pressure equal to “b”. The linear damage evolution law was considered in this case.

Parameter	Value
E^M $[MPa]$	70
ν^M $[-]$	0.20
c'^M $[kPa]$	0
φ'^M $[°]$	35

Table 4.1: Matrix parameters for triaxial test simulations - Mohr-Coulomb Model[2]

Parameter	Value
E^b $[MPa]$	8000
ν^b $[-]$	0.20

Table 4.2: Elastic parameters for bond material

Parameter	TX(2)-103	TX(4)-103
r_0^b $[MPa]$	0.01	0.07
r_1^b $[MPa]$	0.40	0.40
c_b $[-]$	0.011	0.022
χ_o $[-]$	0.90	0.80
β_χ $[-]$	2.30	3.00

Table 4.3: Parameters for triaxial test simulations (linear damage evolution law)

In Tab. 4.3, c_b corresponds to cement concentration in terms of volume as defined in Chapter 3. From the relation established in Eq. 3.4 it can be directly related with the cement content in terms of dry weight, as it is defined and reported by the authors. Since it is the same soil with different cement contents, it was expected that the values of the initial structuration parameter χ_o and the destructuring rate parameter β_χ obtained after calibration were the same for both tests. But some differences were found for the values of χ_o and β_χ. The possible variables affecting these two parameters will be discussed later.

[2] A linear isotropic hardening law was considered in order to smooth the quasi perfect elasto-plastic stress-strain curve for the matrix material.

Responses obtained for the simulated tests are shown in Fig. 4.1. For the uncemented sand, good accuracy is reached through Mohr Coulomb model. For the cemented sands the accuracy is also good for the elastic response (i.e. the first part of the stress-strain curves) meaning that the initial structuration parameter is well determined. For the response after peak, the accuracy is acceptable but the results show that the model tends to give a more brittle behavior than the experiment.

In Fig. 4.1 is also presented the evolution of the structuration parameter, normalized by the initial one. After peak, a quick destructuration is observed, and the stress-strain curve of cemented material converge to the one of the uncemented sand.

It is known that Mohr Coulomb Model has several limitations to reproduce the soils behaviour, especially the volumetric response, since constant rate of dilation is predicted with this model. For this reason, no volumetric strain evolution for the simulated tests are shown in this part of the validation. Despite of this, it can be said that the composite model exhibits a good performance in terms of axial strain - deviatoric stress.

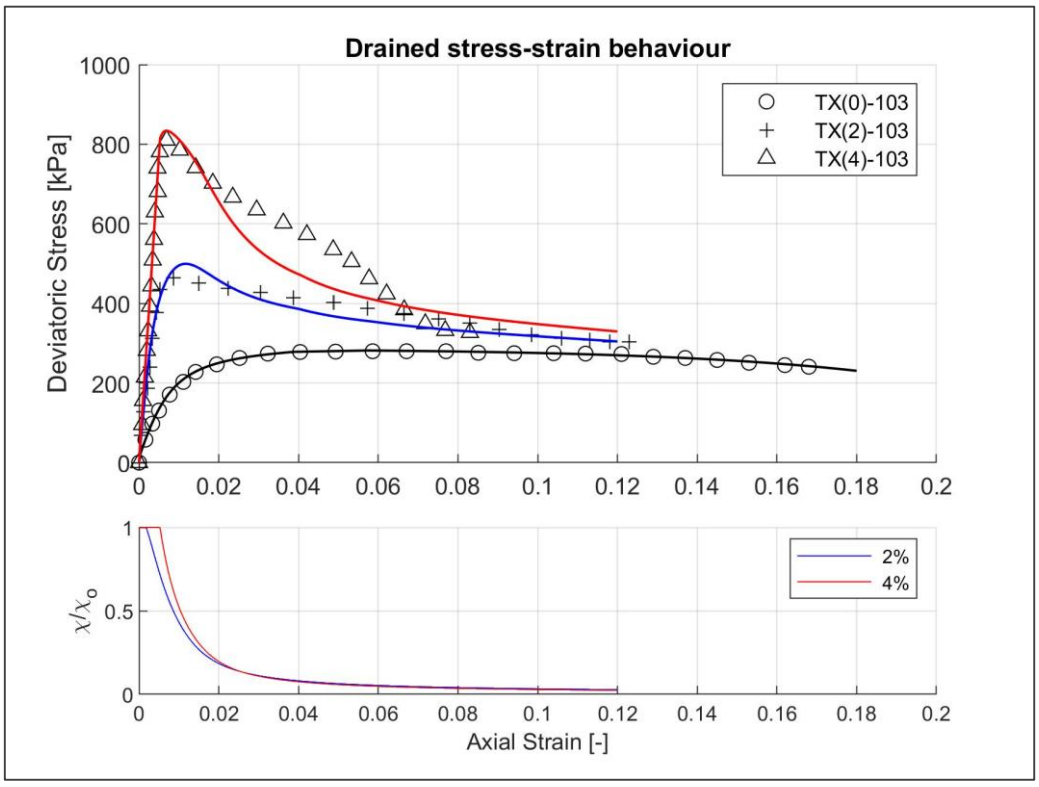

Figure 4.1: Triaxial tests reported by Clough et al. (1981) and simulations performed

4.2.- Isotropic compression tests by Rotta et al. (2003)

Rotta et al. (2003) intended to simulate the formation of a cemented sedimentary deposit in which cement bonding occurs after burial and under geostatic stresses. The soil samples used derived from weathered sandstone obtained from the region of Porto Alegre, in southern Brazil.

The specimens were prepared by initially mixing dry soil and Portland cement considering 1%, 2%, and 3% of cement content. Water was then added and further mixing was performed. After compaction in the mold at a target void ratio of 0.65 the samples were placed in the triaxial cell and submitted, prior the onset of the cementitious bond, to confining pressures ranging from 50 to 2000 kPa (intended to represent soil elements at different depths in the fictitious sedimentary deposit when the cementing occurred). Then the specimens were cured for 48 h at constant confining stress. The authors indicated that the time taken to prepare and set up the specimen in the triaxial cell was always less than 1 h, which is much shorter than the time of Portland cement curing. Isotropic compression was then carried out.

Some results reported by Rotta et al. (2003) are shown in Chapter 1, in Fig. 1.21. They found an interactive effect of the curing void ratio and the cement content on the general behaviour of the soil. After yield, all the paths follow a post-yield compression line that is unique for each degree of cementation and which converges towards the intrinsic compression line of the uncemented soil as the isotropic stress increases.

In this case, sand matrix was modeled through Modified Cam Clay Model (MCCM). The parameters obtained after calibration for the uncemented sand are presented in Tab. 4.4. Elastic parameter for bonding material were considered equal in each simulated test for the cemented sand and are presented in Tab. 4.5.

The remaining parameters were assessed separately for each test. They are presented in Tab. 4.6. Label “ISO(a)b-c”, as defined by Rotta et al. (2003), means isotropic compression test for the specimen with “a” percent cement content cured at a confining stress close to “b” and compressed up to a stress equal to “c”. The damage evolution law considered in this case was the exponential dependency.

Tab. 4.6 provides the values of the confining stress and void ratio at the time of curing p'_{cur} and e_{cur}. Note that the samples were cured at stress states on the isotropic normal compression line for the uncemented soil. Therefore, each pair of values of p'_{cur} and e_{cur} correspond to a point situated at (or close to) this line.

Parameter	Value
κ^M $[-]$	0.0015
ν^M $[-]$	0.30
λ^M $[MPa]$	0.069
M^M[-]	1.25

Table 4.4: Matrix parameters for isotropic compression test simulations (MCCM)

Parameter	Value
E^b $[MPa]$	8000
ν^b $[-]$	0.30

Table 4.5: Elastic parameters for bond material

Test	p'_{cur}	e_{cur}	r_0^b	r_1^b	c_b	χ_o	β_χ
	$[kPa]$	$[-]$	$[MPa]$	$[-]$	$[-]$	$[-]$	$[-]$
ISO(1)100-6000	98	0.62	0.001	30	0.006	0.8	0.6
ISO(1)250-6000	246	0.57	0.001	30	0.006	1.5	2.6
ISO(1)500-6000	499	0.53	0.001	30	0.006	2.5	4.3
ISO(1)1000-6000	998	0.47	0.001	30	0.006	5.0	5.5
ISO(2)100-6000	104	0.62	0.001	30	0.011	0.8	0.9
ISO(2)250-6000	254	0.57	0.001	30	0.011	1.5	2.8
ISO(2)500-6000	494	0.54	0.001	30	0.011	2.5	4.3
ISO(3)100-6000	99	0.62	0.001	30	0.017	0.8	1.2
ISO(3)250-6000	245	0.57	0.001	30	0.017	1.6	3.2
ISO(3)500-6000	492	0.54	0.001	30	0.017	2.5	4.5
ISO(3)1000-6000	974	0.48	0.001	30	0.017	4.2	5.8

Table 4.6: Parameters for isotropic compression test simulations (exponential damage evolution law)

As one can observe from Tab 4.6, relative high values of damage evolution rate r_1^b were obtained after calibration in comparison with the simulated triaxial tests previously presented. Actually, the damage evolution law used is different (linear in the simulated triaxial tests and exponential in this case). This means that the way and velocity at which damage (i.e. fissures) develop in bonds is substantially different for isotropic and shearing loading. For the tests under comparison, it appears that isotropic compression results in a slower damage rate than shearing.

On the other hand, the values obtained for χ_o and β_χ are of the same order of magnitude in the isotropic and shear tests. Nevertheless, differences exist from test to test. It is suggested that these two parameters could be dependent on the curing conditions. This aspect will be discussed in next section.

Responses obtained for the simulated tests are shown in Fig. 4.2, Fig 4.3 and Fig. 4.4 for the specimens of 1%, 2% and 3% of cement content respectively. For the uncemented sand, MCCM appears to well-capture the test. For the cemented sands, the agreement is good for all curing stresses and cement contents, but the model predicts a slightly faster degradation towards the uncemented compression line.

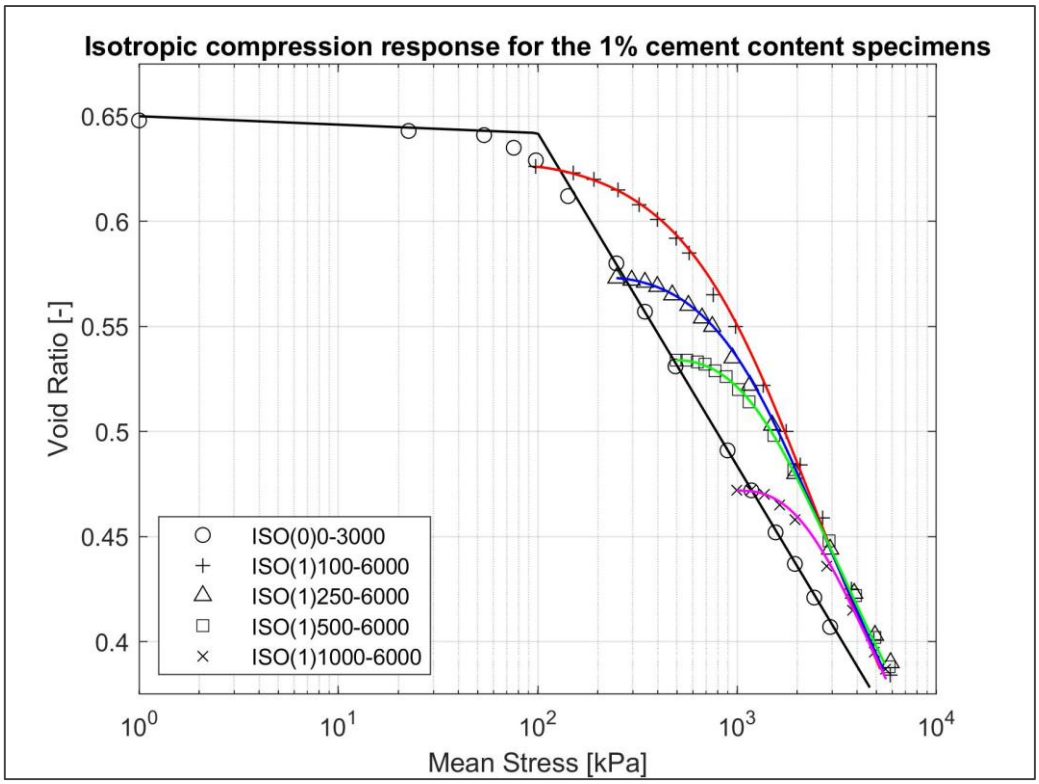

Figure 4.2: Isotropic compression tests reported by Rotta et al. (2003) and simulations performed - specimens with 1% cement content

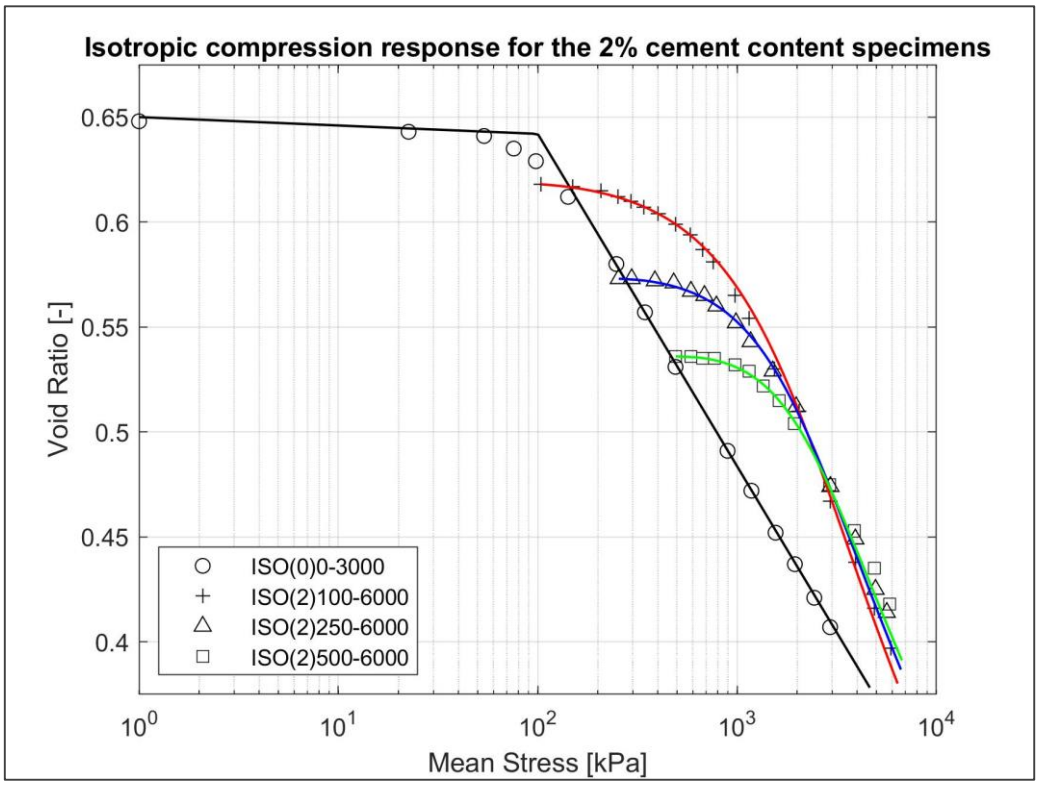

Figure 4.3: Isotropic compression tests reported by Rotta et al. (2003) and simulations performed - specimens with 2% cement content

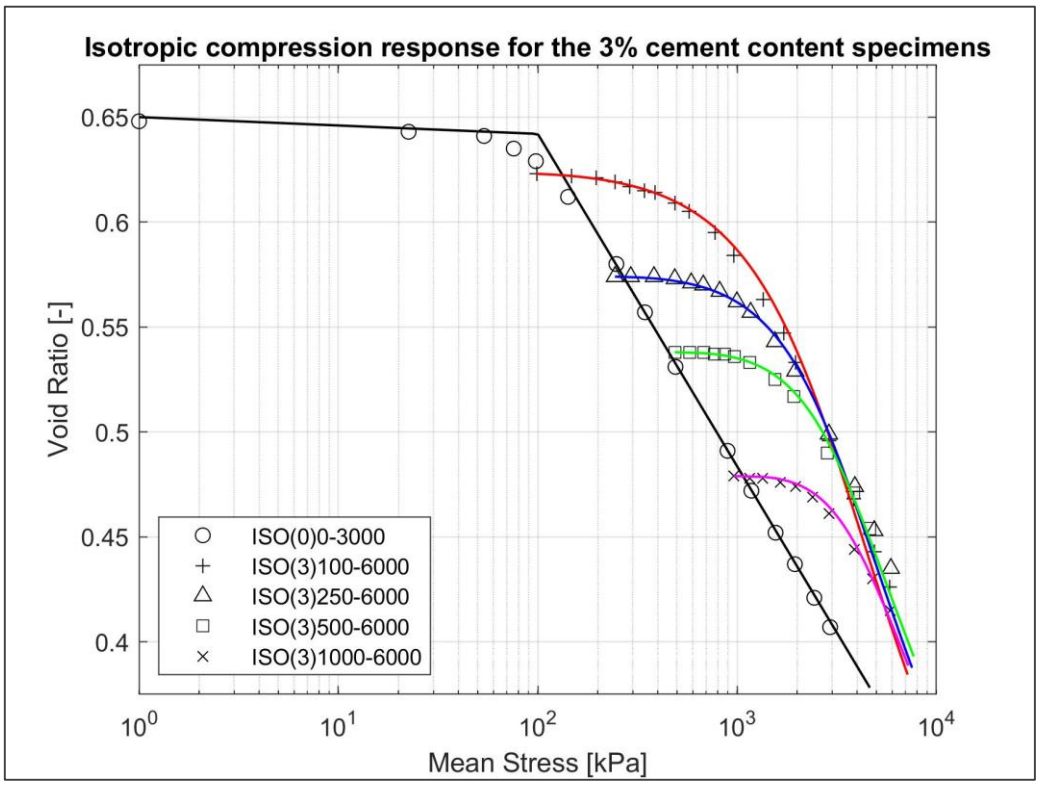

Figure 4.4: Isotropic compression tests reported by Rotta et al. (2003) and simulations performed - specimens with 3% cement content

4.3.- Drained triaxial tests by Dalla Rosa et al. (2008)

Dalla Rosa et al. (2008) extend the work made by Rotta et al. (2003) to triaxial shear tests. Samples preparation is similar to that described previously, using the same cement contents. The samples were installed in the triaxial chamber immediately after preparation and were left to cure 48 h under different confining pressures. Standard drained tests were carried out, at confining pressures either equal to or different from the curing stress.

In this section, only two tests are simulated and compared with the results reported by Dalla Rosa et al. (2008). They correspond to specimens with 2% cement content cured at 250 and 500 kPa, and tested at the same confining pressure as curing.

Since the specimens were done with the same sand and following the same procedure than the tests reported by Rotta et al. (2003), the same parameters for the matrix material (Tab. 4.4) and the same elastic parameters for the bonding material (Tab. 4.5) were considered. The remaining parameters, obtained after calibration, are presented in Tab 4.7.

Test	p'_{cur}	e_{cur}	r_0^b	r_1^b	c_b	χ_o	β_χ
	$[kPa]$	$[-]$	$[MPa]$	$[MPa]$	$[-]$	$[-]$	$[-]$
TX(2)-250	250	0.574	0	6	0.011	1.0	2.8
TX(2)-500	500	0.537	0	15	0.011	1.2	4.3

Table 4.7: Parameters for triaxial test simulations (linear damage evolution law)

Since samples were cured at similar stresses and void ratios than that considered by Rotta et al. (2003), it was expected that the parameters obtained in the calibration presented previously would also work with these triaxial tests simulations (parameters in Tab. 4.6 - rows corresponding to 2% cement content and 250 and 500 kPa of curing test). However, one can see from Tab, 4.7 that different values for χ_o were obtained after calibration in both simulated tests, while the values of β_χ remained equal. Also the damage rule considered was not the same. As the triaxial tests simulated for the case of Clough et al. (1981) at the beginning of this chapter, linear damage evolution law is better to reach certain accuracy in this case. Because different damage evolution laws were considered, no comparisons are possible between the values of r_1^b obtained now and the obtained in the isotropic compression test simulations.

Responses obtained for the simulated tests are shown in Fig. 4.5 and Fig 4.6 for the specimens cured and tested at confining pressures of 250 and 500 kPa respectively. In this figures one can see the stress-strain response and the volumetric strain evolution during test. The accuracy achieved for the uncemented sand through MCCM is acceptable, except for the volumetric response of the specimen tested at a confining pressure of 250 kPa.

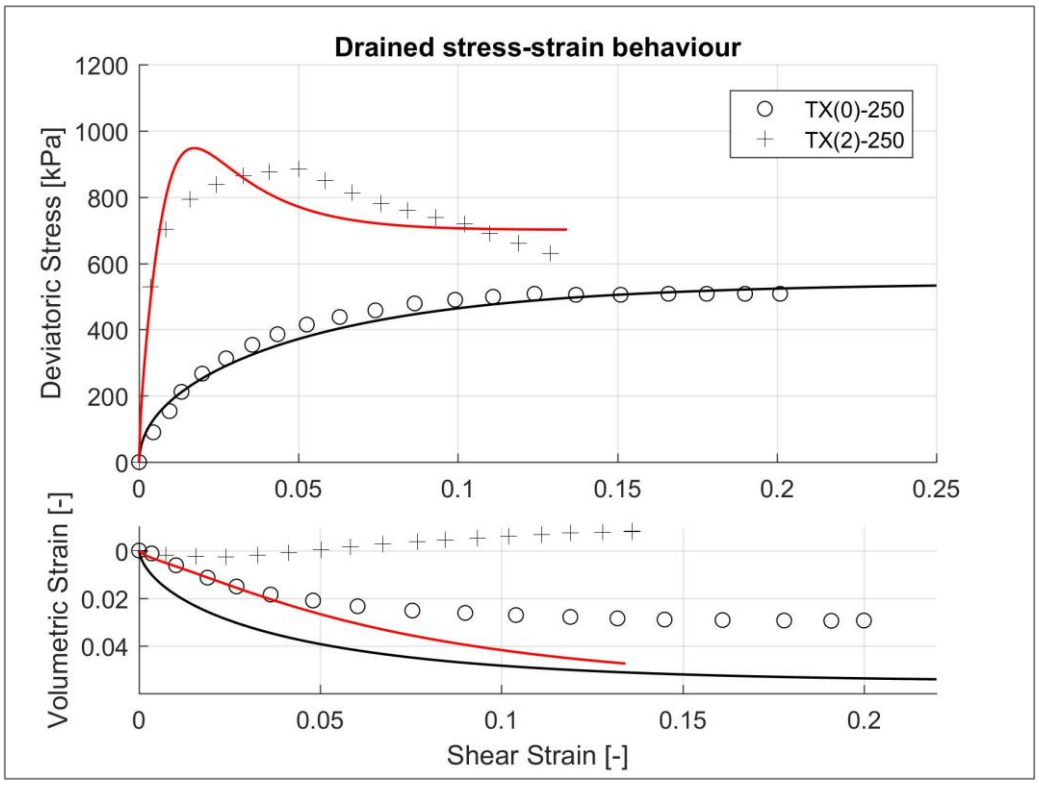

Figure 4.5: Triaxial test reported by Dalla Rosa et al. (2008) and simulation performed - 2% cement content and 250 kPa of confining pressure

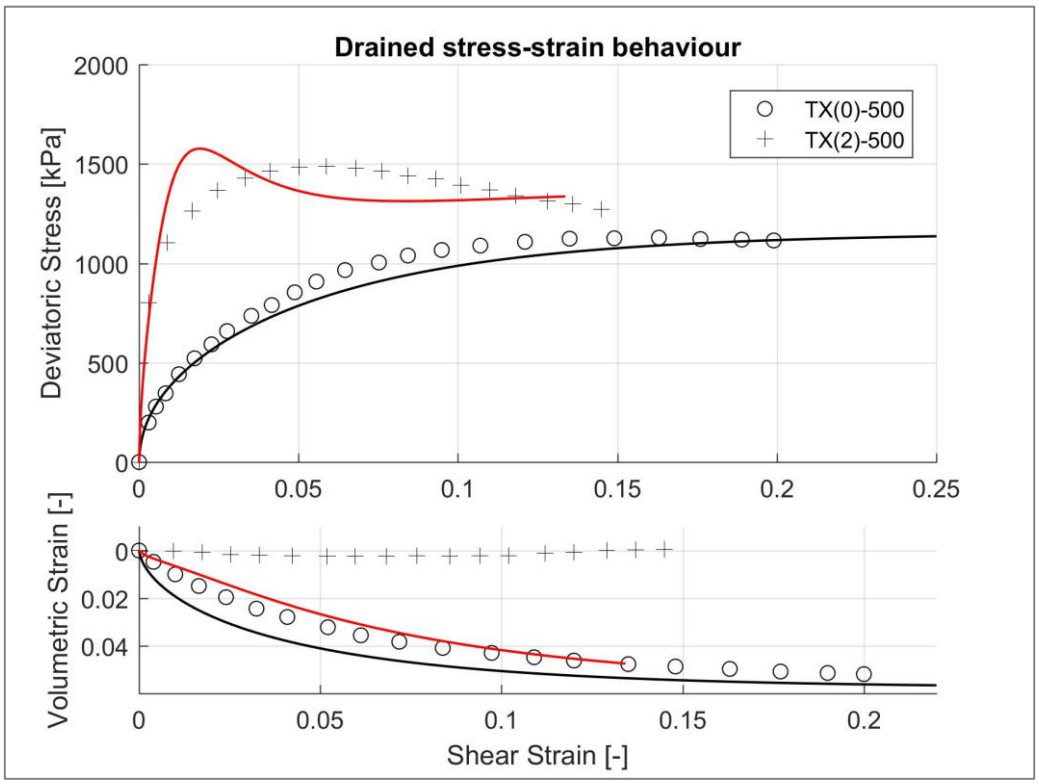

Figure 4.6: Triaxial test reported by Dalla Rosa et al. (2008) and simulation performed - 2% cement content and 500 kPa of confining pressure

For the cemented sands, the agreement between model and experiments is relatively poor, especially for the volumetric response, since the increase in dilatancy with cementation is not reproduced by the model. Peak strength is slightly overestimated by simulations, and the strain at peak predicted is lower than the reported test. In general, the behaviour after peak predicted by simulation is more brittle than that observed in the real tests.

4.4.- Discussion

From observations, one can see that the definition of the damage evolution law is quite different for the triaxial tests and isotropic tests, even for the tests performed with the same soil. As suggested before, this means that damage in bond, and therefore destructuration, do not develop in the same way and with similar rates in each kind of test. It is suggested that this is probably related to an intrinsic strength anisotropy of the bond material that is not taken into account through the actual damage model. This evolution law defines almost all the behaviour after peak strength, which is the most visible lack of the model.

It was proposed in the previous section that a relation between the initial structuration parameter and the curing conditions appears to exist. In order to inquire in this aspect, values of χ_o obtained for isotropic compression tests (Tab 4.6), are plotted in relation with curing void ratio (see Fig. 4.7). Visible tendency is observed and a possible exponential dependency is proposed.

From Fig. 4.7, one can deduce that the lower the curing void ratio is, the more structured the specimens is when the test begins. This can be related to the fact that, as was described for many authors from their observations, an increase in density results in an increase in the number of contact points between the soil particles where the cement can form a bond, and therefore the bonded structure is more “effective”.

Same analysis can be considered for the destructuration rate. If values of β_χ are plotted in relation with the curing void ratio a visible tendency is observed too. In this case, a linear dependecy is proposed (see Fig. 4.8). It can be observed that the lower the curing void ratio is, the higher the rates of destructuration are. This tendency can not easily be explained from a physical point of view.

The increase of β_χ can be related, instead, to the increase of initial structuration parameter itself. It is reasonable to suppose that at higher level of initial structuration, higher rates of destructuration would occur when the specimen is loaded. This is shown in Fig. 4.9. A tendency is observed and a logarithmic dependency is proposed.

These observations suggest that the structuration parameter must be related not only to the damage of bonding material, but also with a variable representative of the state of the matrix material. This variable could be for example the void ratio itself (or sand density), the accumulated plastic strains, or the plastic multiplier. χ_o would be, in each case, a value representative of the structuration in the reference undamaged state.

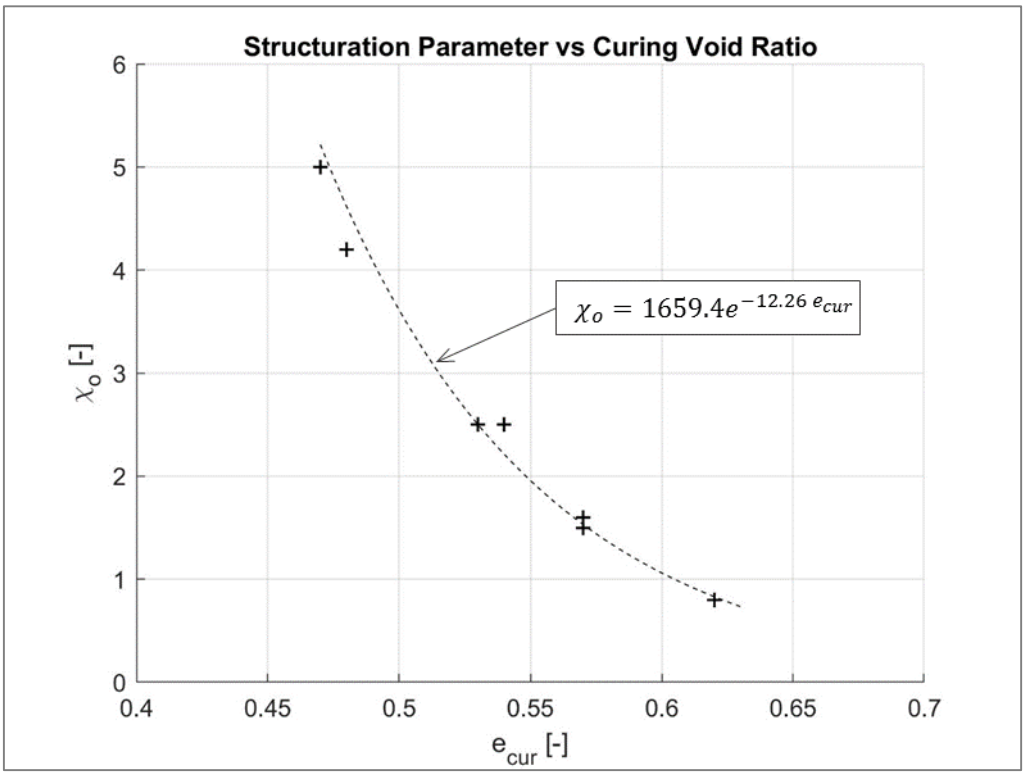

Figure 4.7: Relation between the initial structuration parameter and the curing void ratio

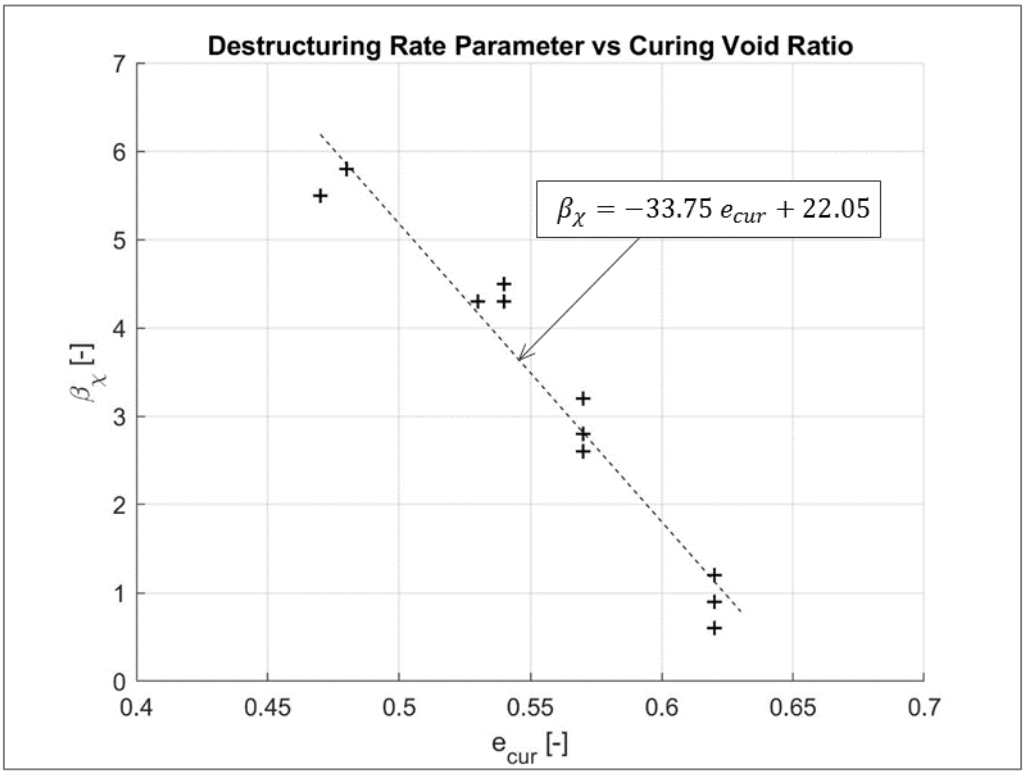

Figure 4.8: Relation between the destructuration rate and the curing void ratio

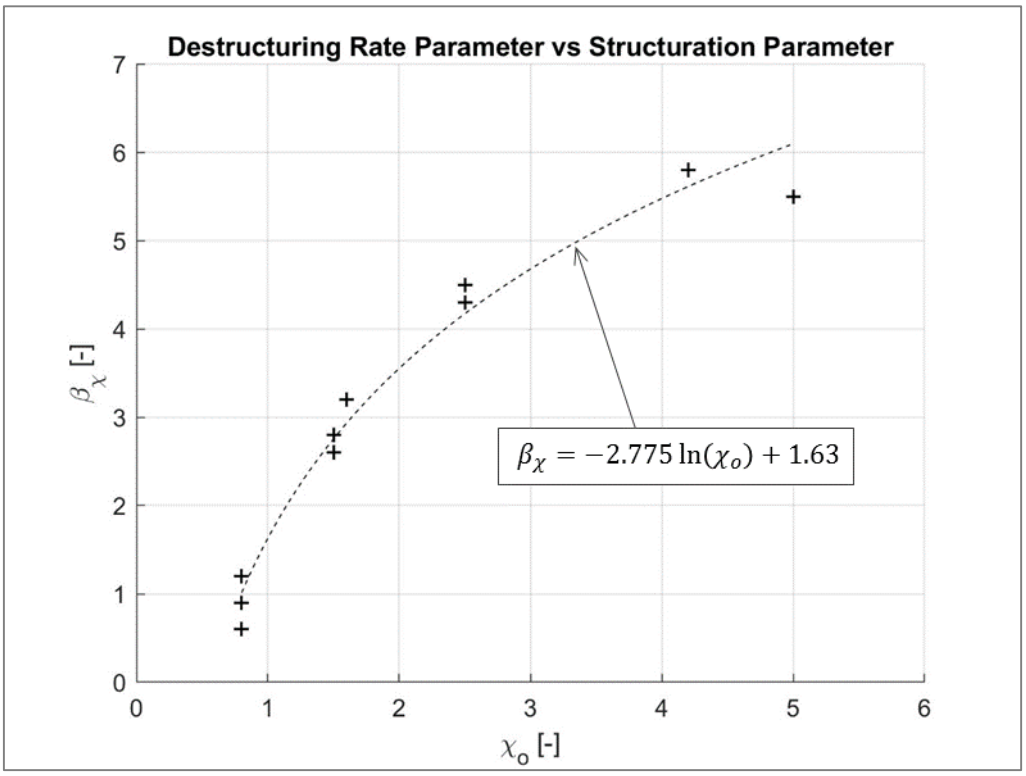

Figure 4.9: Relation between the destructuration rate and the initial structuration parameter

Chapter 5

Conclusions and future work

After a thorough review of the available bibliography, main aspects of the behaviour of cemented sands were highlighted. In general, the behaviour of this kind of material is strongly influenced by the cement content and sand density at time of curing. In addition, the confining pressure at which the test is performed plays an important role, controlling the relative contributions to the sand response by the cementation and frictional components: the lower the confining pressure, the more significant the cementation component is. Frictional component is related to more ductile behaviour, while the cementation component due to bonding particle is related to more brittle failure mode. Other effects of cementation in sands found in bibliography are adding a cohesion and tensile strength, increasing the unconfined compressive strength and increasing the stiffness and the elastic range domain.

A coupled damage-elastoplastic model based on a composite material was developed. It was intended to represent the behaviour of the two key materials of the cemented sands: the sand itself, and the cementing agent bonding the sand particles. Through the simulation of oedometer and conventional triaxial tests, it was shown that the model is able to reproduce the main effects of cementation in sands, like increase in stiffness, increase of strength and the more brittle failure mode of compared with uncemented soils.

A validation procedure was carried out by comparison of reported experimental results with the response predicted by the model. For the case of isotropic compression tests, the agreement achieved is good. The increase in stiffness is well captured by the model by calibrating the initial structuration parameter. The destructuration when loaded is simulated with acceptable accuracy but the model predicts a faster degradation towards the uncemented compression line.

For the triaxial response, the agreement achieved is poorer, particularly for the volumetric response. The peak strength is relatively well-predicted but the predicted strain at peak is in general lower than in the experiments. The post-failure part of the model is the most critical: in general the behaviour after peak predicted by simulation is more brittle than that observed in the real tests, and the transition from brittle to ductile failure mode is not well-captured by the model when confining stress is increased. Finally, the increase in dilatancy with cement content is not reproduced by the model.

Further improvements in the damage evolution law and the damage model itself for the bonding material are necessary to represent the after peak behaviour with more accuracy. It was found that damage in bonds do not develop in the same way for isotropic load and shearing load, and it is suggested that this is probably related to the strength

anisotropy of cementitious materials. A damage model including this aspect should be considered.

Finally, a relationship between the effectiveness of microstructure, represented by the structuration parameter and the void ratio at the time of curing was found. This is in agreement with the observation of many investigators that suggested that an increase in density at time of bond deposition results in more structured sands, due to the increase in the number of contacts between soil particles where the cement can form a bond. It is suggested then, that a dependency of the structuration parameter with a variable representative of the state of the uncemented material at the time of curing should be included in the model in further developments.

References

Acar, Y., and El-Tahir, A. (1986). Low strain dynamic properties of artificially cemented sand. *Journal of the Geotechnical Engineering Division, ASCE*, 112(11):1001–1015.

Airey, D. W. & Fahey, M. (1991). Cyclic response of calcareous soil from the North-West Shelf of Australia. *Géotechnique*, 41(1):101–121.

Airey, D. W. (1993). Triaxial testing of naturally cemented carbonate soil. *Journal of the Geotechnical Engineering Division, ASCE*, 119(9):1379–1398.

Burland, J. B. (1990). On the compressibility and shear strength of natural clays. *Géotechnique*, 40(3):329–378.

Carol, I., Rizzi, E. & Willam, K. (2001). On the formulation of anisotropic elastic degradation. I. Theory based on a pseudologarithmic damage tensor rate. *Int. J. Solids and Structures.,* 38(4):491–518.

Carol, I., Rizzi, E. & Willam, K. (1994). A unified theory of elastic degradation and damage based on a loading surface. *Int. J. Solids and Structures.,* 31(20):2835–1994.

Chang, T., and Woods, R. D. (1992). Effect of particle contact bond on shear modulus. *Journal of the Geotechnical Engineering Division, ASCE*, 118(8):1216–1233.

Chiang, Y. C. & Chae, Y. S. (1972). Dynamic properties of cement treated soils. *Highway Res. Record.* 379: 39–51.

Clough, G. W., Sitar, N., Bachus, R. C. & Rad, N. S. (1981). Cemented sands under static loading. *Journal of the Geotechnical Engineering Division, ASCE*, 107(6):799–817.

Consoli, N. C., Rotta, G. V. & Prietto, P. D. M. (2000). The influence of curing under stress on the triaxial response of cemented soils. *Géotechnique*, 50(1):99–105.

Consoli, N. C., Rotta, G. V. & Prietto, P. D. M. (2006). Yielding-compressibility-strength relationship for an artificially cemented soil cured under stress. *Géotechnique*, 56(1):69–72.

Coop, M. R. (1990). The mechanics of uncemented carbonate sands. *Géotechnique*, 40(4):607–626.

Coop, M. R. & Atkinson, J. H. (1993). The mechanics of cemented carbonate sands. *Géotechnique*, 43(1):53–67.

Cuccovillo, T. & Coop, M. R. (1993). The influence of bond strength on the mechanics of carbonate soft rocks. *Proceedings of the international conference on hard soils – soft rocks*, volume 1, pages 447–455. Athens. Rotterdam: Balkema.

Cuccovillo, T. & Coop, M. R. (1997). Yielding and pre-failure deformation of structured sands. *Géotechnique*, 47(3):481–508.

Cuccovillo, T. & Coop, M. R. (1999). On the mechanics of structured sands. *Géotechnique*, 49(6):741–760.

Dalla Rosa, F., Consoli, N. C. & Baudet, B. A. (2008). An experimental investigation of the behaviour of artificial soil cured under stress. *Géotechnique*, 58(8):675–679.

Dupas, J. M. & Pecker, A. (1979). Static and dynamic properties of sand-cement. *Journal of the Geotechnical Engineering Division, ASCE*, 105(3):419–436.

Gens, A. & Nova, R. (1993). Conceptual bases for a constitutive model for bonded soil and weak rocks. *Proceedings of the international conference on hard soils – soft rocks*, volume 1, pages 485–494. Athens. Rotterdam: Balkema.

Gens, A., Vaunat, J., Garitte, B. & Wileveau, Y. (2007). In situ behaviour of a stiff layered clay subject to thermal loading: observations and interpretation. *Géotechnique*, 57(2):207–228.

Lagioia, R. & Nova, R. (1995). An experimental and theoretical study of the behaviour of a calcarenite in triaxial compression. *Géotechnique*, 45(4):633–648.

Leroueil, S. & Vaughan, P. R. (1990). The general and congruent effects of structure in natural soils and weak rocks. *Géotechnique*, 40(3):467–488.

Mitchell, J. K. (1976). The Properties of Cement-Stabilized Soils. *Proceedings, Workshop on Materials and Methods for Low Cost Road, Rail and Reclamation Work*, Sept. 1976, Australia.

Olivella, S., Carrera, J., Gens, A. & Alonso, E. E. (1994). Non-isothermal multiphase flow of brine and gas thorugh saline media. *Transports in Porous Media*, 15(3):271–293.

Olivella, S., Gens, A., Carrera, J. & Alonso, E. E. (1996). Numerical formulation for a simulator (CODE_BRIGHT) for the coupled analysis of saline media. *Engineering Computations,* 13(7):87–112.

Pinyol, N., Vaunat, J. & Alonso, E. E. (2007). A constitutive model for soft clayey rocks that includes weathering effects. *Géotechnique*, 57(2):137–151.

Rotta, G. V., Consoli, N. C., Prietto, P. D. M., Coop, M. R. & Graham, J. (2003). Isotropic yielding in an artificially cemented soil cured under stress. *Géotechnique*, 53(5):493–501.

Vaunat, J., Cante, J. C., Ledesma, A. & Gens, A. (2000). *International Journal of Plasticity*, 16(2):121–141.

Vaunat, J. & Gens, A. (2003). Bond degradation and irreversible strains in soft argillaceous rock. *Proceedings, 12th Panamerican Conference on Soil Mechanics and Geotechnical Engineering,* Boston 1, pages 479–484.

Appendix A

Numerical implementation

The model developed was implemented in the Finite Element Code *Code_Bright* (*Olivella et al., 1994, 1996*) using a Stress Point Algorithm like the described by *Vaunat et al., (2000*) for an elastoplastic model for unsaturated soils.

The algorithm is based on an implicit integration scheme. A backward Euler method is assumed for the time discretization. The system of equations to be solved related to the matrix and bonding material are presented in Eq. A.1 and Eq. A.2. In addition, the yield conditions for plastic and damage loading indicated in Eq. A.3 must be satisfied.

$$\sigma_{ij}^{M\ n+1} = \sigma_{ij}^{M\ n} + \Delta\sigma_{ij}^{M\ n+1} \qquad and \qquad \sigma_{ij}^{b\ n+1} = \sigma_{ij}^{b\ n} + \Delta\sigma_{ij}^{b\ n+1} \qquad (Eq.A.1)$$

$$\chi^{p\ n+1} = \chi^{p\ n} + \Delta\chi^{p\ n+1} \qquad and \qquad \chi^{d\ n+1} = \chi^{d\ n} + \Delta\chi^{d\ n+1} \qquad (Eq.A.2)$$

$$F^{p\ n+1} = 0 \qquad and \qquad F^{d\ n+1} = 0 \qquad (Eq.A.3)$$

The unknown increment of matrix stress and the history variable of the elastoplastic model are defined in Eq. 2.2, Eq. 2.3 and Eq. 2.6. The discrete form of this equation for the step "$n+1$" are presented in Eq. A.4 and Eq. A.5.

$$\Delta\sigma_{ij}^{M\ n+1} = D_{ijkl}^{M}\left(\Delta\varepsilon_{kl}^{\ n+1} - m_{kl}^{p\ n+1}\,\Delta\lambda^{p\ n+1}\right) \qquad (Eq.A.4)$$

$$\Delta\chi^{p\ n+1} = h^{p\ n+1}\,\Delta\lambda^{p\ n+1} \qquad (Eq.A.5)$$

The residuals for the non-linear system to be solved for the elastoplastic model are defined in Eq. A.6 to Eq. A.8 for the increment step "$n+1$" and the iteration "it". The unknowns are $\Delta\sigma_{ij}^{M\ n+1}$, $\Delta\chi^{p\ n+1}$ and $\Delta\lambda^{p\ n+1}$.

$$res_{ij}^{\sigma M}\Big|_{it}^{n+1} = \Delta\sigma_{ij\ it}^{M\ n+1} - D_{ijkl}^{M}\left(\Delta\varepsilon_{kl}^{EXT\,n+1} - m_{kl\ it}^{p\ n+1}\,\Delta\lambda_{\ it}^{p\ n+1}\right) \qquad (Eq.A.6)$$

$$res^{\chi p}\Big|_{it}^{n+1} = \Delta\chi_{\ it}^{p\ n+1} - h_{\ it}^{p\ n+1}\,\Delta\lambda_{\ it}^{p\ n+1} \qquad (Eq.A.7)$$

$$res^{FP}\Big|_{it}^{n+1} = F_{\ it}^{p\ n+1} \qquad (Eq.A.8)$$

For its part, the discrete form for the step "$n+1$" of the unknown increment of bond stress and the history variable of the damage model are presented in Eq. A.9 and Eq. A.10. Note that they are quite different from the corresponding to the elastoplastic model. After some operation, Eq. A.11 and Eq. A.12 are obtained (only exponential damage law is considered here).

$$\Delta\sigma_{ij}^{b\,n+1} = D_{ijkl}^{b\quad n+1}\,\varepsilon_{kl}^{b\,n+1} - D_{ijkl}^{b\quad n}\,\varepsilon_{kl}^{b\,n} \qquad (Eq.A.9)$$

$$\Delta\chi^{d\,n+1} = \chi^{d\,n+1} - \chi^{d\,n} = r^{b\,n+1} - r^{b\,n} \qquad (Eq.A.10)$$

$$\Delta\sigma_{ij}^{b\,n+1} = \Delta\sigma_{ij}^{bT\,n+1} e^{-\Delta\lambda^{d\,n+1}}\mathcal{K}^{n+1} - \sigma_{ij}^{b\,n}\left(1 - e^{-\Delta\lambda^{d\,n+1}}\right) \qquad (Eq.A.11)$$

$$\Delta\chi^{d\,n+1} = r^{b\,n}\left(e^{r_1^b\,\Delta\lambda^{d\,n+1}} - 1\right) \qquad (Eq.A.12)$$

$$with \qquad \mathcal{K}^{n+1} = \frac{1 + c_b\chi^n}{e^{\beta_\chi\,\Delta\lambda^{d\,n+1}} + c_b\chi^n} \qquad (Eq.A.13)$$

$$and \qquad \Delta\sigma_{ij}^{bT\,n+1} = D_{ijkl}^{b\quad n}\,\frac{\chi^n}{1 + c_b\chi^n}\Delta\varepsilon_{kl}^{EXT\,n+1} \qquad (Eq.A.14)$$

The residuals for the non-linear system to be solved for the damage model are defined in Eq. A.15 to Eq. A.17 for the increment step "$n+1$" and the iteration "it". The unknowns are $\Delta\sigma_{ij}^{b\;n+1}$, $\Delta\chi^{d\;n+1}$ and $\Delta\lambda^{d\;n+1}$.

$$res_{ij}^{\sigma b}\Big|_{it}^{n+1} = \Delta\sigma_{ij\;it}^{b\;n+1} - \Delta\sigma_{ij}^{bT\,n+1} e^{-\Delta\lambda^{d}{}_{it}^{\,n+1}}\mathcal{K}_{it}^{n+1} + \sigma_{ij}^{b\,n}\left(1 - e^{-\Delta\lambda^{d}{}_{it}^{\,n+1}}\right) \qquad (Eq.A.15)$$

$$res^{\chi d}\Big|_{it}^{n+1} = \Delta\chi^{d}{}_{it}^{\;n+1} - r^{b\,n}\left(e^{r_1^b\,\Delta\lambda^{d}{}_{it}^{\,n+1}} - 1\right) \qquad (Eq.A.16)$$

$$res^{Fd}\Big|_{it}^{n+1} = F^{d}{}_{it}^{\;n+1} \qquad (Eq.A.17)$$

$$with \qquad \mathcal{K}_{it}^{n+1} = \frac{1 + c_b\chi^n}{e^{\beta_\chi\,\Delta\lambda^{d}{}_{it}^{\,n+1}} + c_b\chi^n} \qquad (Eq.A.18)$$

Solution of the system of equations is given by Eq. A.19 applied to all residuals defined previously, where res^{α} can be either $res_{ij}^{\sigma M}$, $res^{\chi p}$, or res^{FP} for the elastoplastic model and $res_{ij}^{\sigma b}$, $res^{\chi d}$, or res^{Fd} for the damage model. For its solution, the Newton's method is employed.

$$res^{\alpha}\Big|_{it+1}^{n+1} = res^{\alpha}\Big|_{it}^{n+1} + \left.\frac{\partial res^{\alpha}}{\partial\sigma_{kl}}\right|_{it}^{n+1}\Delta\sigma_{kl}\Big|_{it+1}^{n+1} + \left.\frac{\partial res^{\alpha}}{\partial\chi^{p}}\right|_{it}^{n+1}\Delta\chi^{p}\Big|_{it+1}^{n+1} + \cdots + \left.\frac{\partial res^{\alpha}}{\partial\lambda^{p}}\right|_{it}^{n+1}\Delta\lambda^{p}\Big|_{it+1}^{n+1} = 0 \qquad (Eq.A.19)$$

For the elastoplastic model, the expression of Eq. A.19 can be written in matrix form as indicated in Eq. A.20. The first matrix on the left hand-side of Eq. A.19 is a Jacobian matrix containing the partial derivatives of the equations with respect to each unknown. The terms of this Jacobian matrix are defined in Eq. A.21 to Eq. A.29. The second vector on the left hand-side is the vector with the unknowns. The vector on the right hand-side is the vector containing the residuals defined previously in Eq. A.6 to Eq. A.8.

$$\begin{bmatrix} \frac{\partial res_{ij}^{\sigma M}}{\partial \sigma_{kl}^{M}} & \frac{\partial res_{ij}^{\sigma M}}{\partial \chi^{p}} & \frac{\partial res_{ij}^{\sigma M}}{\partial \lambda^{p}} \\ \frac{\partial res^{\chi p}}{\partial \sigma_{kl}^{M}} & \frac{\partial res^{\chi p}}{\partial \chi^{p}} & \frac{\partial res^{\chi p}}{\partial \lambda^{p}} \\ \frac{\partial res^{Fp}}{\partial \sigma_{kl}^{M}} & \frac{\partial res^{Fp}}{\partial \chi^{p}} & \frac{\partial res^{Fp}}{\partial \lambda^{p}} \end{bmatrix}_{it}^{n+1} \begin{bmatrix} \Delta\sigma_{kl}^{M} \\ \Delta\chi^{p} \\ \Delta\lambda^{p} \end{bmatrix}_{it+1}^{n+1} = - \begin{bmatrix} res_{ij}^{\sigma M} \\ res^{\chi p} \\ res^{Fp} \end{bmatrix}_{it}^{n+1} \quad (Eq.A.20)$$

$$\left.\frac{\partial res_{ij}^{\sigma M}}{\partial \sigma_{kl}^{M}}\right|_{it}^{n+1} = \delta_{ik}\delta_{jl} + D_{ijmn}^{M} \left.\frac{\partial m_{mn}^{p}}{\partial \sigma_{kl}^{M}}\right|_{it}^{n+1} \Delta\lambda^{p}{}_{it}^{n+1} \quad (Eq.A.21)$$

$$\left.\frac{\partial res_{ij}^{\sigma M}}{\partial \chi^{p}}\right|_{it}^{n+1} = D_{ijkl}^{M} \left.\frac{\partial m_{kl}^{p}}{\partial \chi^{p}}\right|_{it}^{n+1} \Delta\lambda^{p}{}_{it}^{n+1} \quad (Eq.A.22)$$

$$\left.\frac{\partial res_{ij}^{\sigma M}}{\partial \lambda^{p}}\right|_{it}^{n+1} = D_{ijkl}^{M}\ m_{kl}^{p}{}_{it}^{n+1} \quad (Eq.A.23)$$

$$\left.\frac{\partial res^{\chi p}}{\partial \sigma_{kl}^{M}}\right|_{it}^{n+1} = - \left.\frac{\partial h^{p}}{\partial \sigma_{kl}^{M}}\right|_{it}^{n+1} \Delta\lambda^{p}{}_{it}^{n+1} \quad (Eq.A.24)$$

$$\left.\frac{\partial res^{\chi p}}{\partial \chi^{p}}\right|_{it}^{n+1} = 1 - \left.\frac{\partial h^{p}}{\partial \chi^{p}}\right|_{it}^{n+1} \Delta\lambda^{p}{}_{it}^{n+1} \quad (Eq.A.25)$$

$$\left.\frac{\partial res^{\chi p}}{\partial \lambda^{p}}\right|_{it}^{n+1} = - h^{p}{}_{it}^{n+1} \quad (Eq.A.26)$$

$$\left.\frac{\partial res^{Fp}}{\partial \sigma_{kl}^{M}}\right|_{it}^{n+1} = \left.\frac{\partial F^{p}}{\partial \sigma_{kl}^{M}}\right|_{it}^{n+1} \quad (Eq.A.27)$$

$$\left.\frac{\partial res^{Fp}}{\partial \chi^{p}}\right|_{it}^{n+1} = \left.\frac{\partial F^{p}}{\partial \chi^{p}}\right|_{it}^{n+1} \quad (Eq.A.28)$$

$$\left.\frac{\partial res^{Fp}}{\partial \lambda^{p}}\right|_{it}^{n+1} = \left.\frac{\partial F^{p}}{\partial \lambda^{p}}\right|_{it}^{n+1} \quad (Eq.A.29)$$

For the damage model, the expression of Eq. A.19 can be written in matrix form as indicated in Eq. A.30. The terms of the Jacobian matrix for this case are defined in Eq. A.31 to Eq. A.39. The vector on the right hand-side is the vector containing the residuals defined previously in Eq. A.15 to Eq. A.17.

$$\begin{bmatrix} \frac{\partial res_{ij}^{\sigma b}}{\partial \sigma_{kl}^{b}} & \frac{\partial res_{ij}^{\sigma b}}{\partial \chi^{d}} & \frac{\partial res_{ij}^{\sigma b}}{\partial \lambda^{d}} \\ \frac{\partial res^{\chi d}}{\partial \sigma_{kl}^{b}} & \frac{\partial res^{\chi d}}{\partial \chi^{d}} & \frac{\partial res^{\chi d}}{\partial \lambda^{d}} \\ \frac{\partial res^{Fd}}{\partial \sigma_{kl}^{b}} & \frac{\partial res^{Fd}}{\partial \chi^{d}} & \frac{\partial res^{Fd}}{\partial \lambda^{d}} \end{bmatrix}_{it}^{n+1} \begin{bmatrix} \Delta\sigma_{kl}^{b} \\ \Delta\chi^{d} \\ \Delta\lambda^{d} \end{bmatrix}_{it+1}^{n+1} = - \begin{bmatrix} res_{ij}^{\sigma b} \\ res^{\chi d} \\ res^{Fd} \end{bmatrix}_{it}^{n+1} \qquad (Eq.A.30)$$

$$\left.\frac{\partial res_{ij}^{\sigma b}}{\partial \sigma_{kl}^{b}}\right|_{it}^{n+1} = \delta_{ik}\delta_{jl} \qquad (Eq.A.31)$$

$$\left.\frac{\partial res_{ij}^{\sigma b}}{\partial \chi^{d}}\right|_{it}^{n+1} = 0 \qquad (Eq.A.32)$$

$$\left.\frac{\partial res_{ij}^{\sigma b}}{\partial \lambda^{d}}\right|_{it}^{n+1} = \Delta\sigma_{ij}^{bT\,n+1} e^{-\Delta\lambda^{d}{}_{it}^{n+1}} \left(\mathcal{K}_{it}^{n+1} - \left.\frac{\partial \mathcal{K}}{\partial \lambda^{d}}\right|_{it}^{n+1}\right) + \sigma_{ij}^{b\,n} e^{-\Delta\lambda^{d}{}_{it}^{n+1}} \qquad (Eq.A.33)$$

$$\left.\frac{\partial res^{\chi d}}{\partial \sigma_{kl}^{b}}\right|_{it}^{n+1} = 0 \qquad (Eq.A.34)$$

$$\left.\frac{\partial res^{\chi d}}{\partial \chi^{d}}\right|_{it}^{n+1} = 1 \qquad (Eq.A.35)$$

$$\left.\frac{\partial res^{\chi d}}{\partial \lambda^{d}}\right|_{it}^{n+1} = -r_1^{b}\, r^{b\,n}\, e^{r_1^{b}\,\Delta\lambda^{d}{}_{it}^{n+1}} \qquad (Eq.A.36)$$

$$\left.\frac{\partial res^{Fd}}{\partial \sigma_{kl}^{b}}\right|_{it}^{n+1} = \varepsilon_{kl}^{b\,n+1} \qquad (Eq.A.37)$$

$$\left.\frac{\partial res^{Fd}}{\partial \chi^{d}}\right|_{it}^{n+1} = -1 \qquad (Eq.A.38)$$

$$\left.\frac{\partial res^{Fd}}{\partial \lambda^{d}}\right|_{it}^{n+1} = u_{it}^{n+1} = \frac{1}{2}\varepsilon_{ij}^{b\,n+1}\,\sigma_{ij\,it}^{b\,n+1} \qquad (Eq.A.39)$$

$$with \qquad \left.\frac{\partial \mathcal{K}}{\partial \lambda^{d}}\right|_{it}^{n+1} = -\beta_{\chi} e^{\beta_{\chi}\,\Delta\lambda^{d}{}_{it}^{n+1}} \frac{1 + c_b\chi^{n}}{\left(e^{\beta_{\chi}\,\Delta\lambda^{d}{}_{it}^{n+1}} + c_b\chi^{n}\right)^{2}} \qquad (Eq.A.40)$$